Doctoraatsproefschrift nr. 907 aan de faculteit Bio-ingenieurswetenschappen van de K.U.Leuven

Second-harmonic generation and nonlinear optical microscopy on microporous materials and interfaces

Monique A. van der Veen

Promotor:
Prof. dr. ir. Dirk E. De Vos
Prof. dr. Thierry Verbiest

Leden van de examencommissie:
Prof. dr. ir. Robert Schoonheydt (voorzitter)
Prof. dr. ir. Dirk De Vos (secretaris)
Prof. dr. ir. Ivo Vankelecom
Prof. dr. Koen Clays
Prof. dr. ir. Pierre Jacobs
Prof. dr. Benoît Champagne

Proefschrift voorgedragen tot
het behalen van de graad van
Doctor in de
Bio-ingenieurswetenschappen

Mei 2010

ISBN 978-90-8826-147-3
D/2010/11.109/26

Acknowledgements

Often you hear people describe their PhD as climbing a mountain of which the summit is not visible. Or they describe it as a process in phases, in which, after a phase of sheer enthusiasm, comes a phase of finding it hard to be motivated. A stage in which they feel as if they are pushing a huge boulder up a hill and they see it hardly move at all and they feel as if they would like to step aside and just let the boulder roll down. I know that I too have felt like that, but I don't remember it.
I only remember that I enjoyed doing it. And many people were part of making that enjoyment happen, and for that I would like to thank them.

First of all I would like to thank my promotor, Prof. Dirk De Vos. Not only did Dirk guide me through these four years, did he affect me with his enthusiasm, and did he teach me to focus on the right questions, he also gave me a custom-made PhD project that I feel was exactly right for me. One part of this tailored PhD-project was a cooperation with the Department of Chemistry. This cooperation was embodied by my co-promotor Prof. Thierry Verbiest. I didn't know Thierry before embarking on this journey, but it turned out that it was hard to imagine a person easier to work with than Thierry. I would like to thank him for guiding me into the world of nonlinear optics, and for giving me opportunities and for believing that I could fulfill them, like building a SHG-microscope.

It was great to work in both scientific groups. I would like to thank Wim, Csaba, Kasper, Kurt, Anneleen, Stijn Van Cleuvenbergen, Edith, Rob, Luis, Ayelle, Jéremy, Mondher, Metin, Filip, Charlie, Jan, Leen, all three Pieters (Verlooy, Smeets and Levecque), Bart T., An, Lana, Sneha, and Katrien for all the nice chats and funny stories. I have been lucky to have had Julie Verhelst as a thesisstudent. When I started my PhD, Luc, Inge, Stijn Foerier and Javier were further along the journey, or had already completed their PhD, and their advice on the not-strictly scientific part of completing a PhD was invaluable.

I would like to thank Marjan De Roeck, Jasper Vannoyen, Ventsislav Valev, Prof. Bert Sels, Prof. Pierre Jacobs and Prof. Ivo Vankelecom for their contributions leading to this work. In particular I am grateful to Prof. Ivo Vankelecom and Prof. Bert Sels for the interesting discussions and to Jasper for synthezing materials. Marjan, I would like to thank for the experiments, discussions and laughs. I would like to thank FWO Vlaanderen for their financial support these four years. The members of the jury I would like to thank for their interest in my research and for accepting to read my dissertation. I thank them also for their valuable comments during my preliminary defense.

Frans and Rik, I want to thank for manufacturing all those electronic devices, and Stef and Johan, for all the help of mechanical nature. Sabina I would like to thank for the time she has spend in the lab for me, and Mia, Gina, Dirk Dom and Hugo, for all their practical help in the lab. I should also thank all the people working at the ‘secretariaat’ of the COK, they have always helped me with a smile.

Tina, Els en Sarah, jullie zijn mijn beste vriendinnen, maar dat wisten jullie natuurlijk al. Ik wou jullie bedanken voor al de goeie tijden en voor het oprecht geïnteresseerd zijn in mijn doctoraat.

Mijn ouders wou ik graag bedanken omdat ze er altijd voor mij zijn, omdat ze altijd achter mijn studiekeuzes hebben gestaan, en omdat ze me van kindsaf hebben getoond dat leren en begrijpen hoe dingen in elkaar zitten leuk zijn. Rud, bij jou weet ik niet eens waar ik moet beginnen met bedanken. Je bent erbij geweest vanaf de studiekeuze die op het einde van het middelbaar gemaakt moest worden. Ik denk dat ik je vooral wil bedanken omdat je al die tijd van mij gehouden hebt.

Table of contents

Abstract

Zeolites are extensively used in the chemical industry. A very important aspect of these industrial processes is the adsorption of molecules in the zeolite pores and the behaviour of the molecules inside the pores. In this thesis a new tool is presented to study these phenomena: second-harmonic generation. A key feature is that, within the electric-dipole approximation, generation of SHG is forbidden in centrosymmetric systems. This has important consequences. First of all, SHG from surrounding bulk phases like e.g. liquids is non-existent, giving SHG inherent specificity for asymmetric systems like interfaces. Secondly, it makes SHG extremely sensitive to the symmetry and order properties of a system. In this thesis, optimal use is made of these features to study adsorption, diffusion and the organization of molecules in zeolites or zeolite-related materials. Not only SHG as such, but also SHG microscopy, complemented by two-photon fluorescence microscopy, has been used in this work.

We have for the first time used second-harmonic generation to probe *in situ* adsorption onto a zeolite, *viz.* a *b*-oriented silicalite-1 film. This methodology allowed for the observation of this process in the liquid phase and for a deeper insight into the complexity of the adsorption process. By continuously monitoring the change in orientation of the aromatic adsorbate molecules, it was established that the DAMPI adsorbate molecules positioned themselves gradually more into the pore direction over the course of two hours (DAMPI = 4-(4'-diethylaminostyryl)-1-methylpyridinium iodide). The data suggest a physisorbed state on the outer surface prior to pore-mouth adsorption. In literature, such a preceding physisorbed state has been observed for adsorption of aromatic molecules on a zeolite in the gas phase. However, SHG has allowed for the first time an observation of this state in the liquid phase.

The suitability of SHG to probe buried interfaces has also been exploited by showing that diffusion of a solute through a thin film under a liquid phase can be probed by SHG *in situ*. In particular, diffusion through silicalite-1 precursor films deposited on a solid substrate was studied. It was in fact the arrival of the solute molecules at the solid/film interface that was monitored. This is an important finding since only few techniques are

capable to study diffusion through buried films and each of these techniques has its limitations.

Apart from these bulk measurements, a SHG-microscope was built. This type of microscopy was for the first time used to study zeolites. More specifically we explored molecular organization inside zeolites. First this was done for *p*-nitroaniline adsorbed in ZSM-5 crystals. It was possible to relate the different molecular organization of *para*-nitroaniline in the two pore types of ZSM-5 to their SHG response, making SHGM a powerful tool for revealing structural details and the intergrown structure of ZSM-5 crystals. The SHG-response is due to a surface selection process which causes the PNA molecules to adsorb predominantly with one functional group first, giving rise to SHG-active dipole chains inside the pores. The microscopy set-up made it possible to see the effect of the bidimensionality of the pore system on the dipolar organization. Indeed, only close the surface the adsorbed PNA gave rise to SHG; further on inside the pores, diffusion from one pore type to the other disrupts the dipolar organization.

The SHG microscope was also used to image the PNA-filled one-dimensional pore system of SAPO-5 zeolite crystals. The SHG and 2-photon fluorescence response of PNA in the one-dimensional channels readily reveals the pore accessibility; intergrown crystallites containing hexagonal pyramidal components and internal diffusion barriers are found next to seemingly perfect crystals in which the pores run from one crystal end to the other. The sensitivity of second-harmonic generation to molecular orientation combined with the spatial resolution of microscopy allowed for mapping of the domains of differently organized PNA. Dense phases of highly aligned PNA alternate with phases of more loosely interacting PNA. It could be shown that these dense or dilute domains extend in all crystallographic directions, with domains ranging from around 1 µm to more than 10 µm.

These SHGM observations reveal the potential of using SHGM for studying molecular organization in host materials. Although less detailed than X-ray diffraction in determining molecular ordering, SHGM possesses spatial resolution and is not limited to guest molecules with a crystallographic ordering, preferably with the same periodicity as the host, as is XRD.

Samenvatting

Zeolieten worden intensief gebruikt in de chemische industrie. Een heel belangrijk aspect van deze industriële processen is de adsorptie van moleculen in de zeolietporiën en het gedrag van deze moleculen binnen de poriën. In deze thesis wordt een nieuwe techniek gepresenteerd om deze fenomenen te bestuderen: tweede-harmonische generatie (THG). Een belangrijke eigenschap is dat, binnen de elektrische dipool approximatie, generatie van THG verboden is in centrosymmetrische systemen. Dit heeft belangrijke gevolgen. Ten eerste, is THG van omringende bulk fasen zoals vloeistoffen onbestaand, wat ervoor zorgt dat THG specifiek asymmetrische systemen zoals interfasen meet. Ten tweede, maakt het THG extreem gevoelig voor de symmetrie en ordening van een systeem. In deze thesis wordt optimaal gebruik gemaakt van deze eigenschappen om adsorptie, diffusie en de organisatie van moleculen in zeolieten of zeoliet gerelateerde materialen te bestuderen. Niet enkel THG op zich, maar ook THG microscopie, aangevuld met twee-foton fluorescentie microscopie, werd gebruikt in dit werk.

Voor de eerste maal werd THG gebruikt om adsorptie op een zeoliet, meer bepaald een *b*-georiënteerde silicaliet-1 film, *in situ* te bestuderen. Deze methodologie liet toe dit proces te volgen in de vloeistoffase en een dieper inzicht in de complexiteit van het adsorptieproces te bekomen. Door continu de verandering in oriëntatie van de aromatische adsorbaat moleculen te volgen, werd vastgesteld dat de DAMPI adsorbaat moleculen zichzelf geleidelijk aan meer in de porierichting positioneerden over een periode van twee uur (DAMPI = 4-(4’-diethylaminostyryl)-1-methylpyridinium jodide). De data suggereren een gefysisorbeerde toestand op het buitenoppervlak voorafgaand aan de adsorptie in de poriemond. In de literatuur werd een dergelijke voorgaande gefysisorbeerde toestand reeds geobserveerd voor adsorptie van aromatische moleculen in een zeoliet in de gasfase. THG liet echter toe om deze toestand voor de eerste maal in de vloeistoffase te observeren.

De geschiktheid van THG om bedekte interfasen te onderzoeken werd ook geëxploiteerd door aan te tonen dat diffusie van een opgeloste verbinding doorheen een dunne film ondergedompeld in een vloeistof, bestudeerd kan worden met THG *in*

situ. Meer bepaald is de diffusie doorheen silicaliet-1 precursor filmen afgezet op een vast substraat bestudeerd. Het was in feite de aankomst van de verbinding aan de vaste stof/film interfase die gevolgd werd. Dit is een belangrijke vinding aangezien slechts enkele technieken de diffusie doorheen bedekte filmen kunnen meten en elk van deze technieken zijn beperkingen heeft.

Afgezien van deze bulk metingen, werd een THG-microscoop (THGM) gebouwd. Dit type microscopie werd voor de eerste maal gebruikt om zeolieten te bestuderen. Meer bepaald werd de moleculaire organisatie binnenin zeolieten bestudeerd. Allereerst werd dit gedaan voor *p*-nitroaniline geadsorbeerd in ZSM-5 kristallen. Het was mogelijk om de verschillende moleculaire organisatie van *p*-nitroaniline in de twee porietypes van ZSM-5 te relateren aan de respectievelijke THG-respons. Dit maakt dat THGM een krachtige techniek is om de structurele details en de vergroeide structuur van ZSM-5 kristallen te bestuderen. De THG-respons wordt veroorzaakt door een oppervlakte selectie proces dat maakt dat de PNA-moleculen preferentieel met één functionele groep eerst adsorberen, met als gevolg THG-actieve dipoolketens in de poriën. De microscopie-opstelling maakte het mogelijk om het effect van de bidimensionaliteit van het poriesysteem op de dipolaire organisatie te bestuderen. Inderdaad, enkel dicht bij het oppervlak genereerden de geadsorbeerde PNA moleculen THG; verderop in de poriën werd de dipolaire organisatie verstoord door diffusie van het ene porietype naar het andere.

De THG microscoop werd ook gebruikt om het met PNA gevulde eendimensionale poriesysteem van SAPO-5 zeoliet kristallen te visualiseren. De THG en 2-foton fluorescentie respons van PNA in de eendimensionale kanalen onthulde rechtstreeks de toegankelijkheid van de poriën; vergroeide kristallieten bestaande uit hexagonale piramidale componenten en interne diffusiebarrières werden geobserveerd naast ogenschijnlijk perfecte kristallen waarin de poriën lopen van het ene kristaluiteinde tot het andere. De gevoeligheid van tweede-harmonische generatie voor moleculaire organisatie gecombineerd met de ruimtelijke resolutie van de microscoop, maakte het mogelijk om domeinen van verschillend georganiseerd PNA in kaart te brengen. Dense fasen waarbinnen de oriëntatie van PNA quasi samenvalt met de porierichting werden afgewisseld met fasen waarbinnen de PNA moleculen zeer beperkt met elkaar

interageren. Er werd aangetoond dat deze dichte of minder aaneengesloten domeinen zich uitstrekken in alle kristallografische richtingen, waarbij domeinen variëren van ongeveer 1 µm tot meer dan 10 µm.

Deze THGM observaties tonen het potentieel van THGM voor de studie van moleculaire organisatie in poreuze materialen aan. Hoewel THGM minder gedetailleerd is dan X-stralen diffractie (XRD) in het bepalen van moleculaire ordening, bezit THGM ruimtelijke resolutie en is THGM niet beperkt tot gastmoleculen met een kristallografische ordening, preferentieel met dezelfde periodiciteit als het poreuze waardmateriaal, zoals XRD wel is.

List of abbreviations

AFM	atomic force microscopy
ATR-IR	attenuated total reflection Fourier transform infrared spectroscopy
DAMPI	4-(4-diethylaminostyryl)-1-methylpyridinium iodide
EBSD	electron backscatter diffraction
IR	infrared
NMR	nuclear magnetic resonance
PMT	photo-multiplier tube
PNA	*para*-nitroaniline
PS	precursor solution
PTFE	polytetrafluoroethylene
SEM	scanning electron microscopy
SHG	second-harmonic generation
SHGM	second-harmonic generation microscopy
TEOS	tetraethyl orthosilicate
THG	tweede-harmonische generatie
TPAOH	tetra-n-propylammonium hydroxide

TPF	two-photon fluorescence
TPFM	two-photon fluorescence microscopy
UV-Vis	ultraviolet and visible
XRD	X-ray diffraction

Chapter 1: Introduction

Abstract

A theoretical treatment of second-harmonic generation in the framework of the experimental work described in this thesis and a brief introduction to zeolites are given, followed by an overview of the objectives of this thesis.

1.1 Introduction

Zeolites are extensively used in the chemical industry. A very important aspect of these industrial processes is the adsorption of molecules into the zeolite pores and the behaviour of the molecules inside the pores. In this thesis a new tool is presented to study these phenomena: second-harmonic generation. A key feature is that, within the electric-dipole approximation, generation of SHG is forbidden in centrosymmetric systems. This has important consequences. First of all, SHG from surrounding bulk phases like *e.g.* liquids is non-existent, giving SHG inherent specificity for asymmetric systems like interfaces. Secondly, it makes SHG extremely sensitive to the symmetry and order of a system. In this thesis, optimal use is made of these features to study adsorption, diffusion and the organization of molecules in zeolites or zeolite-related materials. Not only SHG as such, but also SHG microscopy, complemented by two-photon fluorescence microscopy, has been used in this work. In this chapter, first a short introduction to zeolites is given, followed by a relevant theoretical framework on SHG and nonlinear optical microscopy. Finally, the objectives and contents of this thesis are outlined.

1.2 A brief introduction to zeolites

Zeolites are robust, crystalline aluminosilicates with a three-dimensional network based on a three-dimensional arrangement of TO_4 tetrahedra (SiO_4 or AlO_4^-). The tetrahedral atoms (T-atoms) are connected through their oxygen atoms forming lattices with repeating identical building blocks.[1] Zeolites contain uniformly sized and spaced pores of molecular size. Close-fitting molecules adsorb preferentially in these pores, while molecules larger than the pore size are excluded. Hence, a zeolite works as a molecular sieve. Part of the Si^{4+} in the SiO_2 framework can be replaced with Al^{3+}, thus creating a charge deficiency which has to be compensated by cations residing in the pores. Some of these cations are susceptible to cation exchange and are able to reversibly interact with polar molecules. These properties make zeolites attractive materials for selective adsorption and separation of molecules, and for ion exchange.[2] Indeed, zeolites are widely used as adsorbents in chemical industry, e.g. for the separation of *m*- and *p*-

xylene with zeolite X and Y,[3] and as detergents, *e.g.* to remove the "hard" calcium and magnesium cations in laundry water. When the charge compensating cations are protons, the zeolite can act as a heterogeneous catalyst with Brønsted acidity. Moreover, cations other than protons may have Lewis acid properties and the oxobridges at the Al^{3+} sites have Lewis base properties. Introduction of metallic particles in the pore system of zeolites leads to redox catalysts. A very important feature of a zeolite catalyst is its shape-selectivity, due to steric constraints in the pores, for the adsorption and conversion of the reagent molecules.[2] This has led naturally to the industrial use of zeolites as catalysts, most notably in hydrocarbon oil refining and gas conversion.[4]

In chapter 2 and 4 zeolites silicalite-1 and ZSM-5 are studied. In chapter 3 on the other hand, we used silicalite-1 precursor films. Silicalite-1 and ZSM-5 in fact have the same topology; they both have the same framework type[i] MFI according to IUPAC nomenclature. The difference is that silicalite-1 is an all-silica material, while in ZSM-5 a small amount of the Si^{4+} atoms is substituted by Al^{3+}, giving the latter the potential of catalytic activity. In fact, ZSM-5 is a very important shape-selective catalyst, *e.g.* in xylene isomerisation and toluene disproportionation, in the conversion of methanol to hydrocarbons and in numerous other processes.[4,5,6]

This MFI topology contains two types of channels. One type is the straight 10-ring pores, in which 10 oxygen and 10 tetrahedral atoms border the channel cross-section. These straight 10-ring pores are parallel to the *b*-axis and will be called the *b*-pores. Their pore-opening is 5.6 x 5.3 Å (Scheme 1-1 a and b). The other type are sinusoidal 10-ring channels along the *a*-axis, called *a*-pores. Their pore-opening is 5.5 x 5.1 Å (Scheme 1-1 c). Both channel types intersect which leads to a three-dimensional pore system (Chapter 4: Scheme 4-1d).

[i] A framework type or structure type describes the connectivity (topology) of the framework tetrahedral atoms in the highest possible symmetry.

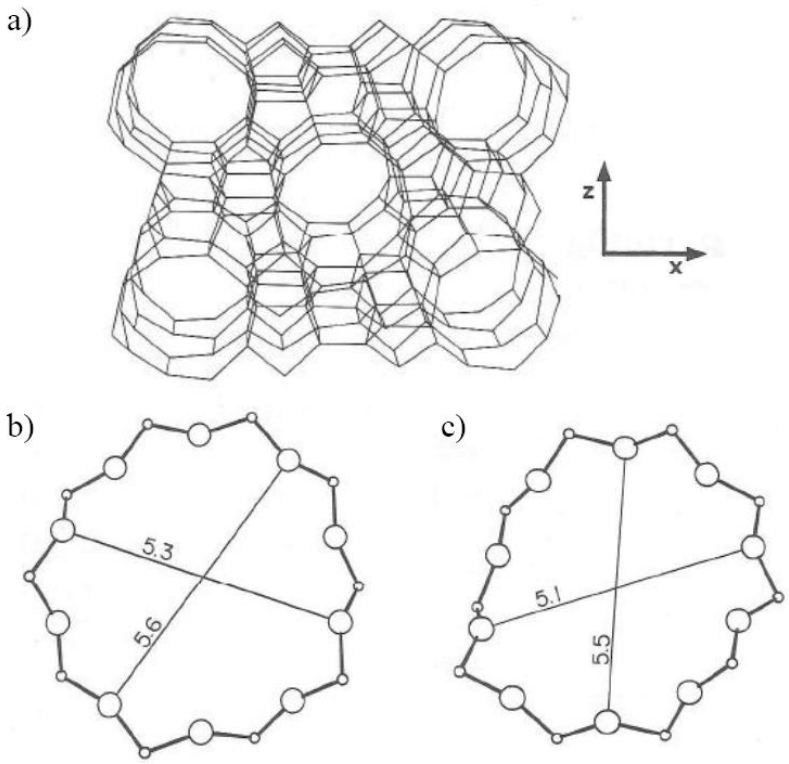

Scheme 1-1: Schematic representation of a) the MFI framework along [010], b) and c) the cross-section of resp. the *b*-pore and the *a*-pore, thus viewed resp. along [010] and [100]. The larger circles in b) and c) represent the oxygen atoms, while the smaller circles represent the hetero-atoms. In a) the T-O-T bridges are represented by straight lines and the vertices are the positions of the T-atoms. Figures adopted from the Atlas of Zeolite Structure Types.[7]

In chapter 5 SAPO-5 crystals are studied. This type of zeolites belongs to a more recent family of zeolite materials that appeared in the late 1970', the $AlPO_4$-materials. In these aluminophosphate materials, the Al^{3+} and P^{5+} atoms strictly alternate between the O^{2-} ions (Al-O-P). When a portion of the P^{5+} is substituted by Si^{4+}, the material is called a SAPO, *e.g.* SAPO-5. The thus introduced charge deficiency is balanced by cations residing in the pores. The structure type of SAPO-5 is called AFI. The structure is composed of straight one-dimensional 12-ring channels with a free diameter of 7.3 Å (Scheme 1-2).

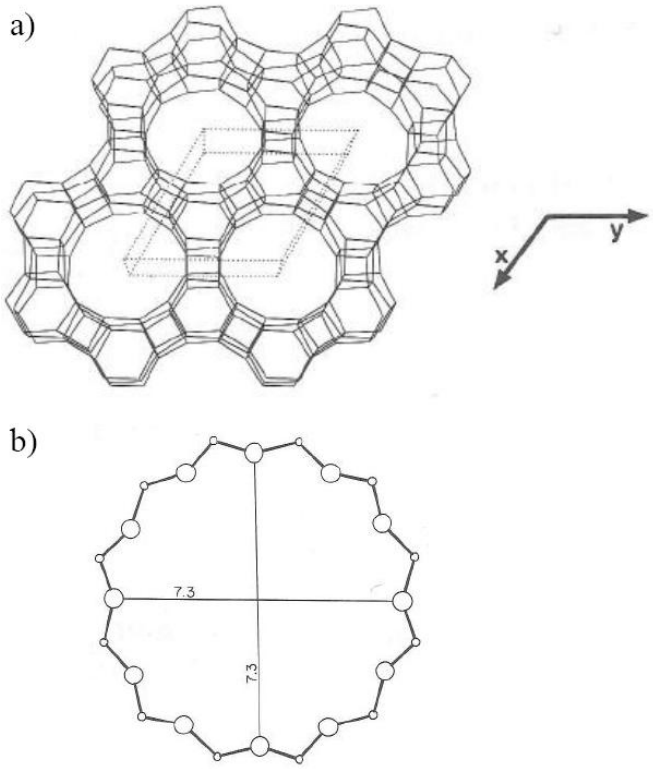

Scheme 1-2: Schematic representation of a) the AFI framework along [001], b) the cross-section of the 12-ring pores also viewed along [001]. The larger circles in b) represent the oxygen atoms, while the smaller circles represent the hetero-atoms. In a) the T-O-T bridges are represented by straight lines and the vertices are the positions of the T-atoms. Figures adopted from the Atlas of Zeolite Structure Types.[7]

1.3 Nonlinear optics

Any material can be considered as an assembly of charged particles. When light is incident on a material, these particles will start to oscillate due to the interaction with the oscillating electric field of light. In a dielectric material, and for moderate light intensity, this leads to an induced polarization $\boldsymbol{P}$ in the medium, oscillating at the same frequency ω as the incident electric field $\boldsymbol{E}$. The induced polarization $\boldsymbol{P}$ is then given by

$$\boldsymbol{P}(\omega)=\chi^{(1)}(\omega)\cdot\boldsymbol{E}(\omega) \qquad \text{Eq. 1-1}$$

with $\chi^{(1)}$ the first-order susceptibility. The induced polarization arises from the sum of the induced dipole moments $\boldsymbol{\mu}(\omega)$ of the individual atoms or molecules. Equation 1-1 can thus be written as

$$\boldsymbol{P}(\omega)=\sum_i \boldsymbol{\mu}_i(\omega) = Nf_\omega\alpha(\omega)\cdot\boldsymbol{E}(\omega)=\chi^{(1)}(\omega)\cdot\boldsymbol{E}(\omega) \qquad \text{Eq. 1-2}$$

In this equation N is the number density of molecules or atoms, $\alpha(\omega)$ is the molecular linear polarizability, and f_ω is a local field factor.[8] The latter accounts for the effects of the induced dipole moments in the medium through electronic polarization. Indeed, the local field $\boldsymbol{E}_{loc}$ at a local spatial point is the sum of the applied field $\boldsymbol{E}$ and the field of the neighbouring dipoles $\boldsymbol{E}_{dip}$.[9]

$$\boldsymbol{E}_{loc} = \boldsymbol{E} + \boldsymbol{E}_{dip} \qquad \text{Eq. 1-3}$$

If very intense light is applied (*e.g.* laser light), the relation between the polarization of the medium and the electric field is no longer linear. Equation 1-1 is then no longer valid and can be expanded into a Taylor series in terms of the applied electric field. The induced polarization can then be written as

$$\boldsymbol{P} = \boldsymbol{P}^{(1)} + \boldsymbol{P}^{(2)} + \boldsymbol{P}^{(3)} + ... = \chi^{(1)} \cdot \boldsymbol{E} + \chi^{(2)} : \boldsymbol{EE} + \chi^{(3)} \vdots \boldsymbol{EEE} + ... \qquad \text{Eq. 1-4}$$

where the terms $\boldsymbol{P}^{(2)}$ and $\boldsymbol{P}^{(3)}$ describe the nonlinear response of the medium. $\chi^{(2)}$ is the second-order susceptibility and $\chi^{(3)}$ the third-order susceptibility, characterizing the second-order and third-order nonlinear optical response of the medium.

In a similar manner, the induced dipole moment can be written as

$$\boldsymbol{\mu} = \boldsymbol{\mu}^{(1)} + \boldsymbol{\mu}^{(2)} + \boldsymbol{\mu}^{(3)} + ... = \alpha \cdot \boldsymbol{E} + \beta : \boldsymbol{EE} + \gamma \vdots \boldsymbol{EEE} + ... \qquad \text{Eq. 1-5}$$

with β and γ the first-order and second-order hyperpolarizability.[8]

1.4 Second-harmonic generation

In this work, we will mainly focus on the term $\boldsymbol{P}^{(2)}$. If we express the electric field of light as

$$\boldsymbol{E}(\boldsymbol{r}, t) = \boldsymbol{E}_0 (e^{i\boldsymbol{k}.\boldsymbol{r} - i\omega t} + cc) \qquad \text{Eq. 1-6}$$

with a time-dependent phase term, ωt (with ω the frequency), and a space-dependent phase term, $\boldsymbol{k}.\boldsymbol{r}$ (with $\boldsymbol{k}$ the wave vector), we can write the nonlinear polarization as:

$$\begin{aligned}\boldsymbol{P}^{(2)} &= \chi^{(2)} : \boldsymbol{E}\boldsymbol{E} = \chi^{(2)} : \boldsymbol{E}_0(e^{i\boldsymbol{k}.\boldsymbol{r}-i\omega t} + cc)\boldsymbol{E}_0(e^{i\boldsymbol{k}.\boldsymbol{r}-i\omega t} + cc) \\ &= 2\chi^{(2)} : \boldsymbol{E}_0\boldsymbol{E}_0 + \chi^{(2)} : \boldsymbol{E}_0\boldsymbol{E}_0(e^{2i\boldsymbol{k}.\boldsymbol{r}-i2\omega t} + cc)\end{aligned} \qquad \text{Eq. 1-7}$$

or,

$$\boldsymbol{P}^{(2)} = \boldsymbol{P}^{(0)} + \boldsymbol{P}^{(2\omega)} \qquad \text{Eq. 1-8}$$

with $\boldsymbol{P}^{(0)}$ a frequency-independent process called optical rectification, and $\boldsymbol{P}^{(2\omega)}$ a double-frequency process called second-harmonic generation. The polarization $\boldsymbol{P}^{(2\omega)}$ oscillates at the doubled frequency 2ω, and hence acts as a source of radiation at this doubled frequency. It is this radiation that is detected during SHG-measurements. As from here, when $\boldsymbol{P}^{(2)}$ is written, in fact, $\boldsymbol{P}^{(2\omega)}$ is meant.

In

$$\boldsymbol{P}^{(2)} = \chi^{(2)} : \boldsymbol{E}\boldsymbol{E} \qquad \text{Eq. 1-9}$$

$\boldsymbol{E}$ is the electric field vector, and $\chi^{(2)}$ is a third-rank tensor with 27 components $\chi^{(2)}_{ijk}$. Hence, in terms of its components, $\boldsymbol{P}^{(2)}$ can be rewritten as

$$P_i^{(2)} = \sum_{j,k} \chi_{ijk}^{(2)} E_j E_k \qquad \text{Eq. 1-10}$$

Explicitly this reads as

$$\begin{bmatrix} P_x^{(2)} \\ P_y^{(2)} \\ P_z^{(2)} \end{bmatrix} = \begin{bmatrix} \chi_{xxx}^{(2)} & \chi_{xyy}^{(2)} & \chi_{xzz}^{(2)} & \chi_{xyz}^{(2)} & \chi_{xzy}^{(2)} & \chi_{xzx}^{(2)} & \chi_{xxz}^{(2)} & \chi_{xxy}^{(2)} & \chi_{xyx}^{(2)} \\ \chi_{yxx}^{(2)} & \chi_{yyy}^{(2)} & \chi_{yzz}^{(2)} & \chi_{yyz}^{(2)} & \chi_{yzy}^{(2)} & \chi_{yzx}^{(2)} & \chi_{yxz}^{(2)} & \chi_{yxy}^{(2)} & \chi_{yyx}^{(2)} \\ \chi_{zxx}^{(2)} & \chi_{xyy}^{(2)} & \chi_{zzz}^{(2)} & \chi_{zyz}^{(2)} & \chi_{zzy}^{(2)} & \chi_{zzx}^{(2)} & \chi_{zxz}^{(2)} & \chi_{zxy}^{(2)} & \chi_{zyx}^{(2)} \end{bmatrix} \begin{bmatrix} E_x^2 \\ E_y^2 \\ E_z^2 \\ E_y E_z \\ E_z E_y \\ E_z E_x \\ E_x E_z \\ E_x E_y \\ E_y E_x \end{bmatrix} \qquad \text{Eq. 1-11}$$

Hence, complete characterization of the nonlinear behaviour of a material implies the determination of all 27 components of the nonlinear susceptibility. Fortunately, the number of independent tensor components can be drastically reduced by taking into account the symmetry of the medium and the type of nonlinear optical process. First of all, for second-harmonic generation, the two incident fields are indistinguishable and therefore the following relation is valid

$$\chi_{ijk}^{(2)} = \chi_{ikj}^{(2)} \qquad \text{Eq. 1-12}$$

This reduces the number of independent tensor components to 18.

The symmetry of the material under investigation will further reduce the number of independent nonzero components. For example, imagine a mirror plane in the *xz* plane. Under reflection in this plane the spatial coordinates transform as

$$x \rightarrow x \qquad y \rightarrow -y \qquad z \rightarrow z$$

Consequently, the polarization and field components transform as

$$E_x \rightarrow E_x \qquad E_y \rightarrow -E_y \qquad E_z \rightarrow E_z$$

$$P_x \rightarrow P_x \qquad P_y \rightarrow -P_y \qquad P_z \rightarrow P_z$$

However, the sign and magnitude of $\chi^{(2)}$, which is a materials property, must remain unchanged under any symmetry operation. The influence of this symmetry operation on the number of tensor components is easily examined by simply performing the symmetry operation on Equation 1-10. For example the relation $P_y^{(2)} = \chi_{yyy}^{(2)} E_y E_y$ transforms into $-P_y^{(2)} = \chi_{yyy}^{(2)}(-E_y)(-E_y)$, leading to $P_y^{(2)} = -P_y^{(2)}$, which can only be valid if $\chi_{yyy}^{(2)} = 0$. Performing this procedure for each combination of indices, leads to the conclusion that a material with one mirror plane has 10 independent, nonzero components instead of 18.

In fact, the higher the symmetry of the system under investigation, the fewer independent nonzero components remain. At the extreme end we find centrosymmetry.

In a centrosymmetric material every component of the electric field vector and the polarization vector changes sign under the operation of an inversion centre: $\boldsymbol{E} \rightarrow -\boldsymbol{E}$ and $\boldsymbol{P} \rightarrow -\boldsymbol{P}$. As a consequence, $\boldsymbol{P}^{(2)} = \chi^{(2)} : \boldsymbol{EE}$ changes into $-\boldsymbol{P}^{(2)} = \chi^{(2)} : (-\boldsymbol{E})(-\boldsymbol{E})$. This can only be true if all the components of $\chi^{(2)}$ are equal to zero. Hence, centrosymmetric materials do not generate a second-harmonic response.[ii] In fact, this is one of the reasons why SHG is used to study interfaces and surfaces: at the interface, centrosymmetry is necessarily broken and SHG can be used as a surface selective probe. In general, SHG has been applied to the study of anisotropic crystals, chiral materials and surfaces and interfaces.[8]

1.5 Second-harmonic generation of interfaces

As mentioned, centrosymmetry must be broken to generate an electric-dipole allowed second-harmonic signal. At the interface between two centrosymmetric materials this symmetry is necessarily broken, and an interface will always have a nonzero nonlinear susceptibility $\chi^{(2)}$, often referred to as surface susceptibility $\chi_S^{(2)}$. Whenever the susceptibility $\chi^{(2)}$ is mentioned in this section (1.5), it is in fact the surface nonlinear susceptibility $\chi_S^{(2)}$ that is meant.

1.5.1 SHG set-up

The experimental SHG set-up that was used in this thesis is operating in reflection geometry. A detailed description of this set-up is given both in chapter 2 and 3. Here, we shall limit ourselves to a discussion of the geometry of the incoming light, the SHG-generated light and the sample (Scheme 1-3). The plane of polarization of the incident light is determined by the position of a half-wave plate ($\lambda/2$ in Scheme 1-3). The fundamental beam can be expressed in terms of its *p*- and *s*-polarized components:

[ii] This is correct within the electric-dipole approximation, which means that only the electric-dipole contributions to the nonlinear response are taken into account as is done in this text. More generally, there can be other contributions to SHG, *viz.* magnetic-dipole and electric-quadrupole interactions and the material may develop a nonlinear magnetization and quadrupolization. However, in the research presented in this work the electric-dipole approximation is reasonable.

$$\boldsymbol{E}(\omega) = \boldsymbol{p}E_p(\omega) + \boldsymbol{s}E_s(\omega) \qquad \text{Eq. 1-13}$$

with E_p and E_s the p- and s-polarized components of the field. The unit vectors are related to the laboratory coordinates (x, y, z) by

$$\boldsymbol{s} = -\boldsymbol{y} \qquad \text{Eq. 1-14}$$

and

$$\boldsymbol{p} = \boldsymbol{x}\cos\gamma + \boldsymbol{z}\sin\gamma \qquad \text{Eq. 1-15}$$

with γ the angle of incidence. In fact the s-polarized component is the component of the electric field vector that is perpendicular to the plane of incidence. The p-polarized component is the component of the electric field vector that is parallel to the incidence plane (Scheme 1-3 and Scheme 1-4).

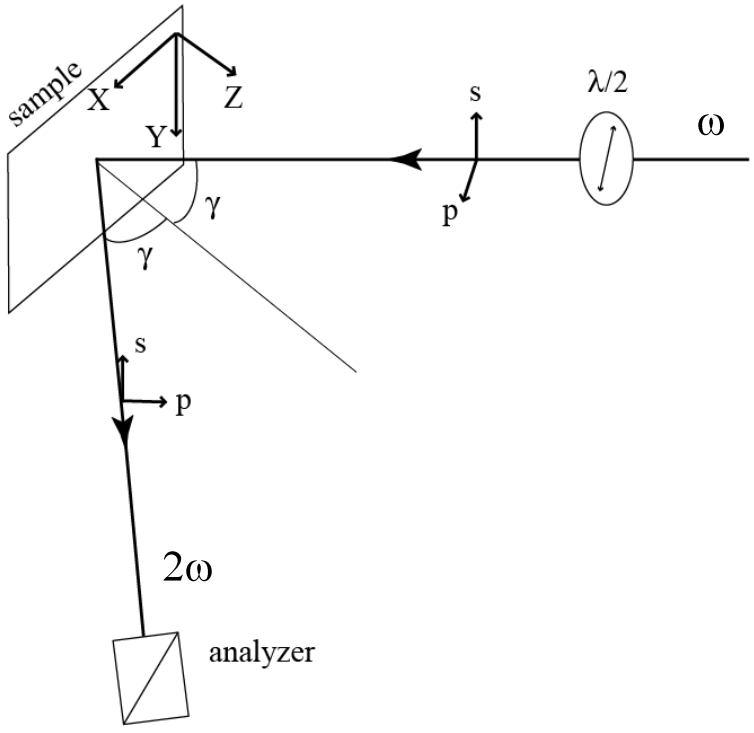

Scheme 1-3: Schematic representation of the geometry of the incident light, the second-harmonic light and the sample during the SHG interface measurements.

While SHG is generated both in transmission and reflection, we will only detect the reflected component in our set-up. Due to the coherent nature of SHG, the second-

harmonic light is generated under the same angle as the angle of incidence γ. In order to analyze both *p*-and *s*-polarized components of the second-harmonic light, we use an analyzer before the detector.

1.5.2 General principles

To describe the second-harmonic generated by a surface we treat the interfacial system as a three-layer system (Scheme 1-4) composed of an interfacial layer with a centrosymmetric medium (1 and 2) at either side. The second-harmonic intensity generated in the reflected direction by the nonlinear polarization of the interfacial layer is described by following expression.[10,11]

$$I(2\omega) \propto \left|\chi_{eff}^{(2)}\right|^2 I(\omega)^2 \qquad \text{Eq. 1-16}$$

with $I(\omega)$ the intensity of the input field, and $\chi_{eff}^{(2)}$ an effective nonlinear susceptibility that takes into account all possible SHG contributions.

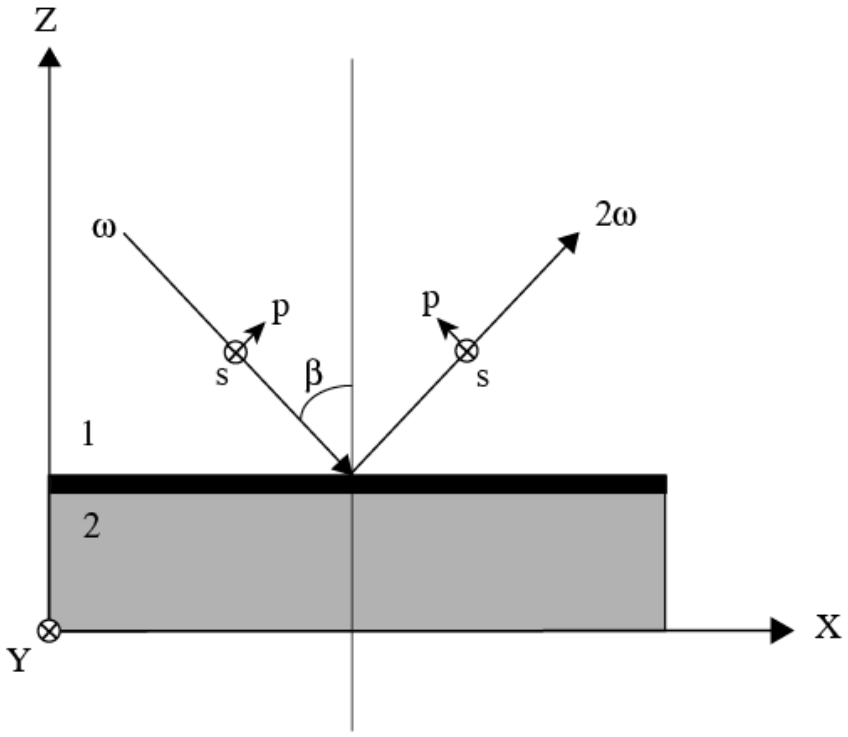

Scheme 1-4: Representation of the laboratory coordinates (*x*,*y*,*z*), the unit vectors of the *p*-polarized and *s*-polarized electric field of light.

For the cases presented in chapter 2 and 3, it is reasonable to describe the probed surface as an achiral, rotationally in plane-isotropic surface, thus with $C_{\infty v}$ symmetry. This means there are only three independent nonzero components of $\chi^{(2)}$. With the lab coordinates chosen so that z is perpendicular to the interface, and x in the incident plane these are $\chi^{(2)}_{zzz}, \chi^{(2)}_{zxx} = \chi^{(2)}_{zyy}$ and $\chi^{(2)}_{xxz} = \chi^{(2)}_{yyz} = \chi^{(2)}_{xzx} = \chi^{(2)}_{yzy}$.

Hence, the three independent components of $\chi^{(2)}$ in the *xyz* coordinate system can be measured through measuring three independent $\chi^{(2)}_{eff}$ terms. However, this is most conveniently done by expressing the $\chi^{(2)}_{eff}$ components in the spk coordinate system, followed by three independent measurements for different input and output polarizations: *s*-in/*p*-out ($\chi^{(2)}_{sp}$), *45*°-in/*p*-out ($\chi^{(2)}_{45°s}$) and *p*-in/*p*-out ($\chi^{(2)}_{pp}$). These $\chi^{(2)}_{eff}$ terms are related to the interfacial macroscopic susceptibilities tensor components $\chi^{(2)}_{ijk}$ by the following equations

$$\chi^{(2)}_{eff,sp} = L_{zz}(2\omega)L^2_{yy}(\omega)\sin(\gamma)\chi^{(2)}_{zyy} \qquad \text{Eq. 1-17}$$

$$\chi^{(2)}_{eff,45°s} = L_{yy}(2\omega)L_{zz}(\omega)L_{yy}(\omega)\sin(\gamma)\chi^{(2)}_{yzy} \qquad \text{Eq. 1-18}$$

$$\begin{aligned}\chi^{(2)}_{eff,pp} = {} & L_{zz}(2\omega)L^2_{xx}(\omega)\sin(\gamma)\cos^2(\gamma)\chi^{(2)}_{zxx} \\ & -2L_{xx}(2\omega)L_{zz}(\omega)L_{xx}(\omega)\sin(\gamma)\cos^2(\gamma)\chi^{(2)}_{xzx} \\ & +L_{zz}(2\omega)L^2_{zz}(\omega)\sin^3(\gamma)\chi^{(2)}_{zzz}\end{aligned} \qquad \text{Eq. 1-19}$$

in which the Fresnel factor terms $L_{ii}(\Omega)$ were defined by Zhuang et al.[11] and Wei et al.[12]

$$L_{xx}(\Omega) = \frac{2n_1(\Omega)\cos\rho}{n_1(\Omega)\cos\rho + n_2(\Omega)\cos\gamma} \qquad \text{Eq. 1-20}$$

$$L_{yy}(\Omega) = \frac{2n_1(\Omega)\cos\gamma}{n_1(\Omega)\cos\gamma + n_2(\Omega)\cos\rho} \qquad \text{Eq. 1-21}$$

$$L_{zz}(\Omega) = \frac{2n_2(\Omega)\cos\gamma}{n_1(\Omega)\cos\rho + n_2(\Omega)\cos\gamma}\left(\frac{n_1(\Omega)}{n'(\Omega)}\right)^2 \qquad \text{Eq. 1-22}$$

In these equations, $n'(\Omega)$ is the refractive index of the interfacial layer at frequency Ω, γ is the incidence angle of the light under consideration and ρ is the refracted angle. The Fresnel factors correct for the reflection, transmission and refraction of light when it passes from one medium to another medium with a different refractive index.

In general however, one is not restricted to the measurement of only three polarization combinations. One can for example measure a complete polarization dependence of both *s*- and *p*-polarized second-harmonic components by continuously rotating a half-wave plate in the incident beam. The dependence of the susceptibility components for the *s*- and *p*-polarized second-harmonic on the rotation angle of the plane of polarization of the input light is given by

$$\chi^{(2)}_{eff,p} = \sin^2(\alpha)\chi^{(2)}_{eff,sp} + \cos^2(\alpha)\chi^{(2)}_{eff,pp} \qquad \text{Eq. 1-23}$$

$$\chi^{(2)}_{eff,s} = \sin(2\alpha)\chi^{(2)}_{eff,45°s} \qquad \text{Eq. 1-24}$$

In these equations, α is the angle of the plane of polarization of the incident light. This angle α is equal to 0° for *p*-polarized fundamental light and 90° for *s*-polarized light.

1.5.3 SHG of molecular interfaces

In case of a layer of adsorbate molecules on an interface, the surface susceptibility $\chi^{(2)}_S$ can be expressed as

$$\chi^{(2)}_S = \chi^{(2)}_{substrate} + \chi^{(2)}_{\text{int}}(\theta) + \chi^{(2)}_{ad}(\theta) \qquad \text{Eq. 1-25}$$

with $\chi^{(2)}_{substrate}$, $\chi^{(2)}_{int}$, and $\chi^{(2)}_{ad}$ the contributions respectively from the substrate surface itself, from the interaction between the substrate and the adsorbate molecules, and from the adsorbate molecules themselves. The latter two contributions are dependent upon the adsorbate coverage θ.[13] In chapter 2 and 3, it is the adsorbate nonlinear susceptibility term $\chi^{(2)}_{ad}$ which dominates the surface susceptibility; so this term will be discussed more thoroughly.

The second-harmonic generated through $\chi_{ad}^{(2)}$ is determined by the adsorbed molecules and can be related to the molecular hyperpolarizability of the adsorbate as[13]

$$\chi_{ijk}^{(2)} = Nf \sum_{i'j'k'=x'y'z'} \left\langle R_{ii'} R_{jj'} R_{kk'} \right\rangle \beta_{i'j'k'} \qquad \text{Eq. 1-26}$$

where N is the molecule number density, the operator $\langle\rangle$ denotes the orientational ensemble average over the Euler rotation matrix transformation element $R\gamma\gamma'$ from the molecular coordinate $\gamma'(x',y',z')$ to the laboratory coordinate $\gamma(x,y,z)$, through the three Euler angles (θ,ψ,φ). The subscript (i, j, k) of the susceptibility $\chi_{ijk}^{(2)}$ corresponds to the laboratory coordinates (x,y,z) (Scheme 1-4 and Scheme 1-5) and the subscript (i',j',k') of the hyperpolarizability β corresponds to the molecular coordinates (x',y',z') (Scheme 1-5). f is a correction for the local field (Section1.3). Furthermore, this local field correction is often included into the equation for the Fresnel factor L_{zz} (Equation 1-23) through the effective refractive index n'.[11,12,14,15] Hence, we can write

$$\chi_{ijk}^{(2)} = N \sum_{i'j'k'=x'y'z'} \left\langle R_{ii'} R_{jj'} R_{kk'} \right\rangle \beta_{i'j'k'} \qquad \text{Eq. 1-27}$$

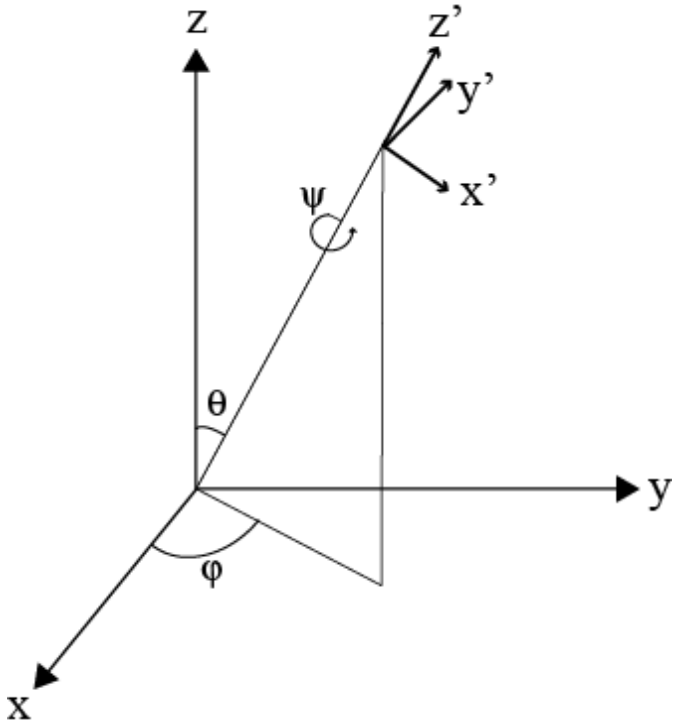

Scheme 1-5: Euler angles (θ,ψ,φ) relating the molecular (x',y',z') and laboratory (x,y,z) coordinate systems.

For example, consider the case of a molecule with a well defined long molecular axis and with its hyperpolarizability tensor β dominated by a single tensor element $\beta_{z'z'z'}$ with z' along the long molecular axis. In general, this is the case for dipolar *para*-substituted stilbene and stilbazolium molecules, such as 4-hydroxy-4'-nitrostilbene and 4-(4'-diethylaminostyryl)-1-methylpyridinium iodide (DAMPI).[16,17,18] Even some smaller dipole molecules like *p*-nitroaniline can be sufficiently described by a single tensor element $\beta_{z'z'z'}$ with z' along the long molecular axis.[19]

If the molecular response can be described by a single tensor element $\beta_{z'z'z'}$, all the elements of the tensor $\chi^{(2)}$ originate from this tensor element. Moreover, for a surface of $C_{\infty v}$ symmetry, which in this case means that the adsorbate molecules have a random azimuthal distribution, the three non-zero independent components of $\chi^{(2)}$ (Section 1.5.2) reduce further to two non-zero independent components of $\chi^{(2)}$ since following relation is now valid:

$$\chi^{(2)}_{zxx} = \chi^{(2)}_{zyy} = \chi^{(2)}_{xxz} = \chi^{(2)}_{yyz} = \chi^{(2)}_{xzx} = \chi^{(2)}_{yzy} = \frac{1}{2} N \beta_{z'z'z'} \left\langle \sin^2\theta \cos\theta \right\rangle \qquad \text{Eq. 1-28}$$

with θ the angle between z' and the surface normal z. and the angular brackets refer to an orientational average. The other component is given by

$$\chi^{(2)}_{zzz} = N \beta_{z'z'z'} \left\langle \cos^3\theta \right\rangle \qquad \text{Eq. 1-29}$$

It is obvious from Equation 1-28 and 1-29 that the ratio of these two independent components of $\chi^{(2)}$, together with the assumption of a δ-function for the orientational distribution, allows us to deduce the tilt angle θ of the adsorbate molecules.[20] For this aim we can define A as

$$A = \frac{2\chi^{(2)}_{xzx}}{\chi^{(2)}_{zzz} + 2\chi^{(2)}_{zxx}} = \frac{\left\langle \sin^2\theta \cos\theta \right\rangle}{\left\langle \cos\theta \right\rangle} \qquad \text{Eq. 1-30}$$

With a δ-function of the orientational distribution we can directly obtain the tilt angle θ through

$$\theta = \sin^{-1}\sqrt{A} \qquad \text{Eq. 1-31}$$

The two independent components of $\chi^{(2)}$ can be measured independently as is shown in Section 1.5.2.

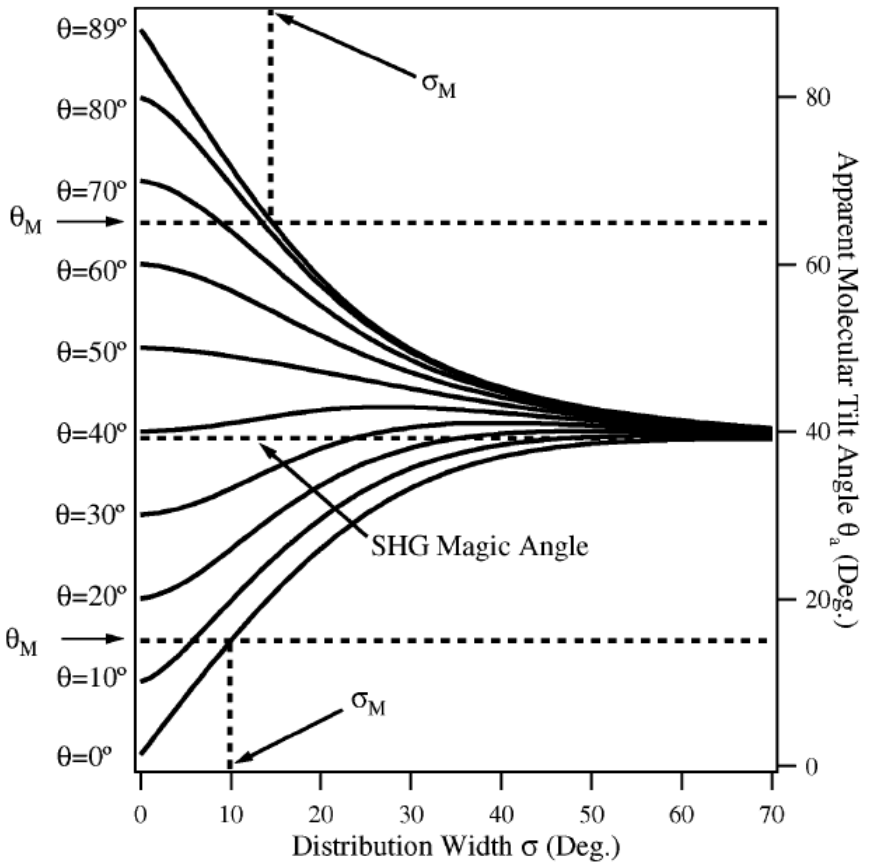

Figure 1-1: The apparent molecular orientational angle (calculated by assuming a δ-function distribution) as a function of the root-mean-square width σ of a Gaussian distribution function. Each curve corresponds to a centre orientational angle θ. The straight line at 39.2° is the magic angle. Two horizontal dashed lines are drawn to show how to determine the θ_M and σ_M with known A value as discussed in the text. Adapted with permission from G. J. Simpson and K. L. Rowlen, J. Am. Chem. Soc., 1999, 121, 2635–2636. Copyright 1999 American Chemical Society.[21]

However, the assumption of a δ-function for the orientational distribution of the adsorbate molecules is not always reasonable. Simpson and Rowlen investigated the dependency of orientation measurements on the width of the orientation distribution.[21] They calculated the relation between the true centre orientation angle θ, the apparent orientation angle θ_a as calculated via A by assuming a δ-function distribution, and the width of distribution σ for a Gaussian distribution. Their results are shown in Figure 1-1. It is clear that when the width of distribution σ increases, the apparent tilt angle θ_a

calculated through A becomes 39.2° regardless of the true centre orientation angle. This angle is often referred to as the magic angle. This means that when tilt angles close to the magic angle are obtained through A, this may be due to the disorder of the adsorbate molecules.

Via the orientational parameter A, we cannot simultaneously determine the two independent orientational variables, namely, the orientational angle θ, and the distribution width σ. Simpson et al.[22] showed that via a linear spectroscopic method another order parameter can be measured, which together with the A value measured by SHG, can provide both the orientational angle θ and the distribution width σ. However, as Zhang et al.[15] pointed out, the key difficulty is that linear spectroscopic methods do not have the inherent surface specificity that make second-harmonic generation so interesting. Therefore, it is not always possible to measure an order parameter via a linear spectroscopic method. Nevertheless, we can still deduce useful information from a singular SHG-measurement. For a measured A value we can determine a maximum or minimum possible orientation angle θ_M and a maximum possible distribution σ_M (Figure 1-1). This information is especially useful when A is significantly away from the magic angle value of A.[15]

1.6 Nonlinear optical microscopy

1.6.1 Set-up

A schematic representation of the second-harmonic generation microscopy and multi-photon microscopy set-up is shown in Scheme 1-6. The light source is a Ti:sapphire laser (Spectra-Physics, Tsunami) that generates ~100 fs pulses with a repetition frequency of 80 MHz. The wavelength of the laser light can be tuned between 730 and 870 nm, and the output light is linearly polarized. In the experimental work presented in this thesis, a wavelength of 800 nm has been used. As can be seen in Scheme 1-6, first a half-wave plate (λ/2 in Scheme 1-6) is placed in the beam path. Together with the first polarizer of the optical isolator (Optics for Research, IO-5BB-800-HP), rotation of this half-wave plate can be used to adjust the intensity of the laser light. The optical isolator transmits light only in one direction and is used to avoid back-reflections into the laser

cavity of optics further along the beam path. A second half-wave plate is used to make the laser light *p*-polarized. Next, a mirror (M2) sends the laser light through a pair of prisms (Newport, SF10) at the Brewster angle. The *p*-polarization of the light ensures a minimal reflection loss. Mirror M3 is used to send the light a second time through the prisms. The function of the prisms is to compensate for the group velocity dispersion introduced by the other optics in the beam path. After this second passage the light skims over the edge of mirror M2. The function of the third half-wave plate is to choose the plane of polarization of the laser light that is incident on the sample. A long pass red filter (Schott, RG665, 1mm) blocks transmittance of second-harmonic light generated by

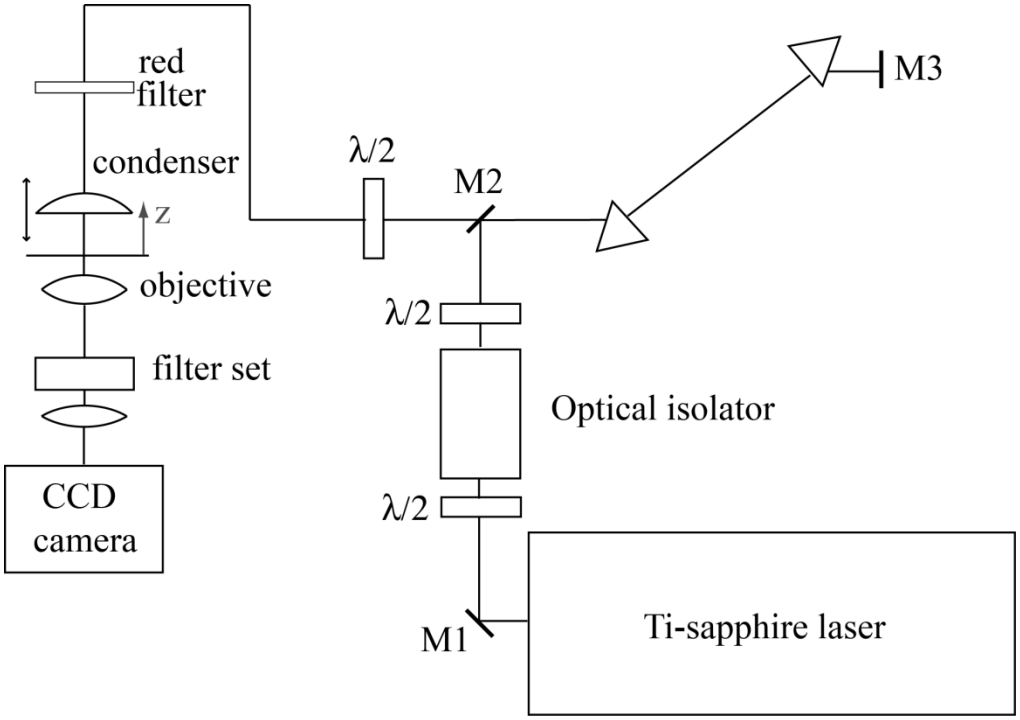

Scheme 1-6: Schematic representation of the joint SHGM and TPFM set-up. *λ*/2 stands for half-wave plate and M for mirror.

the optics earlier in the beam path and inside the laser. A lens (Thorlabs, best form lens, f= 5cm, B-coated) is used as a condenser. Via a translation stage the distance between the condenser and the sample can be adjusted to determine the size of the illuminated spot on the sample and the light intensity on the sample. The following parts, together with the sample stage are part of an inverted microscope (Olympus, IX71): the objective, a filter carousel and a tube to which the camera is connected. Via rotation of the filter carousel, different filter sets can be chosen. The filter set for the second-

harmonic light consists of a band pass filter (Schott, BG39, 2mm) and an interference filter (Melles-Griot, F10-400, centre wavelength 400 nm, FWHM 10 nm). The filter set for the two-photon fluorescence light consists of a band pass filter (Schott, BG39, 3mm) and a long pass filter (Schott, GG435, 2 mm). The transmitted light is then guided to an EM-CCD camera (Hamamatsu, C9100-13).

1.6.2 Second-harmonic generation microscopy

In the described set-up the direction of propagation of the incident light and the second-harmonic light is perpendicular to the sample plane. If we choose the laboratory coordinate system such that the *z*-axis is perpendicular to the sample plane (Scheme 1-6 and Scheme 1-7), then the *z*-axis coincides with the direction of light propagation. This means that the electric field vector of both the incident light and the second-harmonic light has no electric field component E_z in the *z*-direction. This means that only the elements $\chi^{(2)}_{ijk}$ without *z*-indices are probed, *i.e.* $\chi^{(2)}_{xxx}, \chi^{(2)}_{xyy}, \chi^{(2)}_{xxy} = \chi^{(2)}_{xyx}, \chi^{(2)}_{yyy}, \chi^{(2)}_{yxx}$ and $\chi^{(2)}_{yxy} = \chi^{(2)}_{yyx}$. All these elements are non-zero only if there is no symmetry is the sample plane.

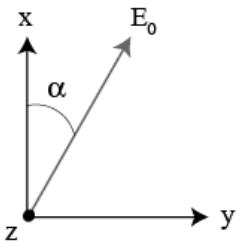

Scheme 1-7: Schematic representation of the electric field vector E of the incident light versus the laboratory coordinates used to describe the SHGM-response.

If we use Equation 1-10 and take into account all these elements of $\chi^{(2)}$, then the relation between the electric field E of the fundamental light and the polarization P_x generated in the *x*-direction becomes

$$\begin{aligned} P_x^{(2)} &= \chi^{(2)}_{xxx} E_x E_x + \chi^{(2)}_{xyy} E_y E_y + \chi^{(2)}_{xyx} E_y E_x + \chi^{(2)}_{xxy} E_x E_y \\ &= \chi^{(2)}_{xxx} E_0^2 \sin^2\alpha + \chi^{(2)}_{xyy} E_0^2 \cos^2\alpha + 2\chi^{(2)}_{xyx} E_0^2 \cos\alpha \sin\alpha \end{aligned} \qquad \text{Eq. 1-32}$$

in which α is the angle between the *x*-axis of the laboratory coordinate system and the electric field vector of the incident light (Scheme 1-7).

Since the second-harmonic intensity is proportional to the square of the norm of the polarization, we can write for the intensity $I_x(2\omega)$ of the *x*-polarized second-harmonic light

$$\begin{aligned} I_x(2\omega) &\propto \left|\chi^{(2)}_{xxx}E_0^2\sin^2\alpha + \chi^{(2)}_{xyy}E_0^2\cos^2\alpha + 2\chi^{(2)}_{xyx}E_0^2\cos\alpha\sin\alpha\right|^2 \\ &\propto \left|\chi^{(2)}_{xxx}\sin^2\alpha + \chi^{(2)}_{xyy}\cos^2\alpha + 2\chi^{(2)}_{xyx}\cos\alpha\sin\alpha\right|^2 I(\omega)^2 \end{aligned} \qquad \text{Eq. 1-33}$$

If we describe the components of $\chi^{(2)}$ explicitly as complex numbers this equation subsequently becomes

$$I_x(2\omega) \propto \left|\begin{matrix} Re(\chi^{(2)}_{xxx})\cos^2\alpha + Re(\chi^{(2)}_{xyy})\sin^2\alpha + 2\,Re(\chi^{(2)}_{xyx})\sin\alpha\cos\alpha \\ +i[Im(\chi^{(2)}_{xxx})\cos^2\alpha + Im(\chi^{(2)}_{xyy})\sin^2\alpha + 2\,Im(\chi^{(2)}_{xyx})\sin\alpha\cos\alpha] \end{matrix}\right|^2 I(\omega)^2 \qquad \text{Eq. 1-34}$$

$$I_x(2\omega) \propto \left(\begin{matrix} [Re(\chi^{(2)}_{xxx})\cos^2\alpha + Re(\chi^{(2)}_{xyy})\sin^2\alpha + 2\,Re(\chi^{(2)}_{xyx})\sin\alpha\cos\alpha]^2 \\ +[Im(\chi^{(2)}_{xxx})\cos^2\alpha + Im(\chi^{(2)}_{xyy})\sin^2\alpha + 2\,Im(\chi^{(2)}_{xyx})\sin\alpha\cos\alpha]^2 \end{matrix}\right) I(\omega)^2 \qquad \text{Eq. 1-35}$$

$$I_x(2\omega) \propto \left(\begin{matrix} [Re^2(\chi^{(2)}_{xxx}) + Im^2(\chi^{(2)}_{xxx})]\cos^4\alpha + [Re^2(\chi^{(2)}_{xyy}) + Im^2(\chi^{(2)}_{xyy})]\sin^4\alpha \\ +4[Re^2(\chi^{(2)}_{xyx}) + Im^2(\chi^{(2)}_{xyx})]\sin^2\alpha\cos^2\alpha \\ +2[Re(\chi^{(2)}_{xxx})Re(\chi^{(2)}_{xyy}) + Im(\chi^{(2)}_{xxx})Im(\chi^{(2)}_{xyy})]\cos^2\alpha\sin^2\alpha \\ +2[Re(\chi^{(2)}_{xxx}\,Re(\chi^{(2)}_{xyx}) + Im(\chi^{(2)}_{xxx})Im(\chi^{(2)}_{xyx})]\sin\alpha\cos^3\alpha \\ +2[Re(\chi^{(2)}_{xyy}\,Re(\chi^{(2)}_{xyx}) + Im(\chi^{(2)}_{xyy})Im(\chi^{(2)}_{xyx})]\sin^3\alpha\cos\alpha \end{matrix}\right) I(\omega)^2 \qquad \text{Eq. 1-36}$$

Similarly to Equation 1-33, we can write the induced second order polarization P_y in the *y*-direction as

$$\begin{aligned} P_y &= \chi^{(2)}_{yxx}E_xE_x + \chi^{(2)}_{yyy}E_yE_y + \chi^{(2)}_{yyx}E_yE_x + \chi^{(2)}_{yxy}E_xE_y \\ &= \chi^{(2)}_{yxx}E_0^2\cos^2\alpha + \chi^{(2)}_{yyy}E_0^2\sin^2\alpha + 2\chi^{(2)}_{yyx}E_0^2\cos\alpha\sin\alpha \end{aligned} \qquad \text{Eq. 1-37}$$

And for the generated second-harmonic intensity with the electric field vector in the *y*-direction $I_y(2\omega)$, we can write

$$I_y(2\omega) \propto \left|\chi^{(2)}_{yxx} E_0^2 \cos^2\alpha + \chi^{(2)}_{yyy} E_0^2 \sin^2\alpha + 2\chi^{(2)}_{yyx} E_0^2 \cos\alpha \sin\alpha\right|^2$$
$$\propto \left|\chi^{(2)}_{yxx} \cos^2\alpha + \chi^{(2)}_{yyy} \sin^2\alpha + 2\chi^{(2)}_{yyx} \cos\alpha \sin\alpha\right|^2 I(\omega)^2 \quad \text{Eq. 1-38}$$

When we describe the second-harmonic susceptibility components $\chi^{(2)}_{ijk}$ explicitly as complex numbers this equation subsequently becomes

$$I_y(2\omega) \propto \left| \begin{matrix} Re(\chi^{(2)}_{yxx})\cos^2\alpha + Re(\chi^{(2)}_{yyy})\sin^2\alpha + 2\,Re(\chi^{(2)}_{yyx})\sin\alpha\cos\alpha \\ +i[Im(\chi^{(2)}_{yxx})\cos^2\alpha + Im(\chi^{(2)}_{yyy})\sin^2\alpha + 2\,Im(\chi^{(2)}_{yyx})\sin\alpha\cos\alpha] \end{matrix} \right|^2 I(\omega)^2 \quad \text{Eq. 1-39}$$

$$I_y(2\omega) \propto \left(\begin{matrix} [Re(\chi^{(2)}_{yxx})\cos^2\alpha + Re(\chi^{(2)}_{yyy})\sin^2\alpha + 2\,Re(\chi^{(2)}_{yyx})\sin\alpha\cos\alpha]^2 \\ +[Im(\chi^{(2)}_{yxx})\cos^2\alpha + Im(\chi^{(2)}_{yyy})\sin^2\alpha + 2\,Im(\chi^{(2)}_{yyx})\sin\alpha\cos\alpha]^2 \end{matrix} \right) I(\omega)^2 \quad \text{Eq. 1-40}$$

$$I_y(2\omega) \propto \left(\begin{matrix} [Re^2(\chi^{(2)}_{yxx}) + Im^2(\chi^{(2)}_{yxx})]\cos^4\alpha + [Re^2(\chi^{(2)}_{yyy}) + Im^2(\chi^{(2)}_{yyy})]\sin^4\alpha \\ +4[Re^2(\chi^{(2)}_{yyx}) + Im^2(\chi^{(2)}_{yyx})]\sin^2\alpha\cos^2\alpha \\ +2[Re(\chi^{(2)}_{yxx})Re(\chi^{(2)}_{yyy}) + Im(\chi^{(2)}_{yxx})Im(\chi^{(2)}_{yyy})]\cos^2\alpha\sin^2\alpha \\ +2[Re(\chi^{(2)}_{yxx}\,Re(\chi^{(2)}_{yyx}) + Im(\chi^{(2)}_{yxx})Im(\chi^{(2)}_{yyx})]\sin\alpha\cos^3\alpha \\ +2[Re(\chi^{(2)}_{yyy}\,Re(\chi^{(2)}_{yyx}) + Im(\chi^{(2)}_{yyy})Im(\chi^{(2)}_{yyx})]\sin^3\alpha\cos\alpha \end{matrix} \right) I(\omega)^2 \quad \text{Eq. 1-41}$$

These equations can be considerably simplified if we take into account the specific symmetry of the sample under study. For example, if there is a mirror plane present perpendicular to the sample plane, *e.g.* in the *xz* plane, all components with an uneven number of y-coefficients will vanish (Section 1.4). Equation 1-36 for the *x*-polarized second-harmonic intensity $I_x(2\omega)$ then simplifies to

$$I_x(2\omega) \propto \left(\begin{matrix} [Re^2(\chi^{(2)}_{xxx}) + Im^2(\chi^{(2)}_{xxx})]\cos^4\alpha + [Re^2(\chi^{(2)}_{xyy}) + Im^2(\chi^{(2)}_{xyy})]\sin^4\alpha \\ +2[Re(\chi^{(2)}_{xxx})Re(\chi^{(2)}_{xyy}) + Im(\chi^{(2)}_{xxx})Im(\chi^{(2)}_{xyy})]\cos^2\alpha\sin^2\alpha \end{matrix} \right) I(\omega)^2 \quad \text{Eq. 1-42}$$

Moreover, since the absolute phase of the susceptibility components is unknown we can equate one imaginary component, *e.g.* $Im(\chi^{(2)}_{yxx})$, to zero, simplifying Equation 1-42 to

$$I_x(2\omega) \propto \left(\begin{matrix} [Re^2(\chi^{(2)}_{xxx}) + Im^2(\chi^{(2)}_{xxx})]\cos^4\alpha + [Re^2(\chi^{(2)}_{xyy})]\sin^4\alpha \\ +2[Re(\chi^{(2)}_{xxx})Re(\chi^{(2)}_{xyy})]\cos^2\alpha\sin^2\alpha \end{matrix} \right) I(\omega)^2 \quad \text{Eq. 1-43}$$

Also for the *y*-polarized second-harmonic intensity $I_y(2\omega)$, we can simplify Equation 1-41 due to the symmetry of the mirror plane in the *xz* plane.

$$I_y(2\omega) \propto [4(Re^2(\chi^{(2)}_{yyx}) + Im^2(\chi^{(2)}_{yyx}))\cos^2\alpha \sin^2\alpha] I(\omega)^2 \qquad \text{Eq. 1-44}$$

Not knowing the absolute phase, we can drop the imaginary component $Im(\chi^{(2)}_{yxx})$ in this equation.

$$I_y(2\omega) \propto [4(Re^2(\chi^{(2)}_{yyx}))\cos^2\alpha \sin^2\alpha] I(\omega)^2 \qquad \text{Eq. 1-45}$$

Chapter 4 and 5 deal with a SHGM-study of adsorbate filled zeolite crystals, in which the adsorbate molecules solely are responsible for the generated second-harmonic. This means that following relation, which was first presented in Section 1.5.3, is applicable

$$\chi^{(2)}_{ijk} = Nf \sum_{i'j'k'=x'y'z'} \left\langle R_{ii'} R_{jj'} R_{kk'} \right\rangle \beta_{i'j'k'} \qquad \text{Eq. 1-46}$$

This means that the symmetry of the ensemble of adsorbate molecules is reflected in the allowed components of $\chi^{(2)}$. Moreover, within the same class of symmetry, differences in organization of the adsorbate molecules will be reflected in the relative values of the tensor components $\chi^{(2)}_{ijk}$. Thus, second-harmonic generation microscopy can be used as a tool for studying the spatial variation of molecular organization.

1.6.3 Two-photon fluorescence microscopy

Two-photon excited fluorescence (TPF) is very similar to the normal fluorescence process, with the difference that the fluorescent molecules are excited not by one photon, but by the simultaneous absorption of two photons. The molecule then releases its energy by emitting a fluorescent photon, as is the case for one-photon fluorescence.[23] The absorption cross section is many orders of magnitude smaller compared to one-photon fluorescence, since it is a higher order process.[24] More specifically, two-photon fluorescence is a third-order process.[23] Being an odd-order process means that no overall asymmetry is required to generate TPF, as is the case

for SHG. So the ability of fluorescent molecules to show TPF is independent of the symmetry of their ordering. This makes SHG and TPF complementary, since TPF will probe the presence of the molecules, while SHG will demonstrate the asymmetric organization of the molecules.

1.7 Alternative spatially resolved techniques to study host-guest systems

In this section an overview of the imaging techniques that so far have been used to study host-guest systems is given. This is done to provide the background towards which the inherent advantages of SHGM must be placed.

1.7.1 Fluorescence microscopy

Fluorescence microscopy has been used to study the intergrown structure of zeolite crystals. One strategy is to visualise coke formation and intermediates during template removal with optical and fluorescence microscopy.[25] This reveals diffusion barriers and hence visualizes the different intergrown parts of the crystal. Complementary techniques, like EBSD and AFM are used in addition to deduce the orientation of the different crystal parts.[26, 27] Another strategy is to use a molecular probe which preferentially adsorbs on one type of crystal plane. For example, DAMPI (4-(4'-diethylaminostyryl)-1-methylpyridinium iodide) adsorbs preferentially in the *b*-pores of ZSM-5, accessible on the (010) planes, and does not adsorb in the *a*-pores, accessible from the (100) planes. Visualizing the preferential adsorption of DAMPI with fluorescence microscopy provides the crystallographic orientation of the different crystal parts.[28]

Fluorescence microscopy has also been used to study catalysis in zeolites *in situ*. More specifically the self-condensation of furfuryl alcohol in the liquid phase catalyzed by H-ZSM-5[26, 29] and the coke formation during methanol-to-olefin conversion in the gas phase catalyzed by H-ZSM-5 and H-SAPO-34 have been studied.[30] This yields spatially resolved information on the catalytic activity of individual crystals, and indirectly provides information on the intergrown structure of the crystals. During an epoxidation

reaction in Ti-MCM-41, intraparticle diffusion limitations have been studied with fluorescence microscopy.[31]

We can conclude that fluorescence microscopy can provide a wealth of information concerning intergrown crystal structure, catalytic activity and diffusion. However, as fluorescence generation is allowed in centrosymmetric media, a strategy must be employed to minimize the fluorescent background. Therefore, the mentioned studies are either *ex situ* studies, or, when they are *in situ*, the formation of fluorescent oligomerized and polymerized substances that can hardly diffuse out of the pores has been followed, or the applied concentration was so low that single molecule fluorescence of the formed products was observed.

1.7.2 Interference microscopy and IR-imaging

Interference microscopy is based on the interference pattern generated by the superposition of two light beams, one beam that passes through the microporous material, and another beam that passes through the surrounding atmosphere. Since the refractive index of the microporous material is dependent on the concentration of guest molecules, changes of local concentration appear in the interference pattern. This allows measuring intracrystalline diffusivities through measuring the transient intracrystalline concentration profiles during adsorption and desorption experiments. This has been done for zeolites of the LTA,[32] MFI[33,34] and AFI[35,36,37] structure type and zeolite ferrierite.[38] The spatial resolution of the method allows determining the concentration dependency of the diffusivity, instead of assuming a concentration independent diffusivity as is done in more conventional methods. Moreover, depending on the geometry of the pore system of the studied material, it allows to calculate the diffusivity through the different pore types, instead of assuming diffusion only through the widest pores. In addition the contribution of surface permeability can be determined.[33,36,38]

IR-imaging can be employed to achieve similarly detailed information on diffusion in microporous materials.[38,39] Whereas interference microscopy has a spatial resolution of ~0.5x0.5 µm², IR-imaging has a spatial resolution of only 2.7x2.7µm².[39] However, it has

the advantage of chemical specificity which allows to distinguish between different adsorbates, hence counterdiffusion can be studied.[40]

In some cases, the diffusion patterns obtained by interference microscopy and IR-microscopy reveal diffusion barriers that can be related to the border of different parts of an intergrown crystal structure. This has been shown for AFI-type zeolites CrAPO-5 and SAPO-5.[35,37] Also, the permeability across the interfaces between intergrown parts can be quantified by interference microscopy, this has been done for isobutane adsorption and desorption in silicalite-1 with an hourglass shaped intergrown structure.[33]

For the *in situ* study of microporous materials, both interference microscopy and IR-imaging have so far only been used in the gas phase. For interference microscopy this is likely due to the smaller difference in refractive index between a solvent-filled zeolite and a zeolite filled with solvent and adsorbate molecules, as compared to the difference in refractive index between an empty zeolite and a an adsorbate-filled zeolite. In IR-imaging, it is hard to distinguish between the infrared absorbance of a molecule in the liquid phase versus the absorbance of the same molecule adsorbed in a pore.

1.7.3 Pyro-electric imaging

Pyro-electric materials are materials with a permanent polarization. Every permanent polarization changes when the temperature is changed, and it is that change in polarization that is probed in pyro-electric measurements. Microporous materials that are filled with dipolar molecules in a dipolar arrangement, have a permanent polarization, which means that they generate SHG, and that they show the pyro-electric effect. A pyro-electric measurement provides *i.a.* the sense of the polarization.

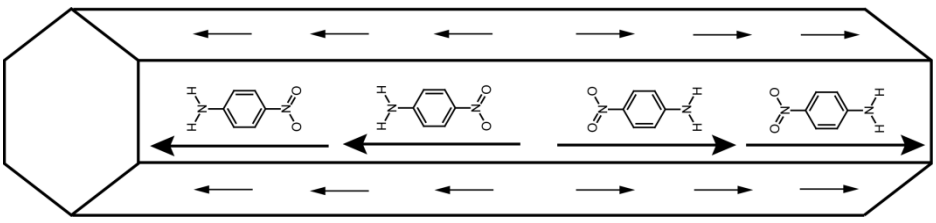

Scheme 1-8: Dipole moments in PNA-filled AlPO-5. The large arrows represent the dipole moments of the PNA molecules, the small arrows represent the lattice polarization. Dipole vectors point from negative to positive charge.

If the change in temperature is caused by laser-induced heating, we can map the pyro-electric effect over a crystal by changing the position of the laser bundle on the crystal. This has been done for AlPO-5 filled with *p*-nitroaniline (PNA). For such crystals, it has been found that the two halves have a polarization with opposite direction, as in shown in Scheme 1-8.[41,42] This means that the nitrogroups point towards the centre of the crystal. The empty AlPO-5 crystals also show the same polarization reversal, albeit with a much smaller polarization magnitude.[43] This leaves two possible explanations for the formation of the PNA-dipole chains. Either the polar structure of AlPO-5 induces the ordering, or it is induced by a surface selection process in which PNA enters the pores with one side preferentially. The first explanation seems unlikely because at the loading temperature (150°C) the crystal is no longer pyro-electric, meaning that most likely the polarization is also zero, and thus, has no influence on the loading process.[43] The surface selection process is in accordance with the observation that the transport from the gas phase into the pores is presumed to occur via adsorption on the external surface.[44,45] Klap et al.[43] gave an explanation for the surface selection process for PNA on AlPO-5 crystals. They deduced from XRD-measurement that the end-planes of an AlPO-5 crystal are planes which expose the aluminium atoms. These aluminium atoms may be three coordinated with an empty coordination position at the exterior, but they most likely are four coordinated with a hydroxylgroup at the outer surface. In both cases, the surface is more likely to interact with the nitrogroup than with the aminegroup. Hence, PNA adsorbs on the external surface predominantly with its nitro-group. If PNA then retains its orientation upon adsorption into the pores, this leads to dipolar PNA chains with the experimentally observed sense of polarization.

From pyro-electric measurements, also information on the cooperative behaviour of the adsorbed molecules can be deduced. For the PNA-AlPO-5 system the pyro-electric coefficient is much larger around 90°C than at room temperature. This indicates that at 90°C the molecules respond to the heat as single molecules, while at lower temperatures the molecules respond to the temperature change via a cooperative motion of many molecules.[42] This is in agreement with the observation that at room temperature the PNA molecules in AlPO-5 can be present as hydrogen bonded chains, while these bonds break at elevated temperatures.[46]

1.8 Thesis objectives and outline

As seen in section 1.5, second-harmonic generation is particularly suited to study molecular interfaces without contribution of the surrounding (centrosymmetric) medium. Since most analysis techniques lack this inherent surface specificity, it is possible with SHG to obtain information that cannot be acquired by other techniques. Nevertheless, most studies on the orientation of molecular (sub)monolayers have been performed in the gas phase[47,48,49,12] and studies on the dynamics of adsorption are scarce.[50,51] Additionally, SHG has so far only been used to a limited extent to study zeolites: only SHG-studies of zeolite crystals dye-loaded outside the SHG-apparatus are available so far (see section 2.1). Therefore, it is our aim to explore the full potential of SHG in measuring *dynamic* events in zeolites in the *liquid phase*. In chapter 2, we employ SHG to study the adsorption of an organic molecule into the pore-mouth of a liquid immersed zeolite *in situ.* Moreover, the dynamics of the orientation of the adsorbate molecules during the adsorption process are probed. In chapter 3 it is shown that SHG can be used to follow the diffusion of an organic molecule through a film buried under a liquid phase *in situ*. More specifically, a spin-coated zeolite precursor film has been employed.

The last decade second-harmonic generation microscopy has emerged as a new tool. However, most reports focus on biological applications.[52] In materials science SHGM has been applied far more scarcely. However, a few studies on *e.g.* liquid crystals,[53] molecular monolayers,[54] nanoparticles,[55,56] ferroelectric crystals,[57] and polymers[58] are available. Several of these studies show that indeed SHGM is sensitive to molecular and supramolecular organization as mentioned in Section 1.6.[53,54,58] Moreover, it has been shown that dipolar molecules adsorbed in zeolites frequently give rise to SHG due to their organization in macroscopic dipole chains inside the pores. This is due to surface selection, which means that one functional group of the adsorbate is preferentially adsorbed (see chapter 4 and 5). In this thesis we exploit the SHGM to elucidate *molecular organization* in zeolite pores with *spatial resolution*. In Chapter 4 and 5 this is done for respectively PNA-loaded zeolite ZSM-5 and SAPO-5.

References

1 Guisnet, M.; Gilson, J.-P. Introduction to Zeolite Science and Technology. In: Zeolites for Cleaner Technologies (1st Edition). Guisnet.M.; Gilson, J.-P. (Eds.), Imperial College Press, 2002.
2 Maesen, Th.L.M.; Marcus, B.The zeolite Scene. In: Introduction to zeolite science and practice (2nd Edition). van Bekkum, H.; Flanigen, E.M.; Jacobs, P.A.; Jansen, J.C. (Eds.), Elsevier, 2001.
3 Methivier, A. Separation of paraxylene by adsorption. In: Zeolites for Cleaner Technologies (1st Edition). Guisnet.M.; Gilson, J.-P. (Eds.), Imperial College Press, 2002.
4 Maxwell, I.E.; Stork, W.H.J. Hydrocarbon processing with zeolites. In: Introduction to zeolite science and practice (2nd Edition). van Bekkum, H.; Flanigen, E.M.; Jacobs, P.A.; Jansen, J.C. (Eds.), Elsevier, 2001.
5 Alario, F.; Guisnet, M. Para-Xylene Manufacturing: Catalytic Reactions and Processes. In: Zeolites for Cleaner Technologies (1st Edition). Guisnet.M.; Gilson, J.-P. (Eds.), Imperial College Press, 2002.
6 Smit, B.; Maesen, T.L.M. *Nature* **2008**, *451*, 671.
7 Meier, W.M.; Olson, D.H. Atlas of Zeolite Structure Types (3rd Edition), Butterworth-Heinemann, 1992.
8 Verbiest, T.; Clays, K; Rodriguez, V. Second-Order Nonlinear Optical Characterization Techniques (1st Edition), CRC Press, 2009, Chapter 1.
9 Shen, Y.R. The Principles of Nonlinear Optics (1st Edition), John Wiley & Sons, 1984, p.24.
10 Shen, Y.R. The Principles of Nonlinear Optics (1st Edition), John Wiley & Sons, 1984, chapter 25.3.
11 Zhuang, X.; Miranda, P.B.; Kim, D.; Shen, Y.R. *Phys. Rev. B* **1999**, *59*, 12632.
12 Wei, X.; Hong, S.-C.; Zhuang, X.; Goto, T.; Shen Y.R. *Phys. Rev. E* **2000**, *62*, 5160.
13 Corn, R. M.; Higgins, D. A. *Chem. Rev.* **1994**, *94*, 107.
14 Rao, Y.; Tao, Y.-s.; Wang, H.-f. *J. Phys. Chem.* **2003**, *119*, 5226.
15 Zhang, W.-k.; Wang, H.-f.; Zheng, D.-s. *Phys. Chem. Chem. Phys.* **2006**, *8*, 4041.
16 Shim, T.K.; Kim, D.; Lee, M.H.; Rhee, B.K.; Cheong, H.M.; Kim, H.S.;Yoon, K.B. *J.Phys.Chem.B* **2006**, *110*, 16874.
17 Cheng, L.T.; Tam, W.; Stevenson, S.H.; Meredith, G.R. *J.Phys.Chem.* **1991**, *95*, 10631.
18 Li, Z.; Wu, K.; Su, G.; He, Y. *Opt. Mater.* **2002**, *20*, 295.
19 Lalama, S.J.; Garito, A.F. *Phys. Rev. A* **1979**, *20*, 1179.
20 Shen, Y.R. *Nature* **1989**, *337*, 519.
21 Simpson, G.J.; Rowlen, K.L. *J. Am. Chem. Soc.* **1999**, *121*, 2635.
22 Simpson, G.J.; Westerbuhr, S.G.; Rowlen, K.L. *Anal. Chem.* **2000**, *72*, 887.
23 Verbiest, T.; Clays, K; Rodriguez, V. Second-Order Nonlinear Optical Characterization Techniques (1st Edition), CRC Press, 2009, Chapter 5.
24 Shen, Y.R. The Principles of Nonlinear Optics (1st Edition), John Wiley & Sons, 1984, p.202.
25 Karwacki, L.; Stavitski, E.; Kox, M.H.F.; Kornatowski, J.; Weckhuysen, B.M. *Ang. Chem. Int. Ed.* **2007**, *119*, 7366.
26 Roeffaers, M.B.J.; Ameloot, R.; Bons, A.-J.; Mortier, W.; De Cremer, G.; de Kloe, R.; Hofkens, J.; De Vos, D.E.; Sels, B.F. *J. Am. Chem. Soc.* **2008**, *130*, 13516.
27 Karwacki, L.; Kox, M.H.F.; de Winter, D.A.M.; Drury, M.R.; Meeldijk, J.D.; Stavitski, E.; Schmidt, W.; Mertens, M.; Cubillas, P.; John, N.; Chan, A.; Kahn, N.; Bare, S.R.; Anderson, M.; Kornatowski, J.; Weckhuysen, B.M. *Nature Mater.* **2009**, *8*, 959.
28 Roeffaers, M.B.J.; Ameloot, R.; Baruah, M.; Uji-i, H.; Bulut, M.; De Cremer, G.; Müller, U.; Jacobs, P.A.; Hofkens, J.; Sels, B.F.; De Vos, D.E. *J. Am. Chem.Soc.* **2008**, *130*, 5763.
29 Roeffaers, M.B.J.; Sels, B.F.; Uji-i, H.; Blanpain, B.; L'hoëst, P.; Jacobs, P.A.; De Schryver, F.C.; Hofkens, J.; De Vos, D.E. *Angew. Chem. Int. Ed.* **2007**, *46*, 1706.
30 Mores, D.; Stavitski, E.; Kox, M.H.F.; Kornatowski, J.; Olsbye, U.; Weckhusyen, B. *Chem. Eur. J.* **2008**, *14*, 11320.
31 De Cremer, G.; Roeffaers, M.B.J.; Bartholomeeusen, E.; Kaifeng, L.; Dedecker, P.; Pescarmona, P.; Jacobs, P.A.; De Vos, D.E.; Hofkens, J.; Sels, B.F. *Angew. Chem. Int. Ed.* **2010**, *49*, 908.
32 Schemmert, U.; Kärger, J.; Krause, C.; Weitkamp, J. *Microporous Mesoporous Mater.* **1999**, *32*, 101.
33 Geier, O.; Vasenkov, S.; Lehmann, E.; Kärger, J.; Schemmert, U.; Rokoczy, R.A.; Weitkamp, J. *J. Phys. Chem. B* **2001**, *105*, 10217.

34 Chmelik, C.; Kortunov, P.; Vasenkov, S.; Kärger, J. *Adsorption* **2005**, *11*, 455.
35 Lehmann, E.; Chmelik, C.; Scheidt, H.; Vasenkov, S.; Staudte, B.; Kärger, J.; Kremer, F.; Zadrozna, G.; Kornatowski, J. *J. Am. Chem. Soc.* **2002**, *124*,8690.
36 Lehmann, E.; Vasenkov, S.; Kärger, J.; Zadrozna, G.; Kornatowski, J. *J. Chem. Phys.* **2003**, *118*, 6129.
37 Lehmann, E.; Vasenkov, S.; Kärger, J.; Zadrozna, G.; Kornatowski, J.; Weiss, Ö; Schüth, F. *J. Phys. Chem. B* **2003**, *107*, 4685.
38 Heinke, L.; Chmelik, C.; Kortunov, P.; Ruthven, D.M.; Shah, D.B.; Vasenkov, S.; Kärger, J. *Chem. Eng. Technol.* **2007**, *30*, 995.
39 Chmelik, C.; Hibbe, F.; Tzoulika, D.; Heinke, L.; Caro, J.; Li, J.; Kärger, J. *Microporous Mesoporous Mater.* **2010**, *129*, 340.
40 Chmelik, C.; Heinke, L.; van Baten J.M.; Krishna, R. *Microporous Mesoporous Mater.* **2009**, *125*, 11.
41 Marlow, F.; Wübbenhorst, M.; Caro, J. *J. Phys. Chem.* **1994**, *98*, 12315.
42 Klap, G.J.; van Klooster, S.M.; Wübbenhorst, M.; Jansen, J.C.; van Bekkum, H.; van Turnhout, J. *J. Phys. Chem. B* **1998**, *102*, 9518.
43 Klap, G.J.; Wübbenhorst, M.; Jansen, J.C.; van Koningsveld, H.; van Bekkum, H.; van Turnhout, J. *Chem. Mater.* **1999**, *11*, 3497.
44 Barrer, R.M. *J. Chem. Soc. Faraday Trans.* **1990**, *86*, 1123.
45 Jentys, A.; Tanaka, H.; Lercher, J.A. *J. Phys. Chem. B* **2005**, *109*, 2254.
46 Marlow, F.; Demuth, D.; Stucky, G.; Schüth, F. *J. Phys. Chem.* **1995**, *99*, 1306.
47 Heinz, T.F.; Tom, H.W.K.; Shen, Y.R. *Phys.Rev.A* **1983**, *28*, 1883.
48 Xu, J.; Lu, X.; Zhou, G.; Zhang, Z. *Thin Solid Films* **1998**, *312*, 295.
49 Inoue, T.; Moriguchi, M.; Ogawa, T. *Thin Solid Films* **1999**, *350*, 238.
50 Dannenberger, O.; Buck, M.; Grunze, M. *J.Phys.Chem.***1999**, *103*, 2202.
51 Wang, H.; Troxler, T.; Yeh, A.-G.; Dai, H.-L. *Langmuir* **2000**, *16*, 2475.
52 Mertz, J. *Curr. Opin. Neurobiol.* **2005**, *14*, 610.
53 Morales-Saavedra, O.G.; Bulat, M.; Rauch, S.; Heppke, G. *Mol. Cryst. Liq. Cryst.* **2004**, *413*, 607.
54 Anceau, C.; Brasselet, S.; Zyss, J. *Chem. Phys. Lett.* **2005**, *411*, 98.
55 Beermann, J.; Bozhevolnyi, S.I. *Phys. Rev. B* **2004**, *69*, 155429.
56 Delahaye, E.; Tancrez, N.; Yi, T.; Ledoux, I.; Zyss, J.; Brasselet, S.; Clément, R. *Chem. Phys. Lett.* **2006**, *429*, 533.
57 Bozhevolnyi, S.I.; Hvam, J.M.; Pedersen, K.; Laurell, F.; Karlsson, H.; Skettrup, T.; Belmonte, M. *Appl. Phys. Lett.* **1998**, *73*, 1814.
58 Xu, J.; Bao, J.; Guo, B.-H.; Ma, H.; Yun, T.-L.; Gao, L.; Chen, G.-Q.; Iwata, T. *Polymer*, **2007**, *48*, 348.

Chapter 2: *In Situ* Orientation-Sensitive Observation of Molecular Adsorption on a Liquid/Zeolite Interface by Second-Harmonic Generation

Abstract

The inherently surface-specific technique of second-harmonic generation was employed to probe the adsorption of an organic molecule, a hemicyanine dye, on *b*-oriented silicalite-1 films *in situ*. Measurements were performed in a purpose-built cell for solution experiments. By measuring at two different polarization combinations of the fundamental and second-harmonic light, the orientation of the adsorbed molecules was measured continuously. It has been observed that the adsorbed molecules gradually align themselves with the straight pores of the zeolite crystallites, thus adsorbing into the pores.

Solid/liquid interfaces are not only abundant in daily life examples, with examples ranging from paints[1], soils[2] and cosmetics[3] to cleaning products,[4] but also in industry, for example in heterogeneous catalysis[5] and fuel cells.[6] Many industrial catalysts not only have a high surface area at the external surface of the particles but also have mesopores (2-50 nm) and micropores (< 2 nm)[7] that contain a large number of active sites that contribute to the overall catalytic activity. For instance, in zeolites, which are crystalline microporous aluminosilicates, the outcome of a reaction is determined by the subtle interplay between adsorption into the pores, diffusion within the pores, and chemical conversion at the sites that are distributed over the crystal.[8] To understand phenomena such as shape selectivity in zeolite-catalyzed reactions, it is important to study each of these elementary steps.

The kinetics of adsorption from the gas phase into a zeolite can be studied with a series of techniques. The most useful of these are IR spectroscopy,[9] IR microscopy,[10] and interference microscopy,[11] as they are capable of providing molecular or spatially resolved information. Other analysis methods, such as gravimetry[12] and ellipsometry[13] provide uptake rate curves from which this information can hardly be distilled. That the initial adsorption into the zeolite crystal can indeed be complex has been shown for the gas-phase adsorption of aromatics: fast time-resolved IR spectroscopy has suggested that the molecules first physisorb at the outer crystal surface, followed by a slower adsorption into the pores.[9] For liquid-phase adsorption, the techniques available are scarcer and moreover can only probe uptake rates.[14,15] However, such experiments do not allow us to distinguish between the various steps in an adsorption process. Spectroscopic methods would be particularly suitable to provide insight in the subtleties of an adsorption process because they yield molecular information. However, linear spectroscopic techniques, like UV-Vis and IR spectroscopy, would also detect contributions of the bulk liquid phase. Even ATR-IR spectroscopy would suffer from significant bulk contributions.

Even-order nonlinear optical techniques, like second-harmonic generation (SHG) and sum-frequency generation (SFG) are intrinsically surface-specific techniques in which the interference of most bulk phases is forbidden in the electric dipole approximation and thus nonexistent.[16,17] Because electronic excitations are more efficient than the

vibrational excitations studied by SFG, we used second-harmonic generation in this study. Whereas several studies of organic molecules at a liquid/solid interface by SHG and SFG are on hand,[17,18,19,20,21,22] only two real-time kinetic studies of molecular adsorption without application of an external electric field are available.[23,24] Here, we report the first *in situ* adsorption SHG study of an organic molecule on a solid/zeolite interface. Earlier SHG studies on zeolites were *ex situ* studies of samples that were loaded with dyes outside the SHG apparatus. Previously, the orientation of molecules adsorbed in zeolites has been studied by various techniques, though only under equilibrium conditions.[25,26,27] As will be demonstrated, an additional advantage of the SHG technique is that the orientation of the molecules during the adsorption process can be monitored, which allows an insight in the adsorption process itself.

The silicalite-1 films in this study were prepared on a Si wafer, on the basis of a procedure described in literature.[28] In Figure 2-1, a typical SEM image is presented, which shows that the film consists mainly of *b*-oriented crystallites with tablet habit and only a minor fraction of the substrate is not covered with crystallites. Furthermore, few crystals have grown on top of this layer and are tilted over 90° in comparison to the *b*-oriented crystallites. The XRD pattern, shown in Figure 2-2, exhibits only (0 *k* 0) peaks; this confirms the predominant *b* orientation of the crystallites.

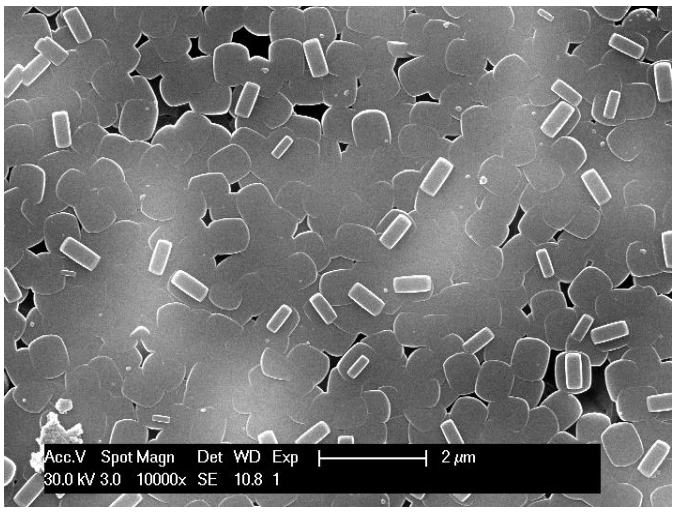

Figure 2-1: SEM image of a typical silicalite-1 substrate film.

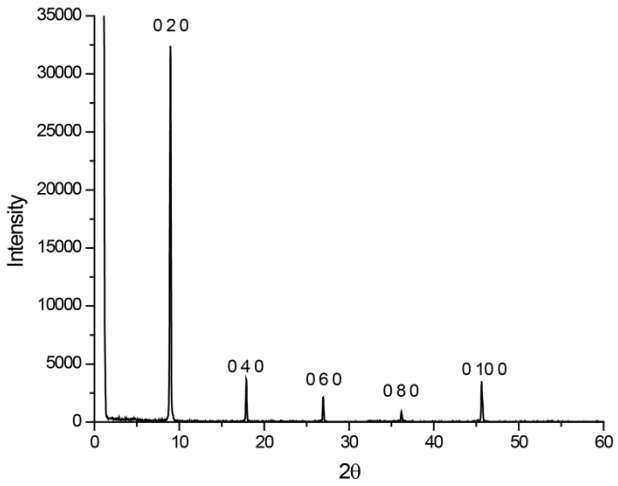

Figure 2-2: X-ray diffractogram of a typical silicalite-1 substrate film.

The SHG experiments were performed with the setup depicted in Figure 2-3, using a Ti:Sapphire laser (Tsunami, Spectra-Physics) which produces ~100 fs pulses at 800 nm at a repetition rate of 80 MHz. The polarization of the incoming beam is selected with a half-wave plate ($\lambda/2$). The fundamental light, with an incident angle of 67.5°, is then focused on the sample, which is placed vertically in a 100 ml octagonal cell (Figure 2-3); the path length for both the incoming and the second-harmonic light is 3.62 cm. The angle of 67.5° was chosen because at this angle the direction of both the incoming and the second-harmonic light are perpendicular with respect to the windows. An analyzer is used to select the polarization of the SHG signal, and filters are used to separate the SHG signal from the fundamental and background light. As a detector, a photomultiplier tube (XP2020, Philips) is employed with a lock-in amplifier (SR830, Stanford Research Systems) and chopper (~1 kHz, custom-made) to reduce background noise on top of the signal. The laser output power is measured with a Photodiode (S1722, Hamamatsu) to ensure that it is constant during the measurement. During the adsorption SHG experiments the cell was filled with 100 ml of 1-hexanol (Acros, 98%) and 1 ml of a 1 mM solution of DAMPI (4-(4-diethylaminostyryl)-1-methylpyridinium iodide; BioChemika, ≥97%) was injected to obtain a final DAMPI concentration of 10 μM. In each experiment, we verified that the generated signal was not due to nonlinear scattering processes by performing angle-dependent measurements. Moreover, a signal was observed only when the focus of the fundamental laser beam coincides with the DAMPI

layer, thus it can be concluded that the signal does not originate from the solution through nonlinear scattering processes.

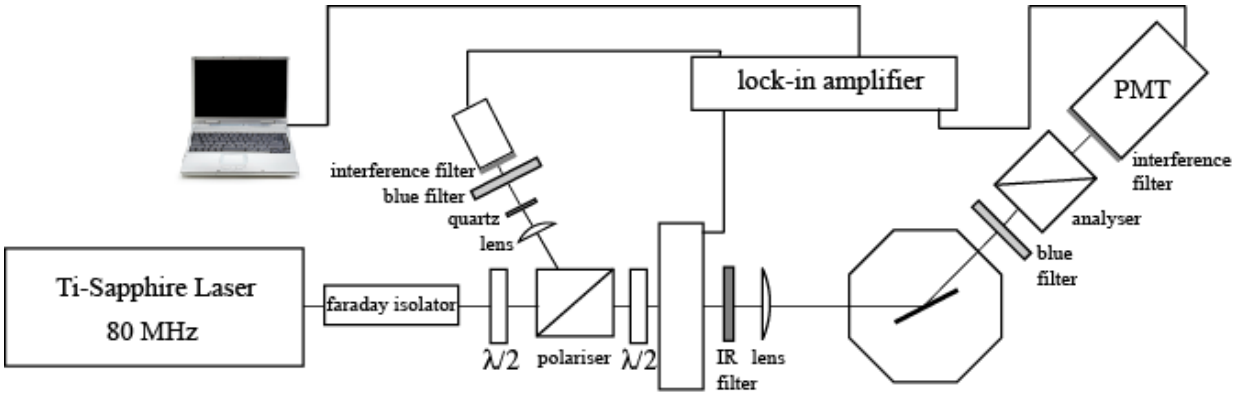

Figure 2-3: Layout of the SHG system. λ/2 - half-wave plate for 800 nm; IR filter - filter blocking 400 nm light; blue filter - filter blocking 800 nm light; PMT - photomultiplier tube; PD - Photodiode.

The zeolite substrate films are theoretically treated as azimuthally isotropic. Although the individual silicalite-1 crystallites possess orthorhombic symmetry, azimuthal isotropy of the zeolite substrate films can be expected because individual *b*-oriented crystallites are positioned randomly on the substrate (see Figure 2-1). This was confirmed by the SHG measurements.

In a substrate-adsorbate system the second-harmonic intensity is directly proportional to the square of the amplitude of the nonlinear susceptibility $\chi_{tot}^{(2)}$, described by[29]

$$\chi_{tot}^{(2)} = \chi_{sub}^{(2)} + \chi_{\mathrm{int}}^{(2)}(\theta(t)) + \chi_{ads}^{(2)}(\theta(t)) \qquad \text{Eq. 2-1}$$

Therefore, second-harmonic generation can originate from the substrate ($\chi_{sub}^{(2)}$), the interaction between the substrate and adsorbate ($\chi_{int}^{(2)}$), and the adsorbate ($\chi_{ads}^{(2)}$). Because DAMPI exhibits a very large quadratic nonlinearity,[30] the terms $\chi_{int}^{(2)}$ and $\chi_{sub}^{(2)}$ are expected to be negligible with respect to the adsorbate term $\chi_{ads}^{(2)}$. Hence, only $\chi_{ads}^{(2)}$ is dependent upon the adsorbate coverage $\theta(t)$ in our system.

In reflection geometry, the effective nonlinear susceptibility, measured at the input and output polarization combinations PP (*p*-input, *p*-output) and SP (*s*-input, *p*-output), takes the forms[31]

$$\chi^{(2)}_{eff,PS} = L_{ZZ}(2\omega)\ L_{YY}(\omega)\ ^2 \sin\gamma(\chi^{(2)}_{ads})_{ZYY}$$
$$\chi^{(2)}_{eff,PP} = +L_{ZZ}(2\omega)\ L_{XX}(\omega)\ ^2 \sin\gamma\cos^2\gamma(\chi^{(2)}_{ads})_{ZXX}$$
$$-2L_{XX}(2\omega)L_{ZZ}(2\omega)L_{XX}(2\omega)\sin\gamma\cos^2\gamma(\chi^{(2)}_{ads})_{XZX}$$
$$+L_{ZZ}(2\omega)\ L_{ZZ}(\omega)\ ^2 \sin^3\gamma(\chi^{(2)}_{ads})_{ZZZ}$$

Eq. 2-2

In the above equations, $L_{ii}(\Omega)$ are the Fresnel factors, and γ is the incident angle of the fundamental light. The subindices refer to the laboratory coordinates (X,Y,Z) as depicted in Scheme 2-1.

Hemicyanine dyes such as DAMPI have one dominant second-order nonlinear polarizability β_{zzz} with z along the long molecular axis.[32] The hyperpolarizability β_{zzz} can be related by a coordinate transformation to the different elements of $\chi^{(2)}_{ads}$ in the laboratory coordinates (X,Y,Z) (Scheme 2-1). If the adsorbate molecules have no preferred direction in the plane, and α is the angle between the molecular axis z and the surface normal Z, then[33,34]

$$(\chi^{(2)}_{ads})_{ZZZ} = N_s\beta_{zzz}\left\langle\cos^3\alpha\right\rangle$$
$$(\chi^{(2)}_{ads})_{ZXX} = (\chi^{(2)}_{ads})_{ZYY} = (\chi^{(2)}_{ads})_{YZY} = (\chi^{(2)}_{ads})_{XZX} = \frac{1}{2}N_s\beta_{zzz}\left\langle\cos\alpha\sin^2\alpha\right\rangle$$

Eq. 2-3

in which N_s is the surface concentration and the brackets refer to the orientational average. We have omitted the local-field factors in the equations because their effect can be included in the Fresnel factors as shown by Zhuang et al.[31] The ratio of the components of $\chi^{(2)}_{ads}$ allows us to determine the molecular orientation. For this aim, it is convenient to define A as

$$A = \frac{2(\chi^{(2)}_{ads})_{XZX}}{(\chi^{(2)}_{ads})_{ZZZ.} + 2(\chi^{(2)}_{ads})_{ZXX}} = \frac{\left\langle\sin^2\alpha\cos\alpha\right\rangle}{\left\langle\cos\alpha\right\rangle}$$

Eq. 2-4

If the orientational distribution can be approximated by a δ-distribution, then the tilt angle α can be obtained directly through A as $\alpha = \sin^{-1}\sqrt{A}$. Both $(\chi^{(2)}_{ads})_{ZZZ}$ and $(\chi^{(2)}_{ads})_{ZXX}$ can be obtained by measuring at two different polarization combinations, for example, in a PP and a SP configuration.

Because the majority of the zeolite crystallites are *b*-oriented (*vide supra*), it is predominantly the straight pores of the zeolite film that are accessible for adsorption, whereas most zigzag pores are inaccessible as can be seen from Scheme 2-1. Moreover, the straight pores are oriented along the surface normal. Whereas DAMPI should be able to adsorb into these pores with its stilbazolium moiety,[35] the amine head cannot enter because of steric hindrance. In other words, DAMPI behaves as a 'nail' (Scheme 2-1).[36] This is an important point because in this case DAMPI can be present only as a monolayer. Because the nonlinearity of the DAMPI layer dominates the observed SHG signal (*vide infra*), we can treat the generated SHG within the electric dipole approximation. Although in theory electric quadrupole and magnetic dipole contributions could be present, it is well established that they are usually much smaller than the electric dipole response in this type of material.[37,38]

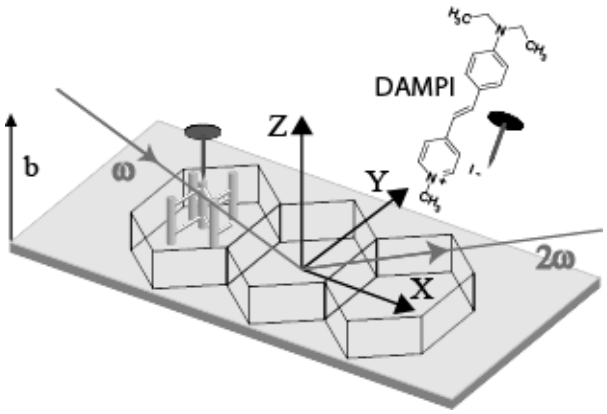

Scheme 2-1: Outline of the experiment. Scheme of *b*-oriented silicalite-1 crystallites on a substrate. The two-dimensional pore system, with straight pores normal to the surface and zigzag pores in plane with the substrate, is depicted, as is DAMPI and its behavior as a 'nail'. The laboratory coordinates X,Y,Z are shown along with the incoming fundamental beam with a frequency of ω and the generated second-harmonic beam with a doubled frequency of 2ω.

The adsorption of DAMPI was probed *in situ* with SHG by collecting both the *p*-polarized second-harmonic for a *p*-polarized fundamental ($I(2\omega)_{pp}$) and the *s*-polarized fundamental ($I(2\omega)_{sp}$) (Figure 2-4a,b). Additionally, the ratio $I(2\omega)_{pp}/I(2\omega)_{sp}$ was recorded (Figure 2-4c). From Equation 2-3, it is clear that $(\chi^{(2)}_{ads})_{ZZZ}$ will increase with a decreasing value of α, *i.e.* at a more perpendicular orientation of DAMPI towards the surface, and vice versa for $(\chi^{(2)}_{ads})_{ZXX}$. Because $I(2\omega)_{sp}$ probes only the tensor component $(\chi^{(2)}_{ads})_{ZXX}$ while $I(2\omega)_{pp}$ probes both $(\chi^{(2)}_{ads})_{ZZZ}$ and $(\chi^{(2)}_{ads})_{ZXX}$, the ratio $I(2\omega)_{pp}/I(2\omega)_{sp}$ will increase with a more perpendicular orientation of DAMPI.

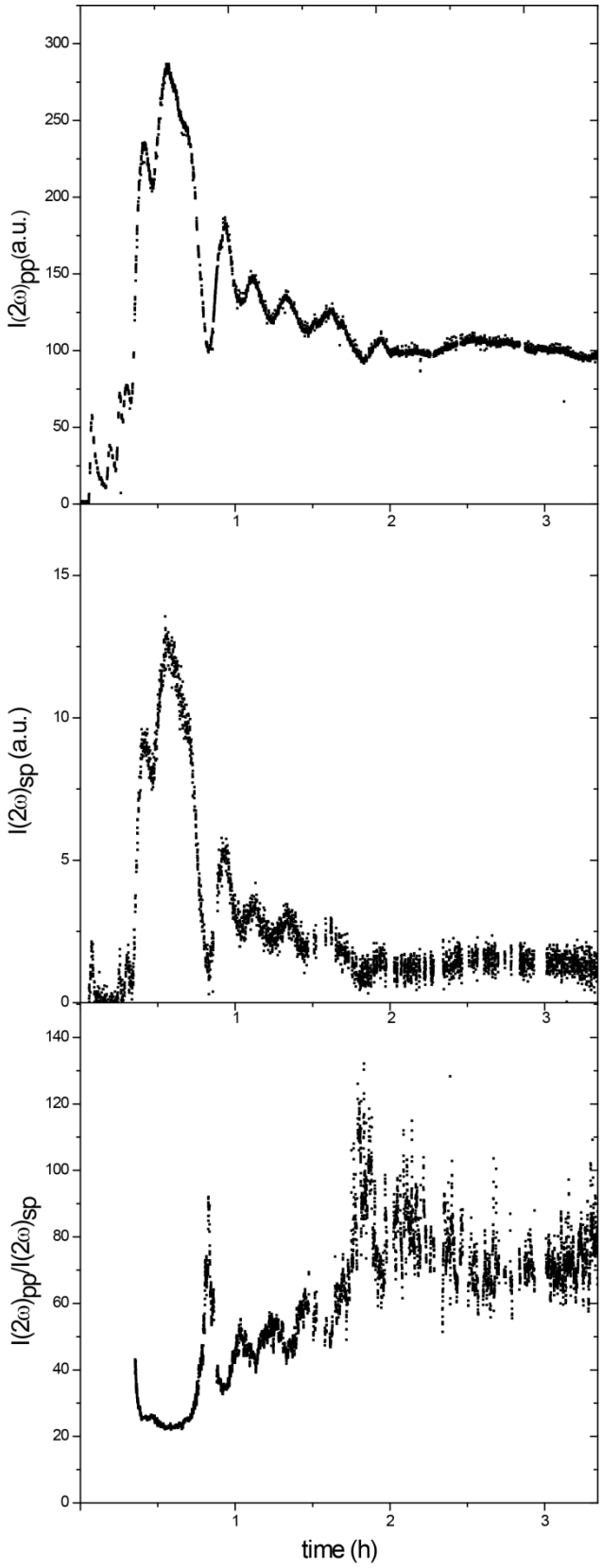

Figure 2-4: Variation of the SHG signal intensity with time after the injection of DAMPI in (a) *p*-input / *p*-output polarization configuration ($I(2\omega)_{pp}$), and (b) *s*-input / *p*-output polarization configuration ($I(2\omega)_{sp}$). (c) Variation of the ratio $I(2\omega)_{pp}/I(2\omega)_{sp}$ with time after injection of DAMPI.[39]

Before addition of the adsorptive, no SHG signal could be distinguished from the noise. After addition of DAMPI, a sharp increase in both second-harmonic signals $I(2\omega)_{pp}$ and $I(2\omega)_{sp}$ was observed (Figure 2-4a,b) indicating the adsorption of DAMPI onto the zeolite. After nearly 2 h, both $I(2\omega)_{pp}$ and $I(2\omega)_{sp}$ stabilize, indicating that the DAMPI adsorption has come to equilibrium. Although the shape of the SHG adsorption curve versus time is similar for $I(2\omega)_{pp}$ and $I(2\omega)_{sp}$, their ratio $I(2\omega)_{pp}/I(2\omega)_{sp}$ changes considerably, as can be seen in Figure 2-4c: there is a gradual rise in $I(2\omega)_{pp}/I(2\omega)_{sp}$ with time. This seems to indicate that DAMPI slowly positions itself more perpendicularly towards the surface.

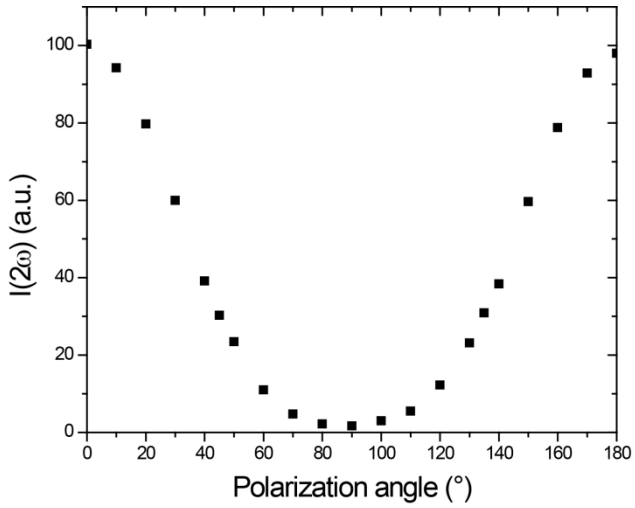

Figure 2-5: Variation of the *p*-polarized second-harmonic signal with the polarization angle of the incoming light. The incoming light is linearly polarized, and the plane of rotation is rotated along the direction of light propagation. A polarization angle of 0° corresponds to *p*-polarization, while a polarization angle of 90° corresponds to *s*-polarization.

In Figure 2-5, the *p*-polarized second-harmonic signal at equilibrium is depicted with respect to the polarization angle of the fundamental. The corresponding average tilt angle α was calculated to be 18.8°.[40] The experiment was repeated twice with other silicalite-1 films from different synthesis batches, resulting in an average tilt angle of 22.8° and 13.2° at equilibrium. In correspondence with the former experiment, the gradual rise of the ratio $I(2\omega)_{pp}/I(2\omega)_{sp}$ took place over the course of approximately 2 h. Moreover, the overall shape of $I(2\omega)_{pp}$ and $I(2\omega)_{sp}$ was similar. However, the temporal fluctuations differed randomly, thus indicating that these are caused by transient inhomogeneous distribution of DAMPI in the solution. In fact, in solvents with low

viscosity, such as chloroform, such fluctuations are nearly absent. Furthermore, the fluctuations can to some extent be smoothed out by improving the stirring regime in the cell. On the basis of the DAMPI molar absorptivity of 2.59 . 10^4 L mol^{-1} cm^{-1} at 400 nm in 1-hexanol, it can be estimated that about 5% of the generated SHG light is reabsorbed at equilibrium by the solution; however, this does not affect the orientational information gathered from the experiment.

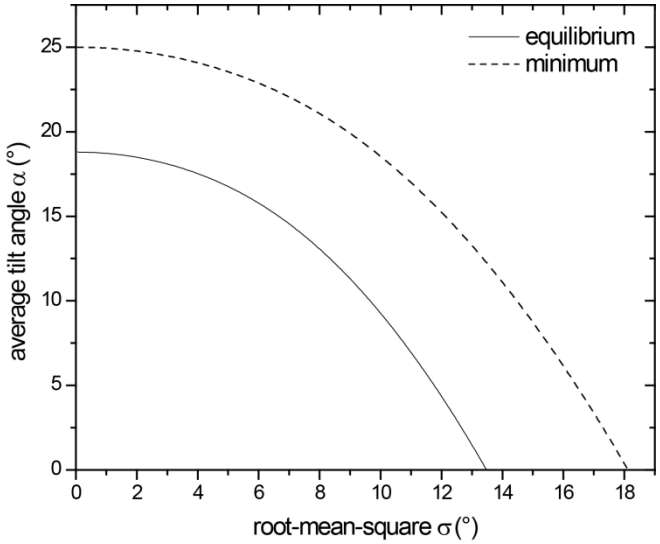

Figure 2-6: Plot of the continuum in which the average tilt angle α and the root-mean-square width σ is situated at equilibrium (solid line) and at the minimum of the $I(2\omega)_{pp}/I(2\omega)_{sp}$ curve (Figure 2-4c) (dashed line), assuming a Gaussian distribution.

A δ-distribution of the molecular orientation was assumed in the calculation of the average tilt angle α. When all adsorbed molecules are present in the straight pores of the b-oriented crystallites, a δ-distribution is expected, because the pores of a single crystallite all have exactly the same orientation[8] and the stilbazolium moiety is just able to fit into them.[35] However, when the molecules reside on the outer surface, a Gaussian distribution can be expected as a result of the greater extent of orientational freedom. The effect of a deviation from a δ-distribution was studied by Simpson and Rowlen,[41] assuming a Gaussian distribution. They analyzed the deviation of the real average orientation from the apparent tilt angle α with increasing orientational disorder in terms of the root-mean-square width σ. We can derive from their analysis that if the apparent average tilt angle of DAMPI is 18.8° then in fact the orientation and angular distribution of DAMPI is situated in the continuum between α = 18.8° with σ = 0°, and α = 0° with σ

= 13.5° (Figure 2-6). Because we find a very small tilt angle and narrow distribution, it is highly probable that at equilibrium most DAMPI molecules are positioned perpendicularly to the surface, and thus in the straight zeolite pores. That DAMPI effectively adsorbs in the pores of the zeolite is further supported by the observation that 2 h is needed to obtain equilibrium because diffusion of the large dye molecules in the narrow 10-membered rings of the MFI zeolite is expected to be slow. In addition, it has been shown that hemicyanine dyes adsorb in the straight pores of silicalite-1 from the liquid phase.[32,42,43] In the latter case, it has been shown that adsorption needs four hours to complete in methanol, which is similar to the time observed here for DAMPI adsorption.[42] Finally, in previous studies, for inclusion of a hemicyanine dye in the straight channels of a *b*-oriented silicalite-1 film, an apparent tilt angle of 11,3° instead of 0° was determined by fluorescence spectroscopy and an angle of 7.7° instead of 0° by SHG.[32,42]

The SEM picture in Figure 2-1 shows some overgrowth of *a*- or *c*-oriented zeolite crystallites, lying on their (100) or (001) face on the zeolite films. Because the straight pores of these crystallites are parallel to the plane of the film, DAMPI adsorption in these pores could explain a deviation from the average tilt angle from 0° and some orientational disorder. However, we observed no significant influence of the amount of overgrowth on the SHG signal. The sinusoidal pores are accessible at the exposed (100) faces at the discontinuities of the zeolite film and at the overgrown crystallites. DAMPI adsorption has also been studied on ZSM-5, which has the same framework type as silicalite-1, but contrary to silicalite-1, it contains some isomorphously substituted Al. These experiments have shown that DAMPI has a marked preference for the (010) faces as opposed to the (100) faces.[35] Hence, we do not attribute the orientational disorder to the latter faces.

The minimum of the $I(2\omega)_{pp}/I(2\omega)_{sp}$ curve in Figure 2-4c corresponds to an average tilt angle of 25.0°. If we compare this with the equilibrium state, we see that an 8° change of tilt angle corresponds to a 4-fold difference of $I(2\omega)_{pp}/I(2\omega)_{sp}$. Therefore, it can be concluded that second-harmonic generation, as a second-order technique, is extremely sensitive to orientational information. Furthermore, the apparent tilt angle of 25.0° at minimal $I(2\omega)_{pp}/I(2\omega)_{sp}$ corresponds to the continuum between α = 25.0° with σ = 0°,

and α = 0° with σ = 18.1° (Figure 2-6). This possibly higher degree of orientational disorder, half an hour after the addition of DAMPI, is in agreement with the conclusion that DAMPI is not yet fully adsorbed in the pores at this stage.

In conclusion, we have for the first time probed adsorption on a zeolite, *viz.* a *b*-oriented silicalite-1 film, with second-harmonic generation *in situ*. Moreover, because of the swift, continuous alternation between $I(2\omega)_{pp}$ and $I(2\omega)_{sp}$, changes in orientation of the adsorptive could be examined in real time. Surprisingly, the adsorption of DAMPI needed on average 2 h to complete, during which time DAMPI positions itself gradually more perpendicularly towards the surface. It seems therefore that DAMPI inches progressively into the straight pores of silicalite-1. This is in agreement with the study of Jentys et al.[9] in which it has been shown for several aromatic molecules that these molecules adsorb from the gas phase onto ZSM-5 by first physisorbing on the outer surface, followed by a slower diffusion into the pores. Because molecules in a physisorbed state on the outer surface may retain part of their rotational freedom, the larger tilt angle or larger degree of disorder, as derived from SHG, suggests a physisorbed state at the outer surface. Because Second-Harmonic Generation is uniquely suited to probe the orientation of organic molecules *in situ* at liquid/solid interfaces, we are currently expanding our approach to other model systems.

References

1 Stoye, D.; Funke, W.; Hoppe, L.; Hasselkus, J.; Curtis, L.G.; Hoehne, K.; Zech, H.-J.; Heiling, P.; Yamabe M.; et al.: "Paints and Coatings" In *Ullmann's Encyclopedia of Industrial Chemistry*, electronic release, 6th ed.; Wiley-VCH: Weinheim, 2000.

2 Mortcliff, S.; Hulpke, H.; Bannick, C.-G.; Terytze, K.; Knoop, G.; Auerswald, K.; Litz, N.; Mayer, R., Stoy; A.; Alef, K.; et.al.: "Soil" In *Ullmann's Encyclopedia of Industrial Chemistry*, electronic release, 6th ed.; Wiley-VCH: Weinheim, 2000.

3 Bono, A.; Mun, H.C.; Rajin, M. *Studies in Surface Science and Catalysis* **2006**, *159*, 693-696.

4 Heiland, H.-J.; Marser, H.; Schlüssler, H.-J.: "Cleansing Agents" In *Ullmann's Encyclopedia of Industrial Chemistry*, electronic release, 6th ed.; Wiley-VCH: Weinheim, 2000.

5 Vargas, A.; Ferri, D.; Bonalumi, M.; Mallot, I.; Baiker, A. *Ang. Chem. Int. Ed.* **2007**, *46*, 3905.

6 Rice, C.; Tang, Y.; Oldfield, E.; Wieckowski, A.; Hahn, F.; Gloaguen, F.; Léger, J.-M.; Lamy, C. *J. Phys. Chem. B* **2000**, *104*, 5803.

7 Sing, K.S.W.; Everett, D.H.; Haul, R.A.W.; Moscou, L.; Pierotti, R.A.; Rouqueral, J.; Siemieniewska, T. *Pure Appl. Chem.* **1985**, *57*, 603.

8 van Bekkum, H.; Flanigen, E.M.; Jacobs, P.A.; Jansen, J.C. *Introduction to Zeolite Science and Practice*, 2nd ed.; Elsevier: Amsterdam, 2001.

9 Jentys, A.; Tanaka, H.; Lercher, J.A. *J. Phys. Chem. B* **2005**, *109*, 2254.

10 Chmelik, C.; Varma, A.; Heinke, L.; Shah, D.B.; Kärger, J.; Kremer, F.; Wilczok, U.; Schmidt, W. *Chem. Mater.* **2007**, *19*, 6012.

11 Heinke, L.; Chmelik, C.; Kortunov, P.; Ruthven, D.M.; Shah, D. B.; Vasenkov, S.; Kärger, J. *Chem. Eng. Technol.* **2007**, *30*, 995.

12 Zhao, L.; Shen, B.; Gao, J.; Xu, C. *J. Catal.* **2008**, *258*, 228.

13 Eslava, S.; Baklanov, M.R.; Kirschhock, C.E.A.; Iacopi, F.; Aldea, S.; Maex, K.; Martens, J.A. *Langmuir* **2007**, *23*, 12811.

14 Okolo, B.; Park, C.; Keane, M.A. *J. Coll. Interface Sci.* **2000**, *226*, 308.

15 Yu, M.; Wyss, J.C.; Noble, R.D., Falconer, J.L. *Microporous and Mesoporous Materials* **2008**, *111*, 24.

16 Held, H.; Lvovsky, A.I.; Wei, X.; Shen, Y.R. *Phys. Rev. B* **2002**, *66*, 205110.

17 Williams, C.T.; Beattie, D.A. *Surf. Sci.* **2002**, *500*, 545.

18 Chen, C.K.; Heinz, T.F.; Ricard, D.; Shen, Y.R. *Chem. Phys. Lett.* **1981**, *83*, 455.

19 Guyot-Sionnest, P.; Superfine, R., Hunt, J.H., Shen, Y.R. *Chem. Phys. Lett.* **1988**, *144*, 1.

20 Corn, R.M.; Higgins, D.A. *Chem. Rev.*, **1994**, *94*, 107.

21 Bain, C.D. *J. Chem. Soc., Faraday Trans.* **1995**, *91*, 1281.

22 Vidal, F.; Tadjeddine, A. *Rep. Prog. Phys.* **2005**, *68*, 1095.

23 Dannenberger, O.; Buck, M.; Grunze, M. *J. Phys. Chem. B* **1999**, *103*, 2202.

24 Wang, H.; Troxler, T.; Yeh, A.-G. ;Dai, H.-L. *Langmuir* **2000**, *16*, 2475.

25 Grahn, M.; Lobanova, A.; Holmgren, A.; Hedlund, J. *J. Chem. Mater*. **2008**, *20*, 6270-6276.

26 van Koningsveld, H.; Tuinstra, F.; van Bekkum, H.; Jansen, J.C*. Acta Crystallogr., Sect. B* **1989**, *B45*, 423.

27 Fyfe, C.A.; Diaz, A.C.; Grondey, H.; Lewis, A.R.; Forster, H. *J. Am. Chem. Soc.* **2005**, *127*, 7543.

28 Wang, Z.; Yan, Y. *Chem. Mater.* **2001**, *13*, 1101.

29 Corn, R.M.; Higgins, D.A. *Chem. Rev.* **1994**, *94*, 107.

30 β^{zzz} is 510 ± 49 * 10^{-30} esu in 1-hexanol, measured at a fundamental wavelength of 800 nm.

31 Zhuang, X.; Miranda, P.B.; Kim, D.; Shen, Y.R. *Phys. Rev. B* **1999**, *59*, 12632.

32 Shim, T.K.; Kim, D.; Lee, M.H.; Rhee, B.K.; Cheong, H.M.; Kim, H.S.;Yoon, K.B. *J.Phys.Chem.B* **2006**, *110*, 16874.

33 Heinz, T.F.; Tom, H.W.K.; Shen, Y.R. *Phys. Rev. A* **1983**, *28*, 1883.

34 Shen, Y.R. *Nature* **1989**, *337*, 519.

35 Roeffaers, M.B.J.; Ameloot, R.; Baruah, M.; Uji-I, H.; Bulut, M.; De Cremer, G.; Müller, U.; Jacobs, P.A.; Hofkens, J.; Sels, B.F.; De Vos, D.E. *J. Am. Chem. Soc.* **2008**, *130*, 5763.

36 Calzaferri, G.; Li, H.; Brûhwiler, D. *Chem. Eur. J.* **2008**, *14*, 7442-7449.

37 Shen Y.R. *The Principles of Nonlinear Optics*, 1st ed.; Wiley: USA, 1984; chapter 25.

38 Kauranen, M.; Verbiest, T.; Maki, J.J.; Persoons, A. *J. Chem. Phys.* **1994**, *101*, 8193.

39 Note that in Fig. 4b and c, occasional gaps can be observed in the experimental data points. During these time periods, no data points where collected. However, these gaps do not influence the overall result.
40 Fresnel coefficients were calculated by presenting the interfacial system as a three-layer system, as in Zhuang et al.[31] The refractive index used was 1.416 for 1-hexanol and 1.451 for the zeolite-film filled with 1-hexanol. The latter was calculated by use of the Lorentz-Lorentz theory[44] by making use of the experimentally measured refractive index and pore volume of silicalite-1 films made by the same synthesis protocol as ours.[13] For the monolayer of DAMPI the same refractive index as the zeolite film was taken. The local-field factors can mathematically be included in the calculation of the Fresnel coefficient through the refractive index of the monolayer, as is done by Zhuang et al.[31] We have adopted the same protocol.
41 Simpson, G.J.; Rowlen, K.L. *J.Am. Chem. Soc.* **1999**, *121*, 2635.
42 Kim, H.S.; Lee, S.M.; Ha, K.; Jung, C.; Lee, Y.-J.; Chun, Y.S.; Kim, D.; Rhee, B.K.; Yoon, K.B. *J. Am. Chem. Soc.* **2004**, *126*, 673.
43 Kim, H.S.; Sohn, K.W.; Jeon, Y.; Min, H.; Kim, D.; Yoon, K.B. *Adv. Mater*. **2007**, *19*, 260.
44 Baklanov, M.R.; Mogilnikov, K.P.; Polovinkin, V.G.; Dultsev, F.N. *J. Vac. Sci. Technol. B* **2000**, *18*, 1385.

Chapter 3: The Use of Second-Harmonic Generation to Study Diffusion through Films under a Liquid Phase

Abstract

Knowledge of the diffusion of chemicals through buried films is important for a wide variety of systems – from sensing to drug delivery. Here, we show that second-harmonic generation (SHG) can be used to follow the diffusion through a thin film buried under a liquid *in situ*. More specifically, the diffusion of 4-(4-diethylaminostyryl)-1-methylpyridinium iodide through zeolite precursor films of different thickness is followed. The diffusion coefficients are calculated according to Fick's law.

This is the pre-peer reviewed version of the following article: M.A. van der Veen, M. De Roeck, I.F.J. Vankelecom, D.E. De Vos, T. Verbiest ChemPhysChem 2010, 11(4), 870-874.

3.1 Introduction

Thin films of inorganic or polymeric materials in contact with a liquid phase are of major importance in many applications, such as sensing, membrane separations and drug delivery, where the diffusion of liquids or solutes through these films can be either needed or unwanted. Therefore, it is crucial to have reliable techniques that enable an *in situ* follow-up of diffusion. Although a number of techniques are available to study diffusion through thin films in the gas phase, the choice is much more limited for diffusion through a thin film underneath a liquid phase.

A simple method to determine the diffusion coefficient is the gravimetric method. Although this technique is widely spread, it is often not suited to study diffusion in thin films, because for example, the density difference between liquid and thin film or the balance accuracy can be insufficient, and desorption effects can seriously influence the accuracy.[1,2] Another commonly used technique is attenuated total reflection Fourier transform infrared spectroscopy (ATR-FTIR) by which the one-sided diffusion of different compounds can be followed via the evanescent wave. The sample then needs to be deposited on top of a crystal and problems of adhesion can occur.[2,3,4] A technique with minimum sample preparation is terahertz (THz) time-domain reflectance spectroscopy.[5] This technique was recently used to follow the movement of an acetone front through a polymer via the reflectance on the interface between dry and wet polymer. No carrier was needed for the film, but it is not clear yet whether the technique can also be used to study diffusion through wet films and whether films deposited on particles can be studied. Furthermore, the spatial resolution of the position of the penetrant front is limited to tens of micrometers, making terahertz spectroscopy an interesting technique only for millimeter thick films. Another non-destructive technique for which the carrier of the film is not important is ellipsometry. In this case however, the sensitivity is critically dependent on the difference of refractive index between solvent and film. Furthermore, surface roughness can introduce artifacts that can seriously influence the results.[6]

In this paper, second-harmonic generation (SHG) is presented as a powerful method to study diffusion of small compounds through thin films. Since centrosymmetric media cannot generate a second-harmonic response, the liquid phase does not contribute to the overall signal. Moreover, only the interfacial regions are probed by this technique, making the method particularly suited for *in situ* studies of diffusion in complex systems. There are also no geometrical limitations. In contrast to most of the aforementioned techniques, the thin films do not need to be shaped as a flat sheet, since SHG can, for example, follow the adsorption of solutes on the surface of microparticles in suspension.[7] All these advantages of SHG have already been used to probe the diffusion of an aromatic compound across a biological membrane.[8,9] In this very specific application, it is in fact the decrease of the second-harmonic signal which is followed, since in this case diffusion gives rise to oppositely oriented molecules at the inner part of the bilayer in comparison with molecules only being present at the outer surface.

In the presented work, it is shown that SHG can be more generally used to probe the diffusion of solutes through thin films present under a liquid phase. The diffusion of a hemicyanine dye through zeolite precursor films of different thicknesses was followed and the diffusion coefficients were calculated.

3.2 Results and Discussion

As SHG is a second-order nonlinear optical process, it is forbidden in a medium with inversion symmetry. This arises from the fact that within the electric dipole approximation, SHG can be described by the second-order nonlinear polarisation $P^{(2)}(2\omega)$:[10]

$$P^{(2)}(2\omega) = \chi^{(2)} E(\omega) E(\omega) \qquad \text{Eq. 3-1}$$

with $\chi^{(2)}$ the second-order susceptibility and $E(\omega)$ the electric field of the incoming light at frequency ω. Since $\chi^{(2)}$ is a third-rank tensor, it is extremely sensitive to symmetry. For example, in centrosymmetric media, all elements of $\chi^{(2)}$ will be zero. This makes SHG an excellent technique to study surfaces where centrosymmetry is necessarily broken.

From Equation 3-1, it is clear that the second-harmonic intensity is directly proportional to the square of the amplitude of the nonlinear susceptibility. At an interface at which adsorbed molecules are present, the total nonlinear susceptibility $\chi_{tot}^{(2)}$ can be described by Equation 3-2:[11]

$$\chi_{tot}^{(2)} = \chi_{sub}^{(2)} + \chi_{int}^{(2)}(\theta(t)) + \chi_{ads}^{(2)}(\theta(t)) \qquad \text{Eq. 3-2}$$

This means that SHG can originate from the substrate ($\chi_{sub}^{(2)}$), the interaction between substrate and adsorbate ($\chi_{int}^{(2)}$), and the adsorbate ($\chi_{ads}^{(2)}$). Only $\chi_{int}^{(2)}$ and $\chi_{ads}^{(2)}$ are dependent on the adsorbate coverage $\theta(t)$. Due to this dependence, adsorption processes at interfaces can be probed.

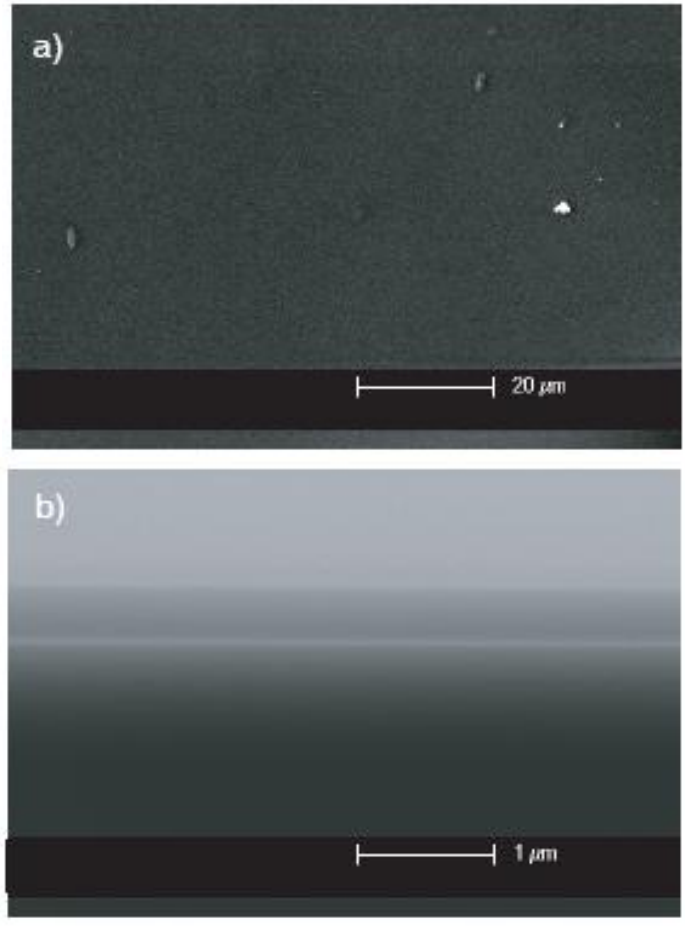

Figure 3-1: A SEM-picture of a) the surface and b) the cross-section of a PS-film.

The films used herein are formed from the precursors to silicalite-1 zeolites. Such zeolites can be formed from clear precursor solutions (PS) that contain TPAOH (tetra-*n*-

propylammonium hydroxide) and TEOS (tetraethyl orthosilicate).[12] Small, nanometer-sized zeolite nuclei are formed in such solutions, with the tetrapropylammonium cations acting as the template. The films were prepared by spin-coating the precursor solutions on the silicon wafers. The TPAOH was not removed by calcination. Because no high-temperature treatment was applied, no macro-pores and hardly any cracks could be observed in the samples via SEM and AFM measurements (Figure 3-1, Table 3-2).

The experimental layout to determine the diffusion coefficients is schematically depicted in Scheme 3-1. A PS-film is deposited on a Si wafer acting as a substrate, and brought in contact with a solvent. The adsorbate DAMPI (4-(4-diethylaminostyryl)-1-methylpyridinium iodide) is injected into the solvent in which, due to stirring, a homogeneous concentration is achieved nearly instantaneously. From this moment on, the adsorbate can diffuse into the film in a unilateral fashion.

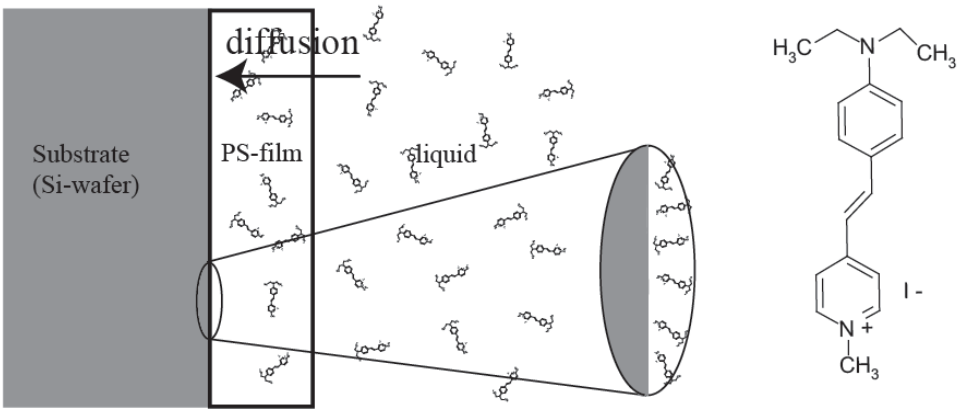

Scheme 3-1: Experimental lay-out (left); structure of DAMPI (right).

As centrosymmetry is expected in the bulk of the film, the latter will not generate any second-harmonic signal. However, the film has two interfaces which may contribute to the SHG-signal, namely, the film/liquid interface and the substrate/film interface. Hence, according to Equation 3-2, adsorption of DAMPI at either interface may give rise to a change in the SHG-signal.

The SHG signal, collected continuously after adding DAMPI to the liquid, is shown in Figure 3-2. The measurement was repeated for three films of different thickness, named PSI, PSII and PSIII in order of increasing film thickness, and for a bare Si wafer as

blank. As no SHG signal could be distinguished before adding DAMPI, except for a small signal for the blank, the substrate second-order susceptibility $\chi_{sub}^{(2)}$ is negligible for both interfaces. While the increase of the SHG-signal is completed almost immediately in case of the blank (Figure 3-2), it becomes much slower when a PS-film is present. Moreover, the thicker the film, the slower the rise in SHG signal. This already indicates that it is the substrate/film interface that is probed. Since the evolution of the SHG-signal is dependent on a resistance to mass transfer through the film, it is the diffusion process that gives rise to the slow change in SHG.

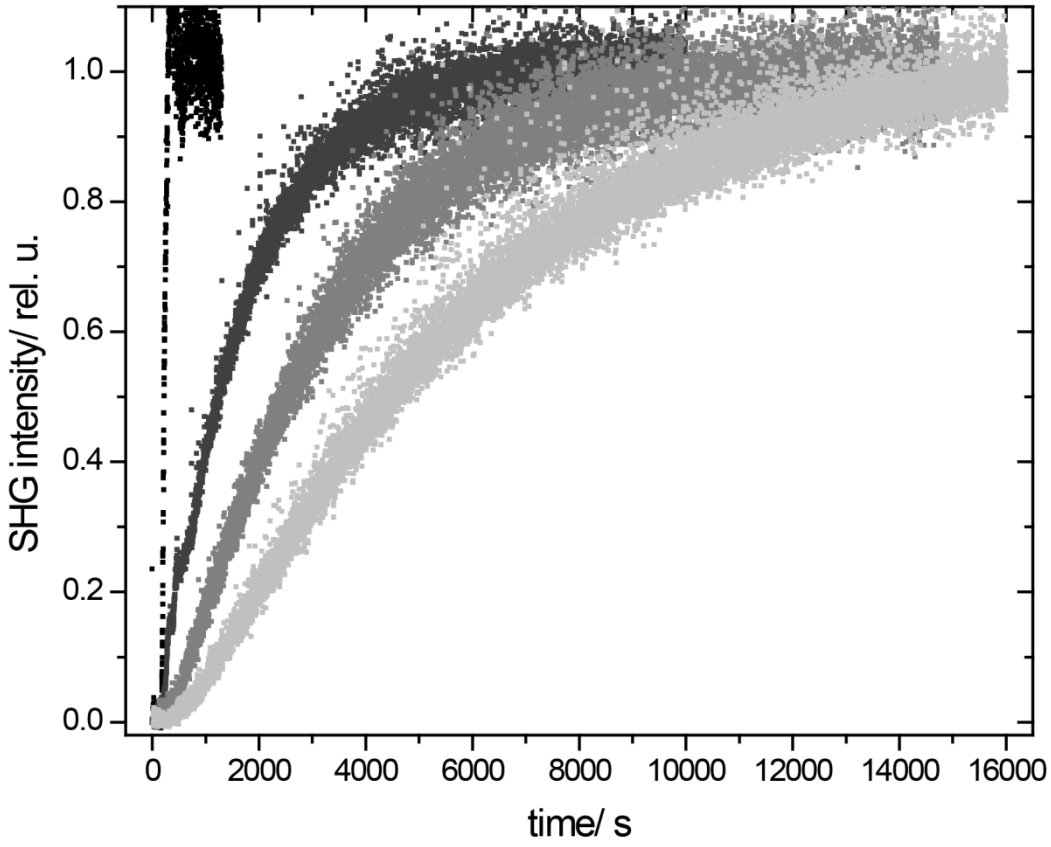

Figure 3-2: Evolution with time of the normalised *p*-polarised SHG-intensity of the samples with PS-film and the blank without a PS-film after addition of DAMPI to the liquid. The incoming light is *p*-polarised. (black = blank; dark grey = PSI; grey = PSII; light grey = PSIII).

Another strong indication that it is the substrate/film interface that is probed is given in Figure 3-3. The polarisation dependence at equilibrium was found to be exactly the same for all samples, including the blank. If adsorption occurred at the film/liquid interface, one would expect a difference in polarisation dependence between blank and films. Hence, it can be assumed that the molecules adsorbed at the substrate/film

interface are probed in our experiments. The absence of a contribution of the bulk of the film to the SHG signal is also confirmed by the fact that the absolute SHG intensity is not dependent on the film thickness (see Table 3-1). As can be seen, all the absolute values are of the same order of magnitude and the variations in signal intensity between samples are most likely due to small differences in alignment.

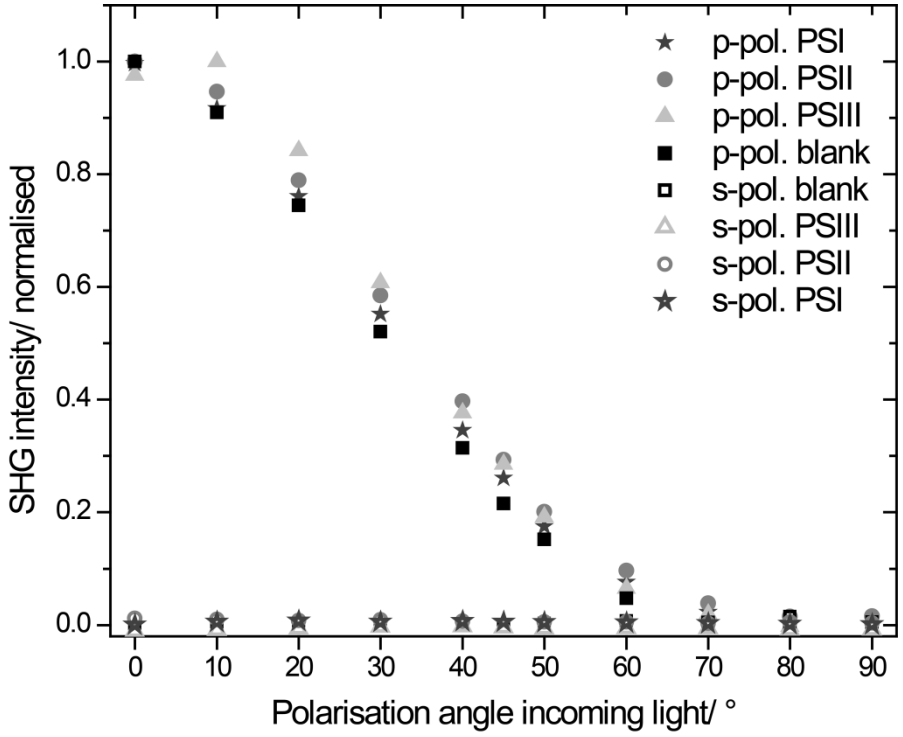

Figure 3-3: Variation of second-harmonic signal with the polarisation angle of the incoming light after addition of DAMPI to the solution and establishment of the equilibrium. Both the *p*-polarised and the *s*-polarised second-harmonic signals are shown for all three samples and the blank. The incoming light is linearly polarised, and the plane of rotation is rotated along the direction of light propagation. A polarisation angle of 0° corresponds to *p*-polarised incoming light, and a polarisation angle of 90° corresponds to *s*-polarised incoming light. For each sample the values are normalised with respect to their maximum value.

The increase of the SHG signal at the substrate/film interface can be attributed to the adsorbate nonlinear susceptibility $\chi_{ads}^{(2)}(\theta(t))$ or to the interaction nonlinear susceptibility $\chi_{int}^{(2)}(\theta(t))$. For the latter contribution, a strong interaction is necessary, such as the formation of a covalent bond between the adsorbate and a metal surface.[13,14] Such an interaction is not expected for adsorption of DAMPI at a Si or SiO_2 interface of a Si wafer. Hence, the change of SHG-signal can solely be attributed to the $\chi_{ads}^{(2)}$ term.

Table 3-1: Absolute values of the SHG-intensity after addition of DAMPI to the solution and establishment of the equilibrium. Both the detected second-harmonic light and the incoming light are *p*-polarised.

	PSI	PSII	PSIII	Blank
SHG [a.u.]	515	157	279	196

If the adsorbed molecules do not interact with each other, as is the case at low interfacial coverage, the nonlinear susceptibility $\chi^{(2)}_{ads}$ can be interpreted as a collective response from a summation over independent molecules. This means that $\chi^{(2)}_{ads}$ is linearly dependent on the surface concentration at the substrate surface $\theta(t)$ of the adsorbate molecule.[15, 16] Since the SHG intensity in aforementioned experiments depends only on $\chi^{(2)}_{ads}$, the intensity is quadratically dependent on the surface concentration $\theta(t)$

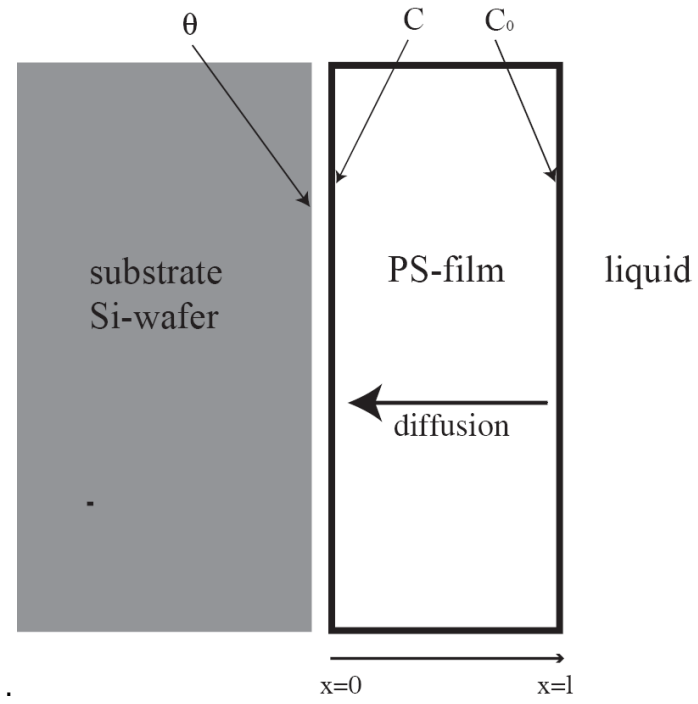

Scheme 3-2: Schematic depiction of the different concentration variables used in the calculation of the diffusion coefficient. θ is the surface concentration at the surface of the Si wafer, C is the concentration in the PS-film at x = 0, and C_0 is the concentration in the PS-film at x = l.

Hence, we can directly relate the SHG intensity to the amount of DAMPI adsorbed at the substrate/film interface. At low surface concentration, that is, in the lower portion of

the adsorption isotherm, the surface concentration θ (Scheme 3-2) is linearly related to the concentration C of the diffusing substance in the film at x = 0 (Scheme 3-2).

$$C(t) = K\theta(t) \qquad \text{Eq. 3-3}$$

As the measured surface concentration θ is directly related to concentration C which appears in the diffusion equation, the collected SHG intensities can be used to determine the diffusion coefficient. The most suitable theory to model diffusion is Fick's theory, which is based on a concentration gradient as the driving force. In the case of Fickian diffusion, the correct diffusion equation for the experimental lay-out depicted in Scheme 3-1 is given by Equation 3-4:[17]

$$C = C_0 \sum_{n=0}^{\infty} (-1)^n erfc \frac{(2n+1)l}{2\sqrt{Dt}} \qquad \text{Eq. 3-4}$$

Herein C is the concentration of the diffusing substance at x = 0 (see Scheme 3-2), D is the Fickian diffusion coefficient, l is the thickness of the plane sheet (see Scheme 3-2), and t is time. Equation 2-4 is the solution for a plane sheet of thickness *l* with following boundary conditions: 1) the concentration at the borderline in contact with the liquid is instantaneously established at a value C_0 at t = 0 (see Scheme 3-2); 2) this concentration remains constant over the full duration of the diffusion experiment, 3) there is no diffusion through the distant interface and 4) concentration of the diffusing adsorbate is initially zero throughout the sheet. The series in Equation 3-4 converges rapidly to Equation 2-5 for all but large values of Dt/l^2.

$$C = C_0 erfc \frac{l}{2\sqrt{Dt}} \qquad \text{Eq. 3-5}$$

In Figure 3-4, exemplary fits of the data to Equation 3-5 are shown. Only the first half of the graph, that is, till 35% of surface coverage, is used, because only at a relatively low occupation degree of the Si wafer by DAMPI, Equation 3-3 is expected to be valid. Moreover, the assumption that the adsorbate nonlinear susceptibility $\chi_{ads}^{(2)}$ is linearly dependent on the surface concentration is valid only at rather low interfacial concentration (*vide supra*).

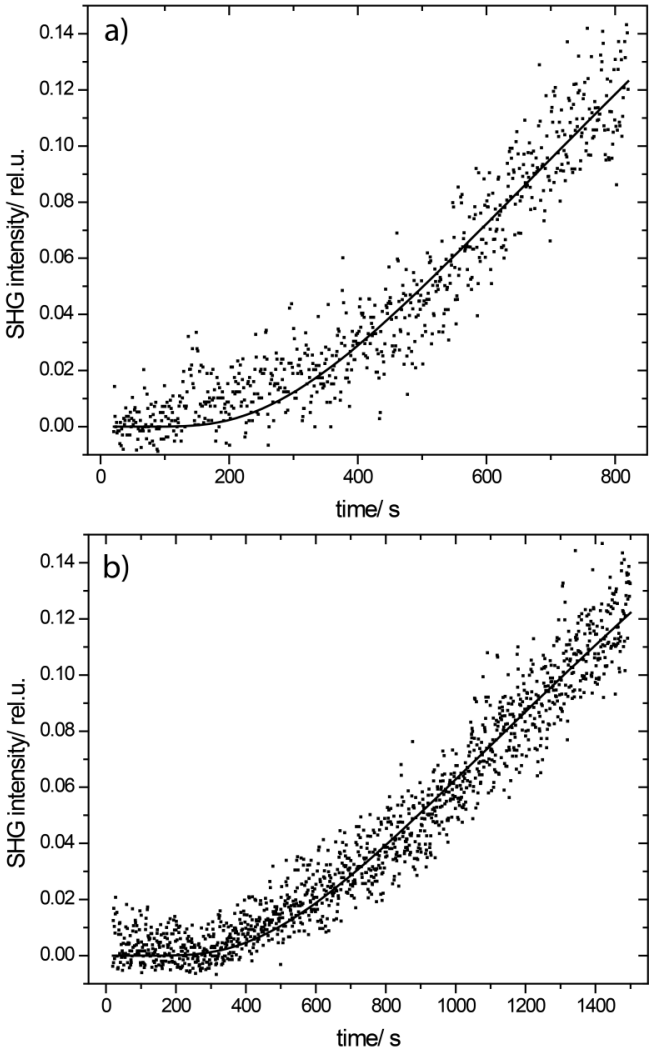

Figure 3-4: Evolution with time of the *p*-polarised SHG-intensity of the samples with a) the PSII film and b) the PSIII film, after addition of DAMPI to the solution. The incoming light is *p*-polarised. The fit to Equation 3-5 is shown.

All diffusion constants are of the same order of magnitude (see Table 3-2), but they seem to be dependent on the thickness of the sample. However, this is not unusual. Thickness-dependent diffusion constants are regularly reported and are generally attributed to a difference in density.[18,19] For the films studied herein, the PSII and PSIII films were prepared with respectively twice and four times the amount of material used for the PSI film. However, as can be seen from the thicknesses shown in Table 3-2, the thickness of the films increases more than linearly with the amount of material added. As a consequence, the thicker the film, the less dense the film. An increase in diffusivity with thickness is consistent with this. This is consistent with thickness-dependent diffusion coefficients reported in literature. These diffusion coefficients generally

increase with increasing film thickness.[18,19] Overall the fit is very good. As mentioned before, Equation 3-5 is only correct for small values of Dt/l^2; otherwise more terms would have to be introduced. For the highest value of Dt/l^2 used in the fitting process, the difference in the ratio C/C_0 between Equation 3-5 and Equation 3-4 with the additional terms is 1 %. It is thus justified to use the simplified Equation 3-5 in this case.

Table 3-2: Diffusion coefficients obtained by the fit to Equation 2-5 to the data, thickness via SEM data and roughness via AFM measurements of a 1 µm x 1 µm area.

	PSI	PSII	PSIII
D (cm^2/s)	$13*10^{-14}$	$39*10^{-14}$	$123*10^{-14}$
Thickness (nm)	100±7	250±27	573±27
R_{ms} (nm)	0.571	0.534	0.578

Furthermore, since the magnitudes of the diffusion constants are comparable with those of the diffusion constants of several organic molecules through standard polymers,[20,21] they are considered to be reasonable values. Hence, we may conclude that SHG can in principle be used as a method to study diffusion processes. Furthermore, the technique is limited neither by the material nor by the geometry of the support of the film. The timescale can vary from seconds to weeks; hence a broad interval of film thicknesses and diffusion constants are within the scope of this technique. In the measurements shown, only the substrate-film interface contributed to the SHG signal. As discussed, this is not necessarily the case; the film-solution interface can also contribute. However, it is possible to distinguish the signals of the two interfaces. First of all, adsorption at the film-solution interface will take place on a different, much faster, timescale, similar to that found for adsorption on the blank substrate. Secondly, only the adsorption on the substrate-film interface will be dependent upon thickness of the film. The strength of this technique lies in the fact that it can probe buried interfaces. In fact, an interface buried under both a liquid and a solid phase was probed herein. By extension, for series of layers of thin films, the arrival of the penetrant molecule can be probed at several of these interfaces. The only limitation lies in the fact that molecules that can generate SHG have to be noncentrosymmetric.

3.3 Conclusions

Second-harmonic generation has been succesfully employed to probe diffusion of a molecule from the liquid phase into a supported thin film. Using a simple Fickian diffusion equation, diffusion constants for a series of samples of different thickness were determined.

3.4 Experimental Section

Films were prepared on silicon wafers via following procedure. A silicon wafer (p-type, thickness 725 ± 25 µm; Siltronic AG) was treated with piranha acid (15mL H_2O_2 35% from Chemlab in 35mL 95%-97% sulfuric acid from Chemlab) for 30 min at 90°C, and rinsed intensively with milli-Q water. A solution of 30 mol % tetraethyl orthosilicate (TEOS, 98%, Acros) in 70 mol % tetra-*n*-propylammonium hydroxide (TPAOH, 40%, Alfa-Aesar) was stirred until the solution clarified ("clear solution"). The desired dilutions (1:9, 2:8, 4:6; volume ratio) were then prepared by means of ethanol (99%, VWR). These solutions were filtered through a 200nm PTFE filter, to remove possible dust, before spin-coating onto the carrier for 60 s at 1500 rpm. Afterwards, the samples were placed in a desiccator for 24h, followed by 24h in an oven at 45°C.

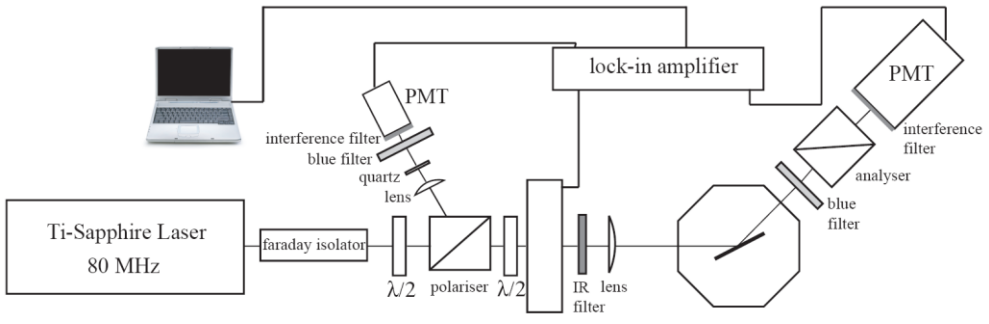

Scheme 3-3: The layout of the SHG system. $\lambda/2$: half-wave plate for 800 nm; IR filter: filter blocking 400 nm light; blue filter: filter blocking 800 nm light; PMT: photo-multiplier tube.

The obtained films were characterized by means of top and cross-section views via scanning electron microscopy (SEM, Philips XL 30 FEG). The surface was studied via atomic force microscopy using a multimode AFM with a Nanoscope IV controller (Veeco/Digital Instruments, Santa Barbara, USA). Samples were imaged in air in

tapping mode with a drive frequency of 200–300 kHz. Silicon nitride oxide-sharpened tips (NCHR, Nanosensors, Germany) were used.

The SHG experiments were performed with the set-up depicted in Scheme 3-3, using a Ti:Sapphire laser (Tsunami, Spectra-Physics) which produces ~100 fs pulses at 800 nm at a repetition rate of 80 MHz. The polarisation of the incoming beam is selected with a half-wave plate ($\lambda/2$). The fundamental light is then, with an incident angle of 67.5°, focused on the sample, which is placed vertically in a 10 ml octogonal cell (see Scheme 3-3). The path length for both the incoming and the second-harmonic light is 1.3 cm. The angle of 67.5° was chosen because at this angle, both the direction of the incoming and the second-harmonic light are perpendicular with respect to the windows. An analyser is used to select the polarisation of the SHG signal and filters are used to separate the SHG signal from the fundamental and background light. As detector a photomultiplier tube (XP2020, Philips) is employed with a lock-in amplifier (SR830, Stanford Research Systems) and chopper (~1 kHz, custom made) to reduce background noise on top of the signal. As a reference the SHG of a quartz crystal is continuously measured by a PMT; all data are corrected with the former. During the SHG experiments the cell was filled with 10 ml of 1-hexanol (Acros, 98%) and 1 ml of a 1 mM solution of DAMPI (4-(4-diethylaminostyryl)-1-methylpyridinium iodide; BioChemika, ≥97%) was injected to obtain a final DAMPI concentration of 10 µM. In each experiment we verified that the generated signal was not due to nonlinear scattering processes by performing angle-dependent measurements. Moreover, a signal was only observed when the focus of the fundamental laser beam coincided with the DAMPI layer, thus, it can be concluded that the signal does not originate from the solution through nonlinear scattering processes.

References

1 G.T. Fieldson, T.A. Barbari, *Polymer* **1993**, *34*, 1146-1153.
2 D. Vesely, Int. Mater. Rev. **2008**, *53*, 299-315.
3 Y.A. Elabd, M.G. Baschetti, T.A. Barbari, J. Polym. Sci., Part B: Polym. Phys. **2003**, *41*, 2794-2807.
4 V. Freger, A. Ben David, Anal. Chem. **2005**, *77*, 6019-6025.
5 J. Obradovic, J.H.P. Collins, O. Hirsch, M.D. Mantle, M.L. Johns, L.F. Gladden, Polymer **2007**, *48*, 3494-3503.
6 L.K. Filippov, J. Chem. Soc., Faraday Trans. **1993**, *89*, 4053-4057.
7 H.F. Wang, T. Troxler, A.G. Yeh, H.L. Dai, Langmuir **2000**, *16*, 245-2481.
8 A. Srivastava, K.B. Eisenthal, Chem. Phys. Lett. **1995**, *292*, 345-351.
9 A. Yamaguchi, M. Nakano, K. Nochi, T. Yamashita, K. Morita, N. Teramae, Anal. Bioanal. Chem. **2006**, *386*, 627-632.
10 C.T. Williams, D.A. Beattie, Surf. Sci. **2002**, *500*, 545-576.
11 R.M. Corn, D.A. Higgins, Chem. Rev. **1994**, *94*, 107-125.
12 A.M. Doyle, G. Rupprechter, N. Pfänder, R. Schlögl, C.E.A. Kirschhock, J.A. Martens, H.-J. Freund, Chem. Phys. Lett. **2003**, *382*, 404-409.
13 O. Dannenberger, M. Buck, M. Grunze, J. Phys. Chem. B **1999**, *103*, 2202-2213.
14 F. Eisert, A. Rosen, Phys. Rev. B **1996**, *54*, 14061-14065.
15 S. Haslam, S.G. Croucher, C.G. Hickman, J.G. Frey, Phys. Chem. Chem. Phys. **2000**, *2*, 3235-3245.
16 Y.R. Shen, Nature **1989**, *337*, 519-525.
17 J. Crank, The mathematics of diffusion (2nd Edition), Oxford University Press, 1979, pp. 11-27.
18 A.M. Shishatskii, Yu.L. Yampol'skii, K.-V. Peinemann, J. Membr. Sci. **1996**, *112*, 275-285.
19 T. Ponjanyakul, S. Puttipipatkahachorn, Int. J. Pharm. **2008**, *346*, 1-9.
20 T. Groves-Abe, F. Pschenitzka, H.Z. Jin, B. Bollman, J.C. Sturm, R.A. Register, J. Appl. Phys. **2004**, *96*, 7154-7163.
21 E. Van Keuren, W. Schrof, Macromolecules **2003**, *36*, 5002-5007.

Chapter 4: Localization of *para*-nitroaniline chains inside zeolite ZSM-5 with second-harmonic generation microscopy

Abstract

For the first time second-harmonic generation microscopy (SHGM) has been employed to study zeolites. Large ZSM-5 crystals filled with *para*-nitroaniline (PNA) dipoles have been visualized. It is shown that SHGM can discriminate between the straight *b*-pores and the sinusoidal *a*-pores of this zeolite, thus revealing the intergrown structure of these crystals. Moreover, it is shown that dipole chains are not only formed in the *b*-pores, but also in the *a*-pores. PNA only assembles into dipole chains of parallel orientation in those pores that are directly accessible from the outer surface. The area in which this PNA ordering prevails is limited to a strip near the outer surface of the zeolite crystal. A rationalization for these two observations is offered.

Second-harmonic generation microscopy (SHGM) has recently emerged as a powerful tool for high contrast study of cellular structures,[1] but has hardly been applied in materials science.[2] Here we report the first SHGM study of a zeolite, and elucidate the molecular organization of *para*-nitroaniline (PNA) in the pore system of zeolite ZSM-5 in relation to its SHG response.

SHG from PNA-filled zeolites can only be observed if there is a net noncentrosymmetric arrangement of PNA. For example, in the unidimensional pores of AlPO-5 (AFI topology), PNA forms strings that are organized in head-to-tail fashion.[3] PNA in ZSM-5 (MFI topology) also gives a strong SHG,[3b,4a] but solid-state NMR and X-ray diffraction investigations indicate that PNA is disordered inside the pore system,[4] which seems hard to reconcile with the SHG result. To this is added the structural complexity of ZSM-5 crystals with varying shape, aspect ratio and defect content. Better insight in ZSM-5 crystal structure has recently been achieved by combined use of fluorescence microscopy, AFM and EBSD (electron backscatter diffraction).[5] In rare cases, 'coffin-shaped' MFI crystals have a uniform crystallographic orientation all over the crystallite, even if various pyramidal and wedge-shaped components can be readily distinguished (Scheme 4-1a).[6] However, the crystal components below the (010) planes frequently undergo a 90° rotation around the c-axis (Scheme 4-1b). As will be shown, space-resolved observation of SHG is crucial for understanding the complex organization of PNA in ZSM-5.

First, coffin-shaped ZSM-5 crystals with a typical aspect ratio of 7 were selected (sample A, Si/Al = 700). Previous AFM characterization has shown that the step size of the terraces on (010), *viz.* ~ 20 nm, is distinctly larger than on (100), *viz.* < 5 nm.[7] Such difference in step heights on the crystal surfaces proves that the crystallographic axis orientation is identical all over the crystal (Scheme 4-1a), without the 90° degree intergrowth commonly observed for ZSM-5.[6] After loading the samples with PNA for 24 h at 110°C, thermogravimetric analysis revealed a PNA loading of 11 $\pm$ 1 wt. %, or 5.2 molecules per unit cell.

In our SHG microscope, we illuminate the sample with polarized light under normal incidence in transmission geometry. In such a configuration, dipolar chains of PNA

parallel with the propagation of light will not generate SHG, and only the dipole chains in the sample plane will be visualized. Second-harmonic generation can be described by the different components of the nonlinear polarization $P_i(2\omega)$ at frequency 2ω

$$P_i^{(2)} = \sum_{j,k} \chi_{ijk}^{(2)} E_j E_k \qquad \text{Eq. 4-1}$$

with $\chi_{ijk}^{(2)}$ a component of the second-order susceptibility tensor and E_{jk} the electric field component of the incoming light.

The number of independent susceptibility components is highly dependent on the symmetry of the system and the particular components that are addressed will depend on the experimental geometry. In our measurements, only 3 non-vanishing components are addressed: $\chi_{xxx}^{(2)}$, $\chi_{xyy}^{(2)}$ and $\chi_{yxy}^{(2)} = \chi_{yyx}^{(2)}$.[8] Furthermore the values of these components will be different depending on whether the molecules are arranged in a linear or a zigzag array, and this affects the dependence of the SHG light on the incident light polarization.

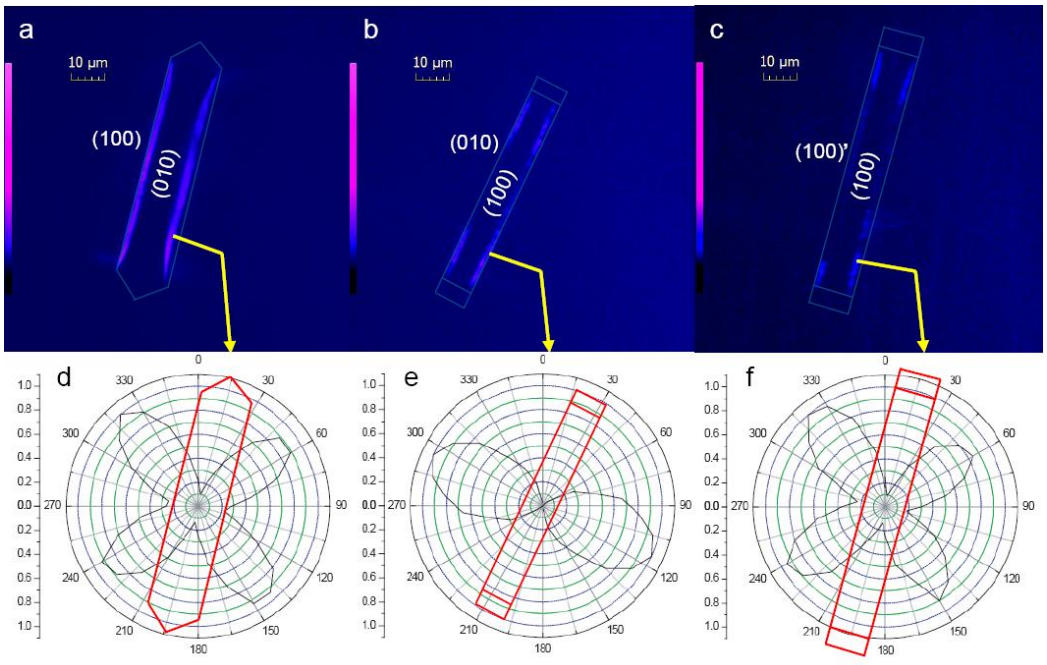

Figure 4-1: SHG images (a-c) and polarization patterns (d-f) for PNA-loaded ZSM-5: (a,d) crystal A1 from batch A, lying on (010); (b,e) crystal A2 from batch A, lying on (100); (c,f) crystal from batch B, lying on (100).

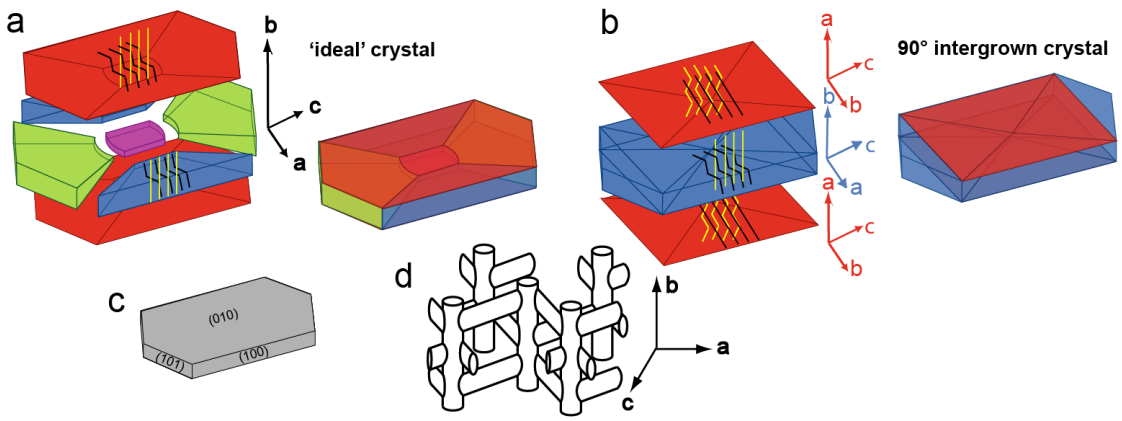

Scheme 4-1

Figure 4-1a and b show the SHG of two PNA-filled ZSM-5 crystals from sample A. They are positioned with their (010) face (crystal A1) and their (100) face (crystal A2) respectively in the *xy*-plane. SHG signals are only found in narrow rims at the crystal border, close to the (100) outer faces of the crystal (Figure 4-1a), or close to the (010) outer faces (Figure 4-1b). In the former case, these rims get narrower towards the crystal ends, suggesting that the pyramidal components of the crystal under the (100) faces (shown in blue in Scheme 4-1a) delimit the SHG-active zone. For the SHG-active areas, we recorded the dependence of SHG on the polarization angle of the linearly polarized input light (Figure 4-1d-e). The two strips along crystal A1 show everywhere a four lobe polarization pattern. By contrast, the SHG from the strips close to (010) of crystal A2 follows a 2-lobe polarization pattern, with maximum intensity along the *b*-axis of the crystal. Both polarization patterns are clearly different which indicates that the orientation of PNA is different in both cases. The 2-lobe pattern, in which the minimum intensity approaches zero, corresponds with straight dipole chains of PNA; the clearly distinct 4-lobe pattern can be modeled based on zigzag dipole chains of PNA (Appendix B). This orientation is consistent with the (010) surface faces giving access to the straight pores and (100) faces to the sinusoidal pores, at least in this particular ZSM-5 crystal with uniform axis orientation throughout the crystallite. It is also clear that oriented dipole chains are only formed in pores that are directly accessible from the outer surface; for instance, for crystal A1, no SHG signal generated by zigzag PNA

chains is detected in the middle of the (010) plane, where the sinusoidal pores run under and parallel to the surface (Appendix C and the red components in Scheme 4-1a). This agrees with the earlier hypothesis of 'surface selection': the zeolite prefers one end of PNA over the other as it enters the crystal.[3,4a]

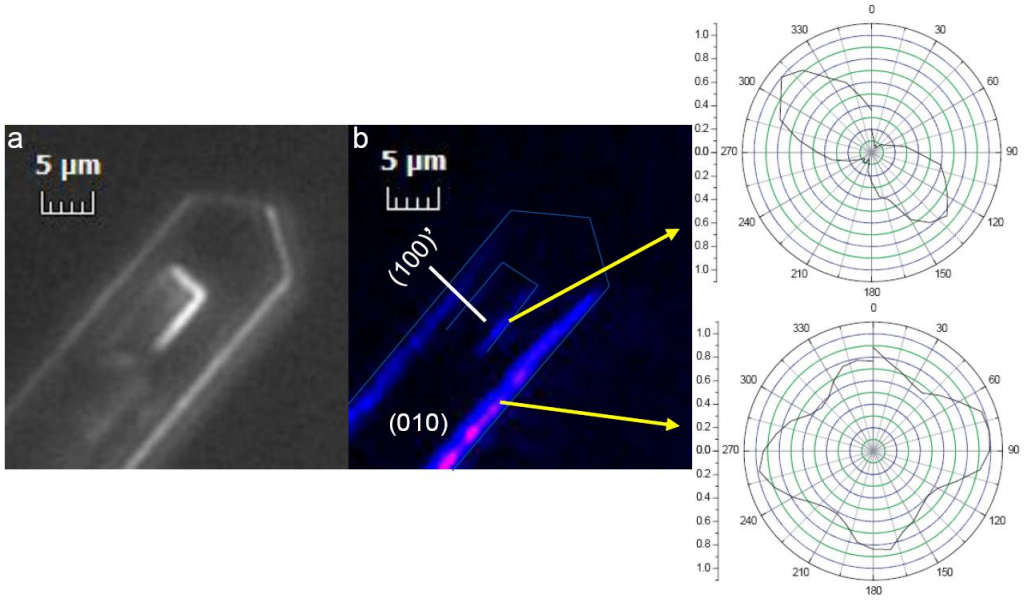

Figure 4-2: The small ramp on the (010) face of ZSM-5: (a) optical image, (b) SHG image and corresponding polarization patterns.

Figure 4-1c shows a crystal from a different batch B, positioned on its (100) face. In this batch, we previously found a large extent of 90° intergrowth covering the original (010) crystallographic faces.[5a,c,7] After PNA loading, SHG is again apparent near the (010) faces, but with a different polarization pattern (Figure 4-1f *vs.* 1d): the 4-lobe pattern of zigzag organized PNA now clearly indicates that a 90° axis rotation has occurred under the hexagonal crystal face, which therefore must be considered as a (100)' face. The latter gives access to sinusoidal pores. Even smaller defects can be visualized in detail. In Figure 4-2, a small ramp is seen protruding from the (010) face. Mapping of SHG polarization signatures reveals the 4-lobe signature of sinusoidal channels at the outer contours of the mother crystal, whereas the lateral faces of the ramp display the 2-lobe straight channel signature, which directly proves a 90° rotation.

In all ZSM-5 samples, SHG is only observed near the outer crystal surface. This is surprizing, since both TGA and the 2-photon fluorescence image of Figure 4-3a indicate

that PNA fills the pores to a large extent, and in a fairly homogeneous fashion. Apparently, only close to the outer surface the PNA molecules have a sufficient head-to-tail organization, not only with identical direction but also with the same sense. The bidirectional MFI pore system plays a crucial role here. As the PNA diffusion front moves into the ZSM-5 crystal, *e.g.* starting from (010) through the straight channel, there is an increasing chance that a PNA molecule jumps to a neighboring straight channel via a sinusoidal connecting channel (Scheme 4-1d). The electrostatic forces between PNA molecules in a string are rather weak, as they are proportional with $1/r^3$. Therefore a newly intruding PNA molecule could assume both the parallel and the antiparallel orientation, even if not necessarily with the same probability. In the latter case, the dipolar alignment is weakened, and this eventually leads to loss of the SHG signal. The more pronounced disorder of PNA organization in the crystal interior is in fact in perfect agreement with NMR and XRD data.[4] A disturbance of PNA organization is less likely close to the surface, since the higher degree of pore occupation with PNA during diffusion makes hopping of a PNA molecule to an adjacent channel less probable. This explains the SHG response at the crystal edges.

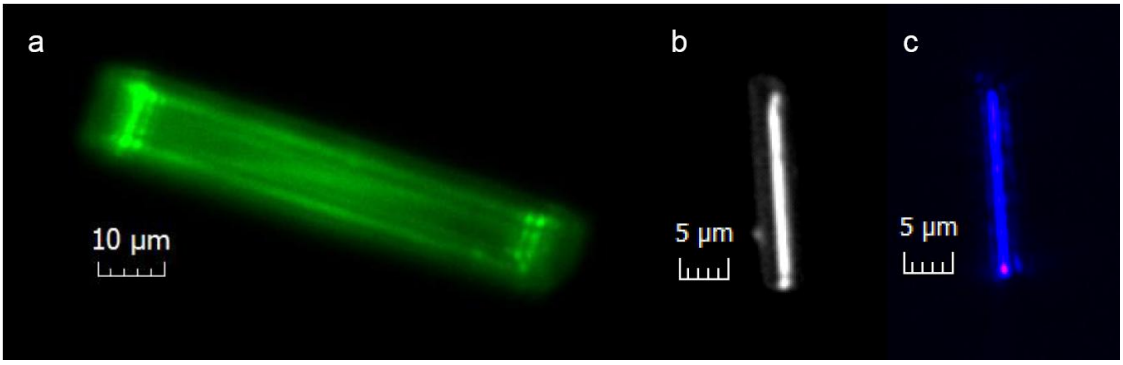

Figure 4-3: (a) 2-photon fluorescence image of a PNA-filled ZSM-5 crystal. (b-c) Optical and SHG images of PNA-filled SAPO-5 crystal.

If this hypothesis is correct, a one-dimensional SAPO-5 crystal, extensively filled with PNA, should have dipole chains and SHG over the full crystal length. This is convincingly borne out by Figure 4-3c. Thus, the unidimensional nature of the pores makes it much easier to keep the arrays of PNA organized. Note that the 12-MR pores of SAPO-5 are too narrow to allow a head-to-tail tumbling of PNA. These results are in accordance with those of Herance et al., who showed that the SHG efficiency of PNA-

loaded zeolites is significantly higher for one-dimensional pore architectures than for two-dimensional pore systems.[9]

Summarizing, SHG-microscopy is a powerful tool for revealing structural details of zeolites, and allows the molecular organization of *p*-nitroaniline (PNA) in complex ZSM-5 crystals to be related to their SHG response.

Note: Appendix A gives further information on the crystal batches and the number of crystals studied.

References

1 Mertz, J. *Curr. Opin. Neurobiol.* **2005**, *14*, 610.

2 (a) Zavelani-Rossi, M.; Celebrano, M.; Biagioni, P.; Polli, D.; Finazzi, M.; Duo, L.; Cerullo, G.; Labardi, M.; Allegrini, M.; Grand, J.; Adam, P.-M. *Appl. Phys. Lett.* **2008**, *92*, 093119/1. (b) Chen, I.-H., Chu, S.-W., Bresson, F., Tien, M.-C., Shi, J.-W.; Sun, C.-K. *Opt. Lett.* **2003**, *28*, 1338.

3 (a) Caro, J.; Finger, G.; Kornatowski, J.; Richter-Mendau, J., Werner, L., Zibrowius, B. *Adv. Mater.* **1992**, *4*, 273. (b) Werner, J.; Caro, J.; Finger, G.; Kornatowski, J. *Zeolites* **1992**, *2*, 658. (c) Marlow, F.; Wübbenhorst, M.; Caro, J. *J. Phys. Chem.* **1994**, *98*, 12315. (d) Klap, G.J.; van Klooster, S.M.; Wübbenhorst, M.; Jansen, J.C.; van Bekkum, H., van Turnhout, *J. Phys. Chem. B* **1998**, *102*, 9518. (e) Klap, G.J.; Wübbenhorst, M., Jansen, J.C.; van Koningsveld, H.; van Bekkum, H.; van Turnhout, J. *Chem. Mater*. **1999**, *11*, 3497.

4 (a) Reck, G.; Marlow, F.; Kornatowski, J.; Hill, W.; Caro, J. *J. Phys. Chem.* **1996**, *100*, 1698. (b) van Koningsveld, H.; Koegler, J.H. *Microporous Mater.* **1997**, *9*, 71. (c) Mentzen, B.F.; Lefèbvre, F. *J. Chim. Phys.* **1998**, *95*, 1052. (d) Fyfe, C.A.; Brouwer, D.H. *Microprous Mesoporous Mater.* **2000**, *39*, 291.

5 (a) Roeffaers, M.B.J.; Ameloot, R.; Baruah, M.; Uji-i, H.; Bulut, M.; De Cremer, G.; Müller, U.; Jacobs, P.A.; Hofkens, J.; Sels, B.F.; De Vos, D.E. *J. Am. Chem. Soc.* **2008**, *130*, 5763. (b) Karwacki, L.; Kox, M.H.F.; de Winter, D.A.M.; Drury, M.R.; Meeldijk, J.D.; Stavitski, E.; Schmidt, W.; Mertens, M.; Cubillas, P.; John, N.; Chan, A.; Kahn, N.; Bare, S.R.; Anderson, M.; Kornatowski, J.; Weckhuysen, B.M. *Nature Mater.* **2009**, *8*, 959. (c) Roeffaers, M.B.J.; Ameloot, R.; Bons, A.J.; Mortier, W.; De Cremer, G. J.; de Kloe, R.; Hofkens, J.; De Vos, D.E.; Sels, B.F. *J. Am. Chem. Soc.* **2008**, *130*, 13516.

6 Agger, J.R.; Hanif, N.; Cundy, C.S.; Wade, A.P.; Dennison, S.; Rawlinson, P.A.; Anderson, M.W. *J. Am. Chem. Soc.* **2002**, *125*, 830.

7 Roeffaers, M.B.J.; Sels, B.F.; Uji-i, H.; Blanpain B.; L'hoëst, P.; Jacobs, P.A.; De Schryver, F.C.; Hofkens, J.; De Vos, D.E. *Ang. Chem. Int. Ed.* **2007**, *46*, 1706.

8 Verbiest, T.; Clays, K.; Rodriguez, V. *Second-order nonlinear optical characterization techniques, an introduction*; CRC Press: Boca Raton, 2009.

9 Herance, J. P.; Das, D.; Marquet, J.; Bourdelande, J. L.; Garcı´a, H. *Chem. Phys. Lett.* **2004**, *395*, 186.

Chapter 5: Mapping of the organization of *p*-nitroaniline in SAPO-5 by second-harmonic generation microscopy

Abstract

Second-harmonic generation microscopy (SHGM) has been employed to study crystals of zeolite-like material SAPO-5 filled with *p*-nitroaniline (PNA). The SHG and 2-photon fluorescence response of PNA in the one-dimensional channels readily reveals the pore accessibility; intergrown crystallites containing hexagonal pyramidal components and internal diffusion barriers are found next to seemingly perfect crystals. The sensitivity of second-harmonic generation to molecular orientation allowed for mapping of the domains of differently organized PNA. Dense domains of highly aligned PNA alternate with dilute zones with loosely aligned PNA.

This chapter has been submitted to Physical Chemistry Chemical Physics by M.A. van der Veen, J. Van Noyen, B.F. Sels, P.A. Jacobs, T. Verbiest, D.E. De Vos.

5.1 Introduction

Ordering of organic molecules in the channels and cages of zeolites has received considerable attention for the generation of special optical properties. Such materials might be used for optical data storage,[1] for frequency conversion,[2] or as lasers.[3] One host/guest system that has been studied extensively is *p*-nitroaniline (PNA) entrapped in the zeolite-like material AlPO-5. The PNA/AlPO-5 system gives rise to second-harmonic generation[4] and pyroelectricity,[5] due to the non-centrosymmetric head-to-tail arrangement of the PNA molecules inside the AlPO-5 pores. It is well established that this is due to a surface selection process: when the molecules adsorb initially into the pores, they do so predominantly with the nitro-group first.[5c] The application of polarized light in Raman spectroscopy,[6] infrared spectroscopy,[7] UV-Vis spectroscopy[8] and second-harmonic generation[4b,c] studies has shown that the PNA molecules are aligned in the AlPO-5 pores. Based on Raman and infrared data, it has also been proposed that PNA can exist inside AlPO-5 in two distinct arrangements: one contains chains of hydrogen-bonded PNA molecules, while in the other the PNA molecules interact only weakly. However, it has not been verified experimentally whether these different arrangements give rise to true phase separation, and if so, which dimensions the domains of these phases possess. In order to visualize PNA domains in the channels of microporous solids, a technique is needed with both sufficient spatial resolution and with high sensitivity to molecular organization. In this paper, we use second-harmonic generation microscopy (SHGM) for this purpose. SHGM has so far only sporadically been used in materials science, and to our knowledge, no reports have appeared on use of SHGM for studying porous materials like zeolites. Our SHGM observations of PNA in the pores of the molecular sieve SAPO-5 show that dense phases of highly aligned PNA alternate with phases of more loosely interacting PNA. The phase domains extend over > 1 μm in all crystallographic directions. Combined SHG and 2-photon fluorescence microscopic observation of the SAPO-5 crystals also visualizes their internal structure.

5.2 Results and Discussion

The molecular sieves AlPO-5 and SAPO-5 both belong to the same AFI structure type. An important feature of this structure are the straight one-dimensional pores with 7.3 Å free pore diameter. The main difference between AlPO-5 and SAPO-5 is their slightly different chemical composition: AlPO-5 is an aluminophosphate material in which the aluminium atoms strictly alternate with the phosphorus atoms between the oxygen atoms (Al-O-P). In the used SAPO-5 sample, 1% of the P^{5+} has been substituted by Si^{4+}. The thus created charge deficiency is compensated by protons. However, the acid strength of these protons is relatively weak, as is the basicity of PNA; thus, protonation of PNA by the charge compensating protons is not expected. This is evidenced by the FTIR spectrum of the PNA-loaded SAPO-5, which is not substantially different from that of PNA in AlPO-5 (see Appendix F).

The X-ray diffractogram of the evacuated SAPO-5 sample (see Appendix D) confirms the crystallinity of the sample and corresponds to the expected powder pattern. From the SEM-micrograph (Figure 5-1), it is evident that the crystals are of excellent quality and have a hexagonal shape. This means that the crystallographic *c*-axis, which is a 6-fold axis of symmetry and corresponds with the pore direction, coincides with the long axis of the crystals (Scheme 5-1). Most crystals are between 10 and 55 µm long.

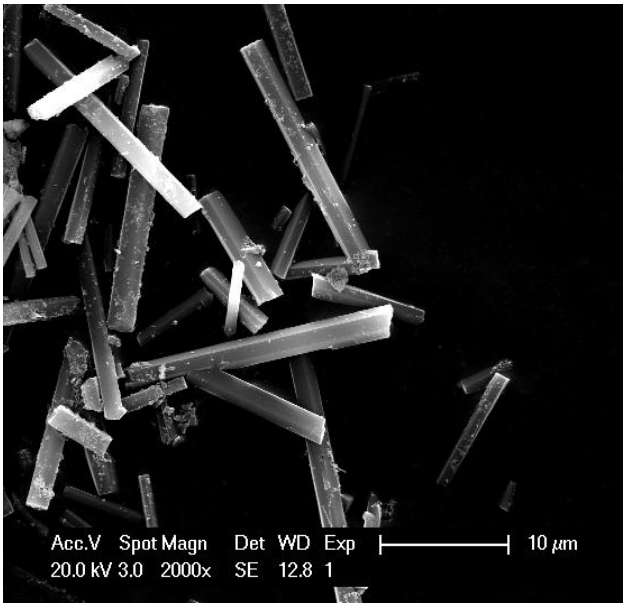

Figure 5-1: SEM micrograph of the SAPO-5 crystals.

Thermogravimetric analysis showed a weight loss of 9 wt% between 150°C and 200°C for the PNA-loaded samples. This was attributed to the loss of PNA and corresponds well with reported values for AFI-type zeolites loaded with PNA in a similar way.[4c,5a,6,7]

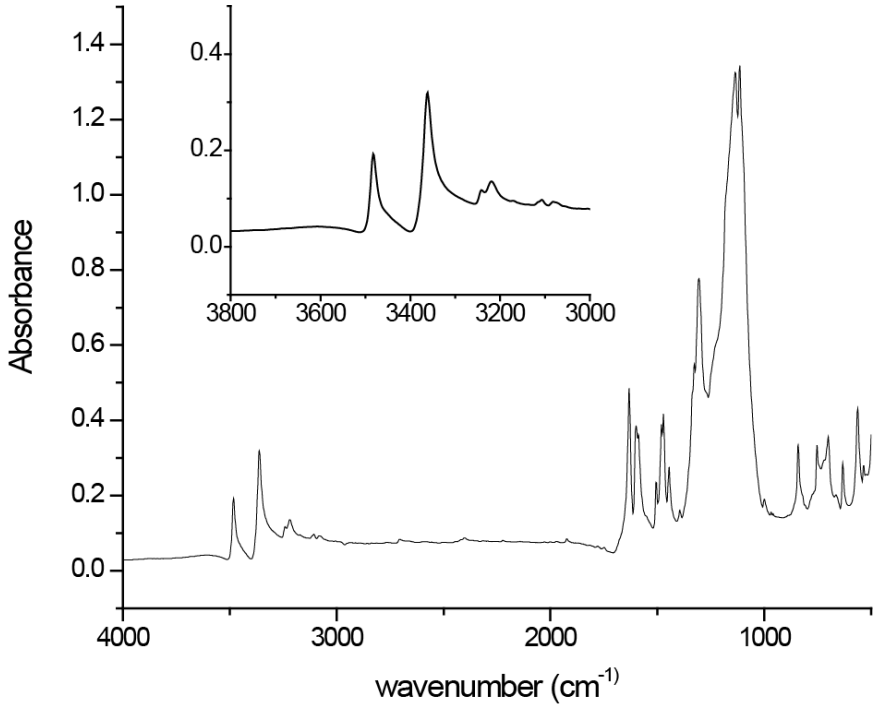

Figure 5-2: FTIR-spectrum of PNA-loaded SAPO-5. Inset: the NH-stretching region.

To investigate possible hydrogen bonding between the PNA molecules, infrared spectroscopy was applied (Figure 5-2). Of particular interest is the region from 3000 and 3500 cm^{-1}, the N-H stretching region. Four absorption peaks can be distinguished in this region. In accordance with Marlow et al.[7] and Kinski et al.,[9] the band at 3483 cm^{-1} is assigned to the asymmetric NH-stretching vibration, while the band at 3359 cm^{-1} represents the symmetric NH-stretching vibration. The weaker bands at 3215 and 3235 cm^{-1} can be assigned to H-bonded species. Due to the high correspondence of the positions of these four peaks to PNA present in hydrogen bonded form (see Appendix F) and the significant intensity of the peaks at 3215 and 3235 cm^{-1}, we can conclude that at least a certain amount of the PNA incorporated in SAPO-5 must be hydrogen-bonded. However, for fully H-bonded PNA, like in solid PNA, the band at 3483 cm^{-1} is at least as intense as or even more intense than the band at 3359 cm^{-1}. For non-hydrogen-bonded PNA, *e.g.* PNA dissolved in chloroform, the band at 3359 cm^{-1} gains more intensity.[7] This point is more elaborated on in Appendix F. Since in our spectrum

the 3483 cm^{-1} peak is clearly much weaker than the 3359 cm^{-1} peak, it is reasonable to conclude that only part of the PNA present is linked by hydrogen bonds. So PNA seems to be present in two different arrangements, one with and one without mutual H-bridges.

Next we used SHG-microscopy and two-photon fluorescence microscopy (TPFM) to study the loaded SAPO-5 samples. As SHG is a second-order process, it is only allowed in noncentrosymmetric ensembles. SHG from these materials must thus be attributed to head-to-tail chains of PNA-molecules in a dipolar arrangement. Two-photon fluorescence on the other hand is an odd-order process, and more specifically a third-order process, which removes the asymmetry requirement. TPFM can therefore be used to simply establish the presence of PNA. Note that in control experiments, the SAPO-5 crystal itself did not give rise to SHG or two-photon fluorescence.

Interestingly, when looking at the images of individual PNA-loaded crystallites, two clearly distinct image types were discerned, both in SHGM and TPFM. The images either show a bipyramidally shaped filling pattern as in Figure 5-3a, or display an elongated rectangular shaped filling pattern as in Figure 5-3b. Approximately 75% of the crystals investigated showed the rectangular shape, suggesting a uniform internal structure of the crystallites, with bundles of continuous, parallel channels running from one hexagonal facet to the opposite one. In contrast, the approximately bipyramidal shape, in which the two pyramids share their vertex, is consistent with an hourglass or dumbbell shape, which has previously been observed in SAPO-5 and some of its analogues with polarized optical microscopy,[10] with fluorescence microscopy[11] and in diffusion patterns measured by interference microscopy.[10,12] This feature was attributed to the growth mechanism of the SAPO-5 material,[5c] which results in the formation of various components within an individual crystallite.[11] Girnus et al.[13] observed either the dumbbell shape or the single crystals with continuous pores depending on the synthesis conditions. As shown in Scheme 5-1, the hexagonal crystal facets in fact are the base planes of two hexagonal pyramids, while the lateral facets belong to a different set of 6 crystallite components. The boundaries between the hexagonal pyramids and the other crystal components are usually considered as diffusion barriers.[10,11,14] That PNA chains are only found inside the hexagonal pyramidal segments supports this vision, as pores are only accessible from the hexagonal crystal facets. Clearly, in comparison with other

tools like interference microscopy,[10,12] SHGM is a very direct technique to visualize the internal structure and the access of small molecules like PNA to the pores.

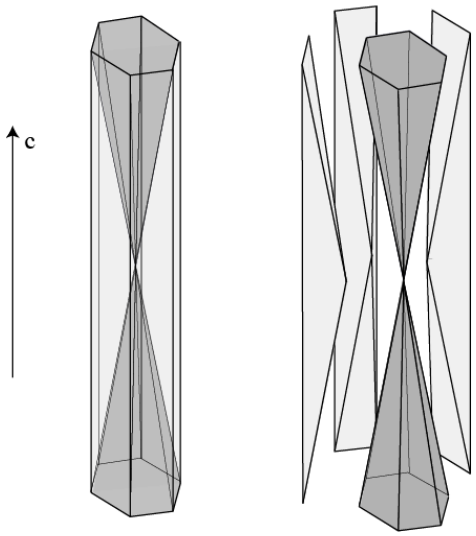

Scheme 5-1: Representation of the intergrowth structure of SAPO-5 (left). On the right side the bipyramidal core is shown together with three of the lateral facets.

A striking feature in some of the crystals with a rectangular SHGM pattern is that no SHG is generated in a small area close to the centre of the crystal (Figure 5-3d), while the two-photon fluorescence picture clearly shows that PNA is present in this area. This phenomenon can be rationalized based on the PNA organization as follows. Since the net-dipole moment of PNA is formed by a surface selection process in which PNA predominantly enters the pores with its nitro-group first, the net-dipole moment has a different orientation in the two halves of the crystal.[5a,c] This should lead to a polarization reversal in the middle of the PNA-filled AFI crystal, which has indeed been experimentally confirmed in the pyroelectric studies. At the front where the PNA-molecules with different sense meet, there is no net dipole moment and thus no SHG is generated there. Such a cancellation of SHG intensity in the middle of the crystal was observed for about half of these crystals; for the other crystals there is no such decrease in SHG-intensity (Figure 5-3b). Presumably, this can be attributed to an imperfect cancellation of the dipolar arrangement of PNA chains in each side of the crystal. Indeed, if the ordering of PNA in both meeting fronts is not exactly the same, the destructive interference will not be as pronounced or even be absent. In case the

SAPO-5 crystal contains pyramidal components, no real front between oppositely oriented PNA molecules can be formed.

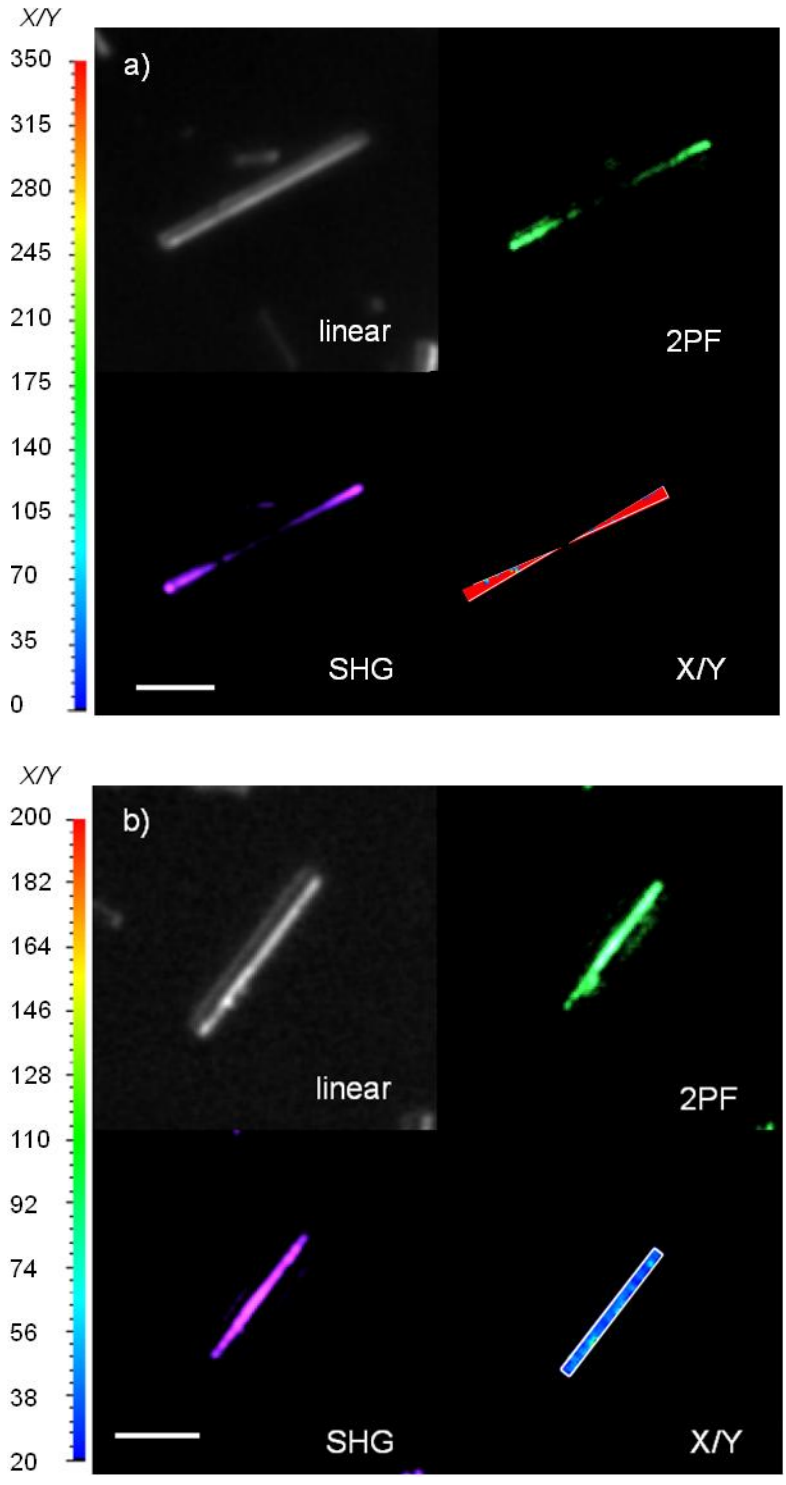

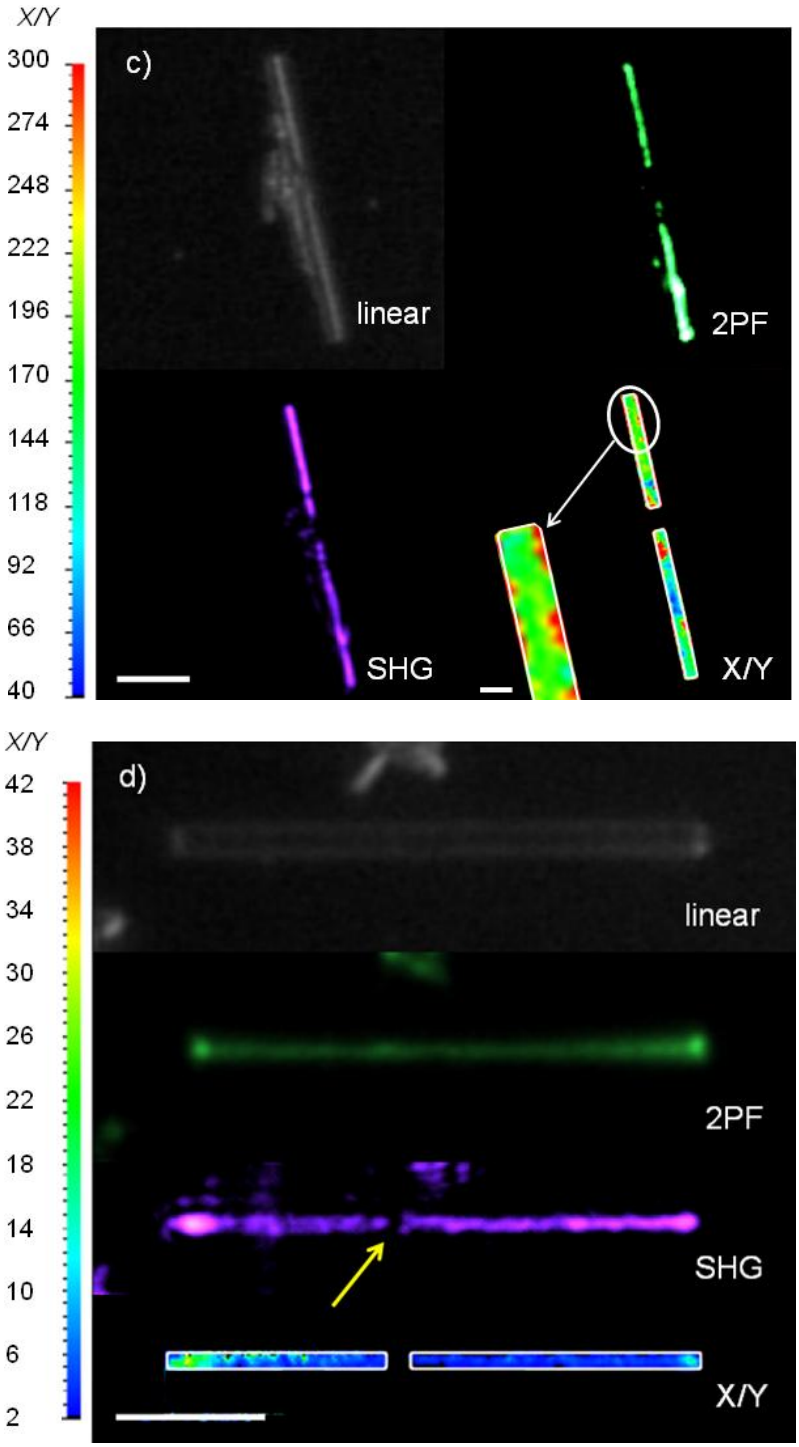

Figure 5-3: SHG and 2PF mapping of four PNA-loaded SAPO-5 crystals (a-d). For each crystal a linear optical image (grey, linear), a two-photon fluorescence image (green, 2PF), a second-harmonic generation image (purple, SHG) and the image of the X/Y ratio (false colour plot, X/Y) are shown. The colour bar corresponds to the X/Y ratio. The white bar represents 10 µm, except for the inset in the X/Y ratio in set c), where it represents 1 µm. Note that in the X/Y ratio images, only the region is shown in which the SHG-intensity is sufficient for a meaningful determination of X/Y. In Figure 3c, the black zone in the centre of the crystal corresponds to an imperfection in the crystal, to which the PNA has no access. In Figure 3d the yellow arrow points to the zone where no SHG is generated due to polarization reversal. In the X/Y ratio image in set a) and set c) all values higher than resp. 350 and 300 are also represented by the red colour.

Changes in alignment of the PNA inside the crystals can be probed by carefully selecting the input polarization in the SHG-microscope. For example, comparison of SHG-microscopy images taken with x- and y-polarized light, in which the x-direction coincides with the long crystal axis *c*, will yield a direct indication on the degree of alignment of PNA inside the crystals. The ratio of both images, X/Y, gives a mapping of all different orientations of PNA and may as such give an indication for the existence of different domains inside the crystal (see Appendix E). If we assume that PNA has only one molecular hyperpolarizability component along its long molecular axis z', then the X/Y ratio is a direct measure for its tilt angle (defined as the angle between the molecular axis and the direction of the pores). The higher this ratio, the smaller the tilt angle, thus the more aligned the molecules are. In general however, and certainly near resonance, PNA has two additional hyperpolarizability components. However, these are at least 5 to 10 times smaller than the main hyperpolarizability component along the z'-axis.[15] Taking the ratio X/Y as a measure for the tilt angle is therefore a very reasonable assumption. However, even in the general case, a change in X/Y will still indicate a change in overall orientation of PNA. Note that in principle, changes in the ratio X/Y can also be due to local changes in the hyperpolarizability of PNA. This could for example be due to local changes in environment or H-bonding. However, such changes in hyperpolarizability are usually very small and are therefore expected to be of minor importance.

Within one batch of PNA-loaded SAPO-5, we visualized the X/Y ratio for twenty crystals. In general, two extreme cases and a range of intermediate situations can be discerned. A first case is represented by the crystal of Figure 5-3a, with an X/Y ratio of 300 or more in all SHG-responsive zones of the crystal. In this case, the dependence of the SHG-intensity on the orientation of the plane of polarization of the incident light can be perfectly fitted by $\cos^4\alpha$ (Figure 5-4a; α is the angle between the polarization plane of the incident light and the *c*-axis of the crystal). Under the reasonable assumption that PNA has only one hyperpolarizability component (*vide supra*), it must be concluded that PNA is strongly aligned inside the pores with a very small tilt angle throughout the SHG-responsive zones of the crystal (see Appendix E). Based on polarized Raman observations, it has been proposed in the literature that hydrogen-bonded PNA is

strongly aligned with the pore direction, with a very modest tilt angle smaller than 9°.[6a] We can therefore assign these areas with X/Y > 300 to the hydrogen-bonded, densely packed arrangement of PNA.

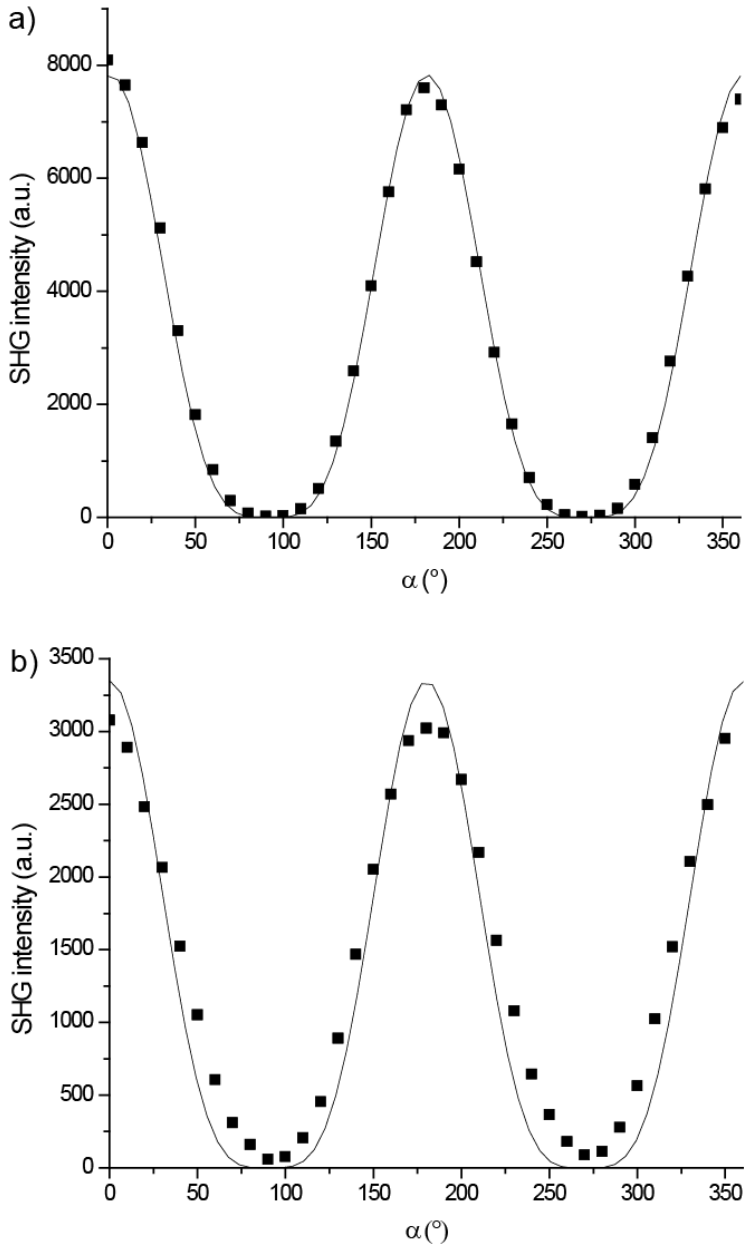

Figure 5-4: Variation of the SHG-intensity with the polarization angle α of the input light for a) an X/Y value of 400, b) an X/Y value of 60. The incoming light is linearly polarized and the plane of rotation is rotated along the direction of light propagation. A polarization angle of 0° corresponds to a polarization plane along the direction of the long crystal axis *c* of the PNA loaded SAPO-5 crystal, while a polarization angle of 90° corresponds to a polarization plane perpendicular to the long crystal axis *c*.

Secondly, crystals are observed with a much lower X/Y ratio over almost the entire crystal (Figure 5-3b). X/Y ratios are typically equal to or smaller than 40, but even zones

with ratios as low as 2 are observed (Figure 5-3d). For these smaller X/Y values, the polarization dependency increasingly diverges from the $\cos^4\alpha$ pattern (Figure 5-4b). As is demonstrated in Appendix E, this corresponds to less well aligned PNA. IR and Raman studies of PNA in AlPO-5 have shown that the non-hydrogen bonded PNA has a larger tilt angle as compared to the hydrogen bonded arrangement.[6b,7] Clearly, this corresponds to more loosely interacting PNA, without hydrogen bonds. In their original SHG study, Cox et al.4a proposed that a loose arrangement of PNA in AlPO-5 pores would not give rise to SHG light. However, based on the spatially resolved SHGM images, it can be asserted now that even a more dilute PNA arrangement gives rise to considerable SHG, as is shown by the spatial overlay of the SHG and X/Y orientational maps in Figure 5-3d.

The co-existence of crystals with dense or dilute PNA arrangement within one batch proves that there is a considerable intercrystalline heterogeneity, resulting in domains with distinct SHG characteristics throughout the powder sample. Such a heterogeneity has also been observed using Raman spectroscopy, but in these experiments, the spatial resolution was limited by the spot size of 30 µm, which is far too coarse to observe any intracrystalline differences.[6b] On the other hand, the spatial resolution of the SHGM now gives direct evidence for intracrystalline domain formation, as shown in Figures 3c and 3d. Domains with different X/Y ratios are scattered throughout the crystal. Recall that the PNA is introduced in the crystals at 150°C. FTIR studies have proven that at high temperature, the PNA assumes a melt-like state. The domains that are observed in the SHGM orientational mapping reflect the organization that the PNA assumes upon cooling. A theoretical study has proven that a dense and dilute PNA phase can coexist in one linear AlPO-5 channel if besides the nearest-neighbour interactions, the overall electrostatic field arising from all PNA molecules in the same channel is taken into account.[16] However, it is unclear whether domain formation would extend beyond one dimension, and whether interactions between PNA chains in adjacent pores would induce a spatial matching along the *c*-axis of the dense zones in adjacent pores. This would mean that the domains also extend perpendicularly to the *c*-axis. Zooming in on a portion of the crystal in Figure 5-3c shows that a domain of 0.5 x 0.5 µm with *X/Y* ~ 350 is directly flanked by a 1 x 3 µm domain with *X/Y* ~ 180 (Figure

5-3c, inset). This directly proves that the domain formation extends in three dimensions. In the same zone of crystal, both the 2-photon fluorescence and the SHG image suggest a fairly homogeneous loading with PNA, which seems to exclude that defects and poor pore filling are at the origin of the variations in the *X/Y* mapping. Previously, only indirect indications for three-dimensional domain formation have been obtained, *e.g.* in a dielectric spectroscopy study of the cooperative dynamics of PNA in AlPO-5.[17] The size of the domains that can be distinguished by SHGM varies between a few hundred nanometres, which is close to the diffraction limit (as in Figure 5-3c), to > 10 µm (as in Figure 5-3d), suggesting that the nucleation rates for the formation of the dense domains vary.

The detailed structural insights that are gained via SHGM could not have been obtained via other techniques, such as X-ray diffraction, especially since the organisation of PNA is not commensurate with the surrounding AFI structure. Indeed, the length of a PNA molecule, 9 Å, is not compatible with the unit cell parameter of AFI along the channel axis, 8.4 Å, and the width of the pores allows for a variety of orientations of PNA inside the pores. Cox et al.[4a] attempted to localize PNA in AlPO-5, but did not succeed in obtaining a convergent solution by Rietveld refinement. For a host/guest system in which the guest molecules do have a periodic ordering, but with a periodicity different from the host-structure, it is extremely hard to determine the ordering of the guest molecules with XRD. SHGM, in contrast with XRD, is not limited by these conditions, and more importantly, can probe molecular organization with a spatial resolution that X-ray diffraction lacks.

5.3 Conclusions

PNA-loaded SAPO-5 crystals were investigated with two-photon fluorescence and SHG microscopy. SHGM on adsorbate-loaded materials is highly useful to reveal details of the crystallite structure: intergrown crystallites containing hexagonal pyramidal components and internal diffusion barriers are found next to seemingly perfect crystals in which the pores run from one crystal end to the other. The orientation of the adsorbed PNA molecules could be mapped with a spatial resolution that was only limited by the diffraction of light. Dense domains with highly aligned PNA alternate with more dilute domains of loosely interacting PNA. It could be shown that these dense or dilute domains extend in all crystallographic directions, with domain sizes ranging from around 1 up to more than 10 µm. As SHGM can successfully follow the organization of host molecules in host/guest systems with spatial resolution, it is complementary with the traditionally used XRD technique.

Note: Appendix G provides the experimental procedures concerning the experiments presented in this chapter.

References

1 M. Ehrl, F.W. Deeg, C. Bräuchle, O. Franke, A. Sobbi, G. Schulz-Ekloff, D. Wörhle, *J. Phys. Chem.* **1994**, *98*, 47.

2 a) S.D. Cox, T.E. Gier, G.D. Stucky, J. Bierlein, *J. Am. Chem. Soc.* **1988**, *110*, 2986; b) F. Marlow, J. Caro, L. Werner, J. Kornatowski, S. Dähne, *J. Phys. Chem.* **1993**, *97*, 11286.

3 U. Kynast, V. Weiler, *Adv. Mater.* **1994**, *6*, 937.

4 a) S.D. Cox, T.E. Gier, G.D. Stucky, *Chem. Mater.* **1990**, *2*, 609; b) J. Caro, G. Finger, J. Kornatowski, J. Richter-Mendau, L. Werner, B. Zibrowious, *Adv. Mater.* **1992**, *4*, 273; c) L. Werner, J. Caro, G. Finger, J. Kornatowski, *Zeolites* **1992**, *12*, 658.

5 a) F. Marlow, M. Wübbenhorst, J. Caro, *J. Phys. Chem.* **1994**, *98*, 12315; b) G.J. Klap, S.M. van Klooster, M. Wübbenhorst, J.C. Jansen, H. van Bekkum, J. van Turnhout, *J. Phys. Chem. B* **1998**, *102*, 9518; c) G.J. Klap, M. Wübbenhorst, J.C. Jansen, H. van Koningsveld, H. van Bekkum, J. van Turnhout, *Chem. Mater.* **1999**, *11*, 3497.

6 a) F. Marlow, W. Hill, J. Caro, G. Finger, *J. Raman. Spectrosc*. **1993**, *24*, 603; b) W. Hill, F. Marlow, J. Kornatowski, *Appl. Spectr.* **1994**, *48*, 224.

7 F. Marlow, D. Demuth, G. Stucky, F. Schüth, *J. Phys. Chem.* **1995**, *99*, 1306.

8 K. Hoffmann, F. Marlow, J. Caro, *Zeolites* **1996**, *16*, 281.

9 I. Kinski, P. Daniels, C. Deroche, B. Marler, H. Gies *Microporous Mesoporous Mater.* **2002**, *56*, 11.

10 E. Lehmann, C. Chmelik, H. Scheidt, S. Vasenkov, B. Staudte, J. Kärger, F. Kremer, G. Zadrozna, J. Kornatowski, *J. Am. Chem. Soc.* **2002**, *124*, 8690.

11 L. Karwacki, E. Stavitski, M.H.F. Kox, J. Kornatowski, B. Weckhuysen, *Angew. Chem.* **2007**, *119*, 7366.

12 E. Lehmann, S. Vasenkov, J. Kärger, G. Zadrozna, J. Kornatowski, Ö Weiss, F. Schüdt, *J. Phys. Chem.* B **2003**, *107*, 4685.

13 I. Girnus, K. Jancke, R. Vetter, J. Richter-Mendau, J. Caro, *Zeolites* **1995**, *15*, 33.

14 C. Martin, N. Tosi-Pellenq, J. Patarin, J.P. Coulomb, *Langmuir* **1998**, *14*, 1774.

15 S.J. Lalama, A.F. Garito, *Phys. Rev. A* **1979**, *20*, 1179.

16 I. Leike, F. Marlow, *Zeolites*, **1996**, *16*, 65.

17 M. Wübbenhorst, G.J. Klap, J.C. Jansen, H. van Bekkum, J. van Turnhout, *Chem. Phys.* **1999**, *111*, 5637.

General conclusions

We have probed adsorption onto a zeolite, *viz.* a *b*-oriented silicalite-1 film, for the first time with second-harmonic generation *in situ*. This methodology allowed for the observation of this process in the liquid phase and for a deeper insight into the complexity of the adsorption process. By continuously monitoring the change in orientation of the aromatic adsorbate molecules, it was established that the adsorbate molecules, DAMPI, positioned themselves gradually more into the pore direction over the course of two hours. A physisorbed state on the outer surface prior to pore-mouth adsorption is suggested by the data. In literature, such a preceding physisorbed state had been observed for adsorption of aromatic molecules on a zeolite in the gas phase. However, SHG has allowed for such an observation for the first time in the liquid phase.

The suitability of SHG to probe buried interfaces has also been exploited to show that diffusion of a solute through a thin film under a liquid phase can be probed by SHG *in situ*. In particular, diffusion through a silicalite-1 precursor film deposited on a solid substrate was studied. It was in fact the arrival of the solute molecules at the solid/film interface that was monitored. This is an important finding since only few techniques are capable to study diffusion through buried films and each of these techniques has its limitations.

Apart from these bulk-measurements, a second-harmonic generation microscope was built. This set-up additionally allowed two-photon fluorescence imaging. In this work, SHGM was for the first time used to study zeolites. More specifically, we explored molecular organization inside zeolites.

First this was done for *p*-nitroaniline adsorbed in ZSM-5 crystals. It was possible to relate the different molecular organization of *para*-nitroaniline in the two pore types of ZSM-5 to their SHG response, making SHGM a powerful tool for revealing structural details and the intergrown structure of ZSM-5 crystals. No doubt, this methodology can be extrapolated to other zeolites. The SHG-response of adsorbates in zeolites is due to a surface selection process which causes the PNA molecules to adsorb predominantly with one functional group first, giving rise to SHG-active dipole chains inside the pores.

The microscopy set-up made it possible to see the effect of the bidimensionality of the pore system on the dipolar organization. Indeed, only close to the surface gave the adsorbed PNA rise to SHG; hence, diffusion from one pore type to the other disrupts the dipolar organization.

The SHG/TPF microscope was also used to image the PNA-filled one-dimensional pore system of SAPO-5 zeolite crystals. The SHG and 2-photon fluorescence response of PNA in the one-dimensional channels readily reveals the pore accessibility; intergrown crystallites containing hexagonal pyramidal components and internal diffusion barriers are found next to seemingly perfect crystals in which the pores run from one crystal end to the other. The sensitivity of second-harmonic generation to molecular orientation combined with the spatial resolution of microscopy allowed for mapping of the domains of differently organized PNA. Dense phases of highly aligned PNA alternate with phases of more loosely interacting PNA. It could be shown that these dense or dilute domains extend in all crystallographic directions, with domains ranging from around 1 µm to more than 10 µm.

Summarizing, we showed that SHGM can successfully map the organization of host molecules in host/guest systems with spatial resolution and is therefore complementary with the traditionally used XRD technique. X-ray diffraction has the unique capacity to determine the position and orientation of a molecule exactly, but the use of XRD is limited to systems in which the molecules of interest have a crystallographic position. Moreover, if the guest molecules have a periodic ordering, but another periodicity than the host-structure, it is extremely hard to determine the ordering of the guest molecules. SHGM, though less specific, is not limited by these conditions, and, more importantly, can probe molecular organization with a spatial resolution that X-ray diffraction lacks.

Due to the successful use of SHG to study adsorption and diffusion in the liquid phase, and the implementation of SHG into a microscope, the next step is to combine both and design liquid phase diffusion experiments in zeolite crystals so that time-dependent concentration profiles can be taken. It has been shown, most notably via interference microscopy, that such profiles reveal much more information concerning the adsorption

and diffusion process than traditional uptake measurements. By using SHGM the gap to the liquid phase is elegantly overcome.

The use of second-harmonic generation on zeolites can be extended from the study of adsorption, diffusion and organization of adsorbate molecules to the study of conversion of adsorbate molecules, thus heterogeneous catalysis. The condition is that the probed reagents or products have a dipolar organization, which can be ensured by using asymmetric reagent molecules that adsorb selectively with one functional group into the pore-mouth. By choosing reactions with either a reagent or a product molecule with a sufficiently high hyperpolarizability, either the disappearance of reagent molecules or the product formation can be probed. Obvious advantages of this strategy are the possibility of studying reactions in the liquid phase *in situ*. Not only will SHGM provide spatial resolution, which will point out diffusion limitations and which crystal parts take part in the conversion process, the sensitivity of SHGM to molecular organization will provide further insight into the conversion process. For example, it may be possible to assign the active positions to a certain pore type (*vide* PNA in ZSM-5) or to reveal the organization/orientation of reagent molecules or product molecules during the reaction.

Appendix A: Crystal batches and number of crystals studied in the PNA-loaded ZSM-5 study

Batch A contained ZSM-5 crystals of 15 x 10 x 80 μm^3, with Si/Al = 700. In a previous publication, this batch was characterized in full detail (Roeffaers et al. JACS 2008, 130, 5763, 'batch B').

Eight different crystals were picked from this batch A for detailed SHGM analysis (half of them lay on their (010) face and half of them on their (100) face). They all yielded similar results, and representative data are shown for crystals A1 and A2 (Figure 1a-b and 1d-e in the main text).

Batch B contained ZSM-5 crystals of 15 x 10 x 80 μm^3, with Si/Al = 40. In a previous publication, this batch was characterized in full detail (Roeffaers et al. JACS 2008, 130, 5763, 'batch C').

Eight different crystals were picked from this batch B for detailed SHGM analysis (three of them lay on their (010) face and five of them on their (100) face). The crystals lying on their (010) face yielded similar results as the crystals of batch A lying on their (010) face. Of the five crystals lying on their (100) face, three of them yielded similar results, and representative data are shown in figure 1c and 1f in the main text. For the two other crystals we encountered a slightly different SHG pattern. Two polarization patterns were recognized in the SHG-active zone close to the hexagonal facet (Figure A 1). In the middle of the two strips that generate SHG, a four-lobe polarization pattern was detected, but towards the crystal extremities (Figure A 1, inside the circles), a two-lobe pattern was detected. This demonstrates that the original axis orientation is preserved there, but that more centrally on the hexagonal facet, there is a 90° rotated section with a (100)' face as outer surface.

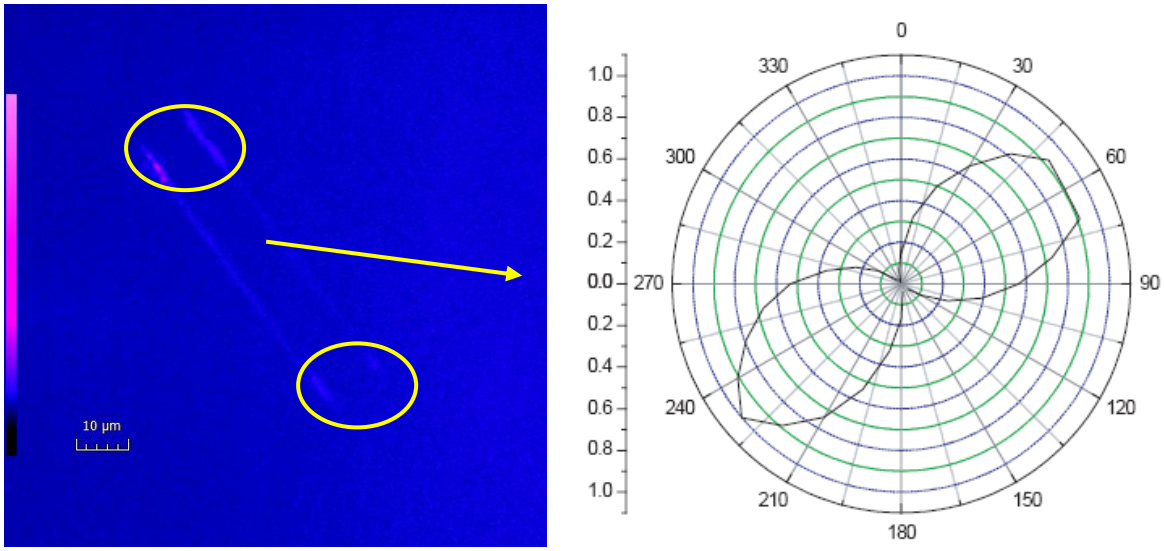

Figure A 1: SHG micrograph (left) of a crystal of batch B lying on its (100) face, and the polarization pattern (right) observed from the SHG-active areas towards the extremities of the crystal.

Appendix B: Polarization patterns for PNA-loaded ZSM-5

To analyse the different polarization patterns, we used the following quantitative model. The distribution of PNA in the crystal will be C_{1v} symmetric (mirror plane is in the XZ plane) at each position in the sample, independent of the type of pores. In that case, and for perpendicular illumination (in the YX plane), there are only 3 susceptibility components that can be addressed, *i.e.* $\chi^{(2)}_{XXX}$, $\chi^{(2)}_{XYY}$, $\chi^{(2)}_{YXY} = \chi^{(2)}_{YYX}$. All these components can be written as a function of the molecular hyperpolarizability by using a simple coordinate transformation between the macroscopic coordinate system XYZ and the molecular frame of reference *xyz* (Figure B 1). Furthermore, if we assume that PNA has only 1 dominant hyperpolarizability component β_{xxx}, the susceptibilities greatly simplify. This assumption is reasonable since it has been shown that other susceptibility components in PNA are typically a factor of 5 to 10 smaller than the *xxx* component, even under resonant conditions (see for example S.J. Lalama, A.F. Garito, Phys. Rev. A, 20(3), 1179-1194, 1979). Hence, the susceptibilities are

$$\chi^{(2)}_{XXX} = Nf\beta_{xxx}\left\langle cos^3\theta \right\rangle$$
$$\chi^{(2)}_{XYY} = \chi^{(2)}_{YXY} = \chi^{(2)}_{YYX} = Nf\beta_{xxx}\left\langle cos\theta\, sin^2\theta \right\rangle$$

With N the number density of molecules and f a local field factor. Notice also that the number of independent susceptibility components reduces to 2. In addition, if *PNA* is oriented in straight dipole chains (θ close to 0°), only 1 susceptibility component remains. On the other hand, if PNA is oriented in a zigzag fashion ($\theta \neq 0°$), both susceptibility components will be different from zero.

If we now include the polarization dependence of the SHG-light, we obtain :

$$I(2\omega) \propto \left|\chi^{(2)}_{XXX}E^2 sin^2\varphi + \chi^{(2)}_{XYY}E^2 cos^2\varphi\right|^2 + \left|\chi^{(2)}_{YXY}E^2 sin\varphi cos\varphi + \chi^{(2)}_{YYX}E^2 sin\varphi cos\varphi\right|^2$$

with φ the rotation angle of the electric field E of the fundamental. From this equation it is clear that we can distinguish two distinct situations: if PNA is oriented in straight dipole chains, the functional form of the polarisation pattern is :

$$I(2\omega) \propto a\cos^4\varphi$$

and if PNA is oriented in a zigzag pattern, the functional dependence will be :

$$I(2\omega) \propto a\cos^4\varphi + b\sin^4\varphi + c\sin^2\varphi\cos^2\varphi$$

with a, b and c functions of the different susceptibility components. The difference between both situations is illustrated in Figure B 2, where a straight dipole orientation leads to a 2-lobe pattern, while a zigzag configuration leads to a 4-lobe pattern.

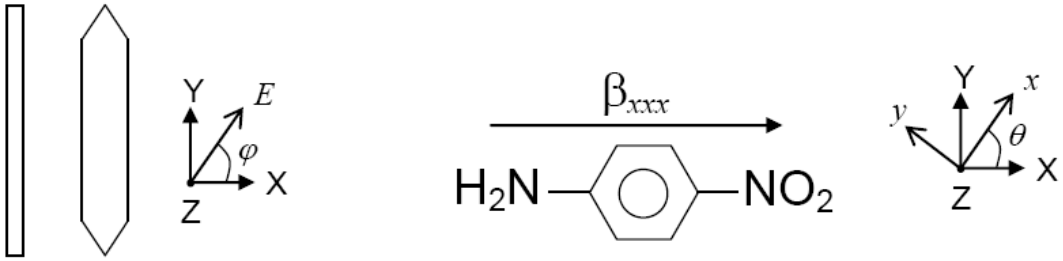

Figure B 1: Left: macroscopic coordinate system XYZ with polarisation vector E. Middle: molecular structure of PNA with one dominant hyperpolarizability component. Right: macroscopic coordinate system XYZ and molecular frame of reference xyz

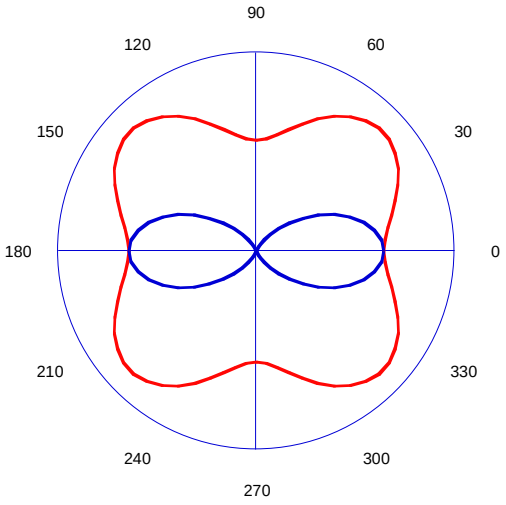

Figure B 2: Polarization dependence of the second-harmonic light for PNA oriented in straight dipole chains (blue line) and PNA oriented in a zigzag pattern (red line).

Appendix C: Note regarding the observation of PNA dipole chains in variously positioned ZSM-5 crystals, with or without 90° rotated section

In the following, 4 sections across the *ab* plane of the zeolite crystal are shown. For each case, the possibility to observe PNA dipole chains is discussed.

Case 1: 'Perfect' crystal, lying on its (010) face:

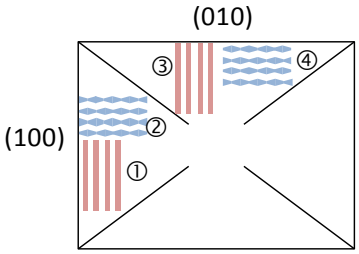

① Straight pores parallel with (100): no PNA can be detected in SHG because the chains are parallel to the propagation vector of incident light;

② Sinusoidal pores, perpendicular on (100): SHG is effectively detected;

③ Straight pores, perpendicular on (010): no SHG detected because the chains are parallel to the propagation vector of the incident light;

④ Sinusoidal pores, parallel with (010): if PNA chains were present, they should be detected by SHG. However, we detect no signal; it seems the PNA is not present as dipole chains in these pores, simply because these pores cannot be filled directly from the outer surface.

Case 2: 'Perfect' crystal, lying on its (100) face:

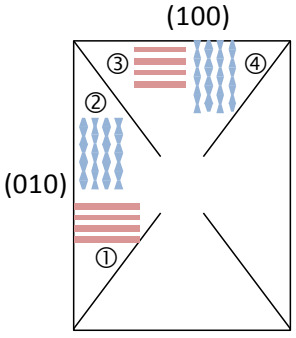

① Straight pores perpendicular on (010): SHG of linear PNA chains is effectively detected;

② Sinusoidal pores, parallel with (010): no PNA can be detected in SHG because the chains are parallel to the propagation vector of the incident light;

③ Straight pores, parallel with (100): if PNA chains were present in these pores, they should be detected. However, SHG does not detect a signal, so it seems there are no PNA chains;

④ Sinusoidal pores, perpendicular on (100): no PNA can be detected in SHG because the chains are parallel to the propagation vector of the incident light.

Case 3: crystal with 90° intergrowth, lying on its (010) face, which is the (100)' face of the intergrown component:

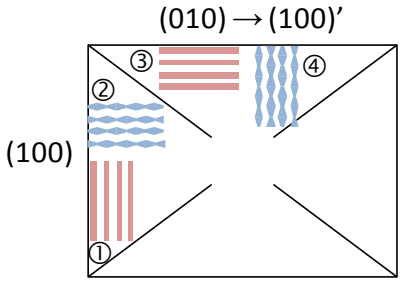

① Straight pores parallel with (100): no PNA can be detected in SHG because the chains are parallel to the propagation vector of the incident light;

② Sinusoidal pores, perpendicular on (100): SHG is effectively detected;

③ Straight pores, parallel with (100)': if PNA chains were present in these pores, they should be detected. However, SHG does not detect a signal;

④ Sinusoidal pores, perpendicular on (100)': no PNA can be detected in SHG because the chains are parallel to the propagation vector of the incident light.

Case 4: crystal with 90° intergrowth, lying on its (100) face:

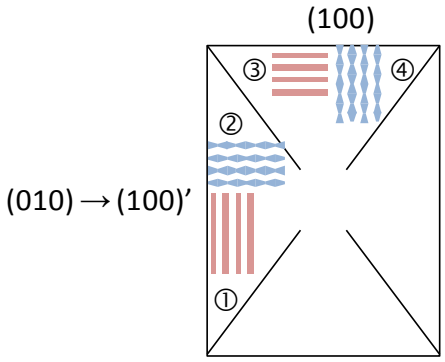

① Straight pores parallel with (100)': no PNA can be detected in SHG because the chains are parallel to the propagation vector of the incident light;

② Sinusoidal pores, perpendicular on (100)': SHG is effectively detected;

③ Straight pores, parallel with (100): if PNA chains were present in these pores, they should be detected. No SHG signal detected;

④ Sinusoidal pores, perpendicular on (100): no PNA can be detected in SHG because the chains are parallel to the propagation vector of the incident light.

Appendix D: X-ray diffractogram of SAPO-5 after calcination

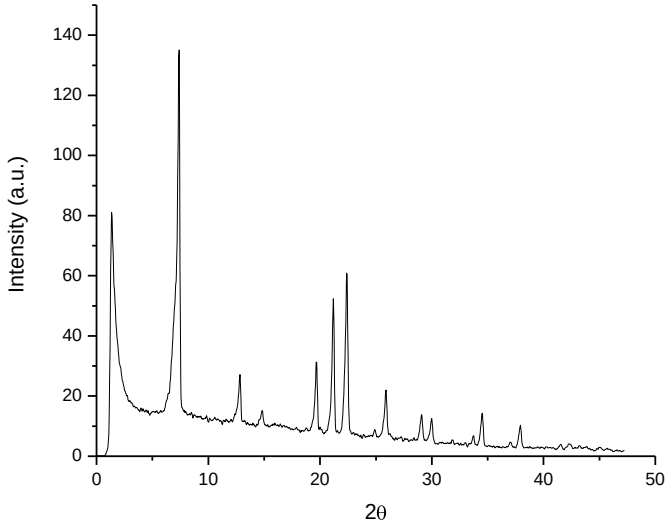

Appendix E: Theory concerning the X/Y ratio for the SHGM-measurements of PNA-loaded SAPO-5

SHG, a second-order nonlinear optical effect, can be described by its nonlinear polarization $P(2\omega)$, given by

$$P(2\omega) = \chi^{(2)} E(\omega) E(\omega)$$

With E the electric field of the fundamental light at frequency ω and $\chi^{(2)}$ the second-order susceptibility that quantifies the nonlinear optical response. $\chi^{(2)}$ is a third-rank tensor with 27 components. The number of nonvanishing susceptibility components however, depends upon the symmetry of the medium under investigation. Furthermore, also the particular experimental configuration will limit the number of components that can be addressed. For an experimental situation where the fundamental light is incident under normal incidence and if we assume that the crystal is in the *xy*-plane (Figure E 1), we can write the nonlinear polarization in the most general case as :

$$\begin{aligned} P &= \chi^{(2)}_{xxx} E_x E_x + \chi^{(2)}_{xyy} xyy E_y E_y + 2\chi^{(2)}_{xyx} E_y E_x + \chi^{(2)}_{yxx} E_x E_x + \chi^{(2)}_{yyy} E_y E_y + 2\chi^{(2)}_{yyx} E_y E_x \\ &= \chi^{(2)}_{xxx} E_0^2 \cos^2\alpha + \chi^{(2)}_{xyy} E_0^2 \sin^2\alpha + 2\chi^{(2)}_{xyx} E_0^2 \cos\alpha \sin\alpha \\ &+ \chi^{(2)}_{yxx} E_0^2 \cos^2\alpha + \chi^{(2)}_{yyy} E_0^2 \sin^2\alpha + 2\chi^{(2)}_{yyx} E_0^2 \cos\alpha \sin\alpha \end{aligned}$$

With the angle α the polarization angle (Figure E 1). Note that in the used experimental configuration, there is no *z*-component of the polarization because the polarization does not radiate in the direction of propagation. Also, the electric field of the incident light too obviously has no *z*-component. This equation can be further simplified if we make additional assumptions concerning the symmetry of the crystal. If we choose the laboratory coordinate system such that the *x*-axis coincides with the long crystal axis *c*, a mirror plane in the *xz*-plane is expected for the PNA-loaded SAPO-5 crystal. This is in agreement with earlier SHG-studies of PNA-loaded AlPO-5 crystals. Moreover, the measured data in these study are in agreement with such a mirror plane. In the case of such a mirror plane, all susceptibility components with an uneven number of *y*-indices will vanish, and the polarization simplifies to

$$P = \chi^{(2)}_{xxx} E_0^2 \cos^2\alpha + \chi^{(2)}_{xyy} E_0^2 \sin^2\alpha + 2\chi^{(2)}_{yyx} E_0^2 \cos\alpha \sin\alpha$$

The second-harmonic intensity is proportional to the square of the polarization. Hence the second-harmonic intensity is given by

$$\begin{aligned} I(2\omega) &\propto \left| \chi^{(2)}_{xxx} E_0^2 \cos^2\alpha + \chi^{(2)}_{xyy} E_0^2 \sin^2\alpha + 2\chi^{(2)}_{yyx} E_0^2 \cos\alpha \sin\alpha \right|^2 \\ &= \left| \chi^{(2)}_{xxx} \cos^2\alpha + \chi^{(2)}_{xyy} \sin^2\alpha + 2\chi^{(2)}_{yyx} \cos\alpha \sin\alpha \right|^2 I(\omega)^2 \end{aligned}$$

If we now define the ratio X/Y as the ratio of intensities for measurements with an input polarization of α = 0° and 90°, we obtain :

$$\frac{X}{Y} = \frac{\left|\chi^{(2)}_{xxx}\right|^2}{\left|\chi^{(2)}_{xyy}\right|^2}$$

This ratio is sensitive to changes in orientation of PNA, since both susceptibility components are function of the tilt angle and the hyperpolarizability β of PNA. If we assume that PNA has only one hyperpolarizability component $\beta_{z'z'z'}$ along the long molecular axis z', the xyy component will vanish if PNA is oriented along the x-direction, and the ratio X/Y goes to infinity. The second-harmonic intensity can then be described by

$$I(2\omega) \propto \left| \chi^{(2)}_{xxx} \right|^2 \cos\alpha \,^4 I(\omega)^2$$

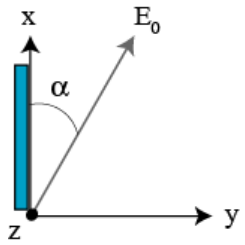

Figure E 1: The orientation of the coordinate system used in our calculations. The rectangle represents the SAPO-5 crystal, E_0 is the fundamental electric field amplitude and α the polarization angle.

Under the reasonable assumption that PNA has only one hyperpolarizability component, the relation between the nonlinear susceptibility and the hyperpolarizability is given by

$$\chi^{(2)}_{XXX} = Nf\,\beta_{xxx}\left\langle \cos^3\theta \right\rangle$$
$$\chi^{(2)}_{XYY} = \chi^{(2)}_{YXY} = \chi^{(2)}_{YYX} = Nf\,\beta_{xxx}\left\langle \cos\theta \sin^2\theta \right\rangle$$

With θ the tilt angle, defined as the angle between the long molecular axis of PNA and the long crystal axis *c*. It is indeed clear that the ratio of these two equations is a measure for the average tilt angle θ, hence so is *X/Y*.

Appendix F: Discussion of the IR-spectrum of PNA-filled SAPO-5

In the IR-spectrum shown in Figure 5-2 in Chapter 5, the principal IR-absorptions are located in the region between 3000 and 3500 cm^{-1} and the region between 1000 and 1800 cm^{-1}. The region from 3000 and 3500 cm^{-1} is the NH-stretching region. This region is the most affected by hydrogen bonds. Four absorption peaks can be distinguished in this region. As mentioned in chapter 5, the band at 3483 cm^{-1} is assigned to the asymmetric NH-stretching vibration, while the band at 3359 cm^{-1} represents the symmetric NH-stretching vibration. The weaker bands at 3215 and 3235 cm^{-1} can be assigned to H-bonded species.

Looking at the positions of these bands in Table F 1 for PNA in different forms, we see that the positions for PNA-loaded SAPO-5 compare very well to crystalline PNA. In this form, the PNA molecules are mutually hydrogen bonded. In contrast, for PNA that is not hydrogen bonded, like PNA dissolved in $CHCl_3$, and for PNA that has significantly weaker hydrogen bonds, like PNA in silica-ZSM-12, the frequencies for the symmetric and asymmetric stretching vibrations are significantly higher. A shift to higher frequency with decreasing strength of the hydrogen bond is indeed expected for these vibrations (Novak A., Structure and Bonding 1974, 18, 177). Due to the high correspondence of the vibrations in the N-H stretch region of PNA-loaded SAPO-5 with the hydrogen bonded crystalline PNA, we conclude that at least a certain amount of hydrogen-bonded PNA must be present.

For PNA in AlPO-5, it has been found that PNA can be present both in a hydrogen-bonded state and in a state that corresponds more to PNA in solution. By Marlow et al. (J. Phys. Chem. 1995, 99, 1306) a sample in which PNA was dominantly present as hydrogen bonded PNA was heated to break the H-bonds and see the effect of this on the IR-spectrum. The bonds at 3235 and 3215 cm^{-1} related to hydrogen-bonded species lost most of their intensity. The symmetric NH-stretch vibration became significantly sharper. Although the positions of the asymmetric and symmetric NH-stretch vibration hardly changed, their respective intensity changed. Before breaking the H-bonds, the

band at 3483 cm^{-1} is at least as intense as the band at 3359 cm^{-1}. By breaking the hydrogen bonds, the band at 3359 cm^{-1} gains more intensity, in fact more than double of the intensity of the asymmetric stretching band at 3483 cm^{-1}. Also for the hydrogen bonded crystalline PNA, the peaks of the asymmetric stretch vibration are of equal intensity of the symmetric N-H stretch vibration (Microporous Mesoporous Mater. 2002, 56, 11), while for PNA dissolved in $CHCl_3$ the symmetric stretch vibration has 5 times the intensity of the asymmetric stretch vibration (J. Phys. Chem. 1995, 99, 1306). Since in our spectrum the peak of the symmetric stretch vibration at 3359 cm^{-1} is clearly more intense than the asymmetric stretch vibration at 3483 cm^{-1}, it is likely that a part of the incorporated PNA is present in a solution-like state. So PNA seems to be present in two different arrangements, one with and one without mutual H-bridges.

Table F 1: Comparison of N-H stretch vibrations (cm^{-1}) of PNA in different forms: incorporated in SAPO-5, AlPO-5 or silica-ZSM-12, as a pure crystal or as individual molecules dissolved in chloroform.

no.	PNA in SAPO-5	PNA in AlPO-5*	PNA in ZSM-12†	PNA cryst†	PNA in $CHCl_3$*
1	3483	3500	3511	3481	3510
2	3359	3393	3404	3363	3410
3			3386	(3307)	
4	3235	3235	3255	3239	3280
5	3215	3215	3230	3216	

* data from Marlow et al. J. Phys. Chem. 1995, 99, 1306

† data from Kinski et al. Microporous Mesoporous Mater. 2002, 56, 11.

The region in Figure 5-2 from 1000 to 1800 cm^{-1} is dominated by vibrations of the carbon skeleton, which might be modified by interactions with the host lattice and are partly superimposed by vibrations of the host lattice. The positions of the peaks in this spectrum correspond with the IR-spectrum of PNA incorporated in AlPO-5 measured by Marlow et al. (J. Phys. Chem. 1995, 99, 1306; measured from 1200 cm^{-1} to 3800 cm^{-1}).

A comparison between the PNA and *p*-nitroanilinium complexes shows that many bands change their position and several new bands appear. For *p*-nitroanilinium complexes a strong band at 1605 cm^{-1} is present which can be assigned to the symmetrical deformation of the NH_3^+ group (Mater. Sci. Eng. B 2003, 100, 225; J. Nonlinear Opt. Phys. Mater. 2003, 12, 113). In the spectrum shown in Figure 5-2, this peak cannot be distinguished between the scissoring NH_2 vibration at 1630 cm^{-1} and the CC stretch vibration at 1595 cm^{-1} (J. Phys. Chem. B, 1997, 101, 483). Moreover, a broad and intense band located between 3200 cm^{-1} and 3000 cm^{-1} or lower is observed (Mater. Sci. Eng. B 2003, 100, 225; J. Nonlinear Opt. Phys. Mater. 2003, 12, 113) for a NH_3^+ group involved in hydrogen bonds. This band too is not observed for PNA-loaded SAPO-5 (Figure 5-2). Thus, as expected, protonation of the incorporated PNA by the host SAPO-5 framework is negligible or non-existent.

Appendix G: Experimental procedures concerning PNA-loaded SAPO-5

SAPO-5 was prepared under continuous stirring from H_3PO_4 (85 wt %), tripropylamine (≥98%), aluminium isopropoxide (≥98%) and bi-distilled water via a modification of the procedure described by Fan et al. (Phys. Chem. Chem. Phys., 2001, 3, 3240). First, Al-isopropoxide was hydrolyzed in water under continuous stirring at 40°C. Dilute H_3PO_4 was added to the slurry. Subsequently, the mixture was aged for 15 min under gentle stirring. Then, the template tripropylamine (TPA) was introduced dropwise after which the gel was aged for another 30 min. A single portion of Ludox-AS40 was further added to the synthesis gel. The molar composition of the final gel was 1 Al_2O_3 : 0.99 P_2O_5 : 0.6 Pr_3N : 400 H_2O : 0.01 SiO_2. After stirring for another 30 min, the gel was loaded into a Teflon lined stainless steel autoclave. The hydrothermal treatment was carried out dynamically at 190°C for 15h. After crystallization, all autoclaves were quenched under cold water flow, the crystals were centrifuged, washed thoroughly with bi-distilled water and dried at 60°C for 24h.

The SAPO crystals were calcined under an O_2 flow. After slowly heating the crystals (at 1°C/minute), the sample was left at 600°C for 15h. Thereafter the crystals were characterized by Scanning Electron Microscopy (SEM, Philips XL 30 FEG) and a powder X-ray diffractogram was measured on a STOE StadiP operating in high-throughput mode using CuKα radiation with a wavelength of 1.541 Å. The PNA molecules were introduced into the SAPO-5 crystals via a gas-phase loading process by contacting the evacuated SAPO-5 crystals with saturated PNA vapour at 150°C for 24h. The amount of adsorbed PNA was determined by thermogravimetric analysis (TA instruments, TGA Q500) under O_2-atmosphere and with a heating rate of 10°C/minute until 1000°C. The infrared spectrum of dry, PNA-loaded SAPO-5 crystals in KBr pellets was recorded on a Fourier Transform Infrared spectrometer (Bruker, IFS 66v/S).

The microscopy images were taken with an inverted wide-field microscope (Olympus, IX-71) coupled to a femtosecond Ti-sapphire laser. Images were recorded in transmission geometry with an EM-CCD camera (Hamamatsu, C9100-13). By using

appropriate filters, the set-up can be used to record both two-photon fluorescence images and SHG images. With a polarizer and a half-wave plate in the incident laser beam, we were able to record polarization patterns for each position on the image.

Publications

Publications related to this work:

M.A. van der Veen, V.K. Valev, T. Verbiest, D.E. De Vos
In Situ Orientation-Sensitive Observation of Molecular Adsorption on a Liquid/Zeolite Interface by Second-Harmonic Generation
Langmuir **2009**, *25*(8), 4256-4261

M.A. van der Veen, M. De Roeck, I.F.J. Vankelecom, D.E. De Vos, T. Verbiest
The Use of Second-Harmonic Generation to Study Diffusion through Films under a Liquid Phase
ChemPhysChem **2010**, *11*(4), 870-874

M.A. van der Veen, B.F. Sels., D.E. De Vos, T. Verbiest
Localization of para-nitroaniline chains inside zeolite ZSM-5 with second-harmonic generation microscopy
Journal of the American Chemical Society **2010**, *132*(19), 6630–6631

M.A. van der Veen, J. Van Noyen, B.F. Sels, P.A. Jacobs, T. Verbiest, D.E. De Vos
Mapping of the organization of p-nitroaniline in SAPO-5 by second-harmonic generation microscopy
Physical Chemistry Chemical Physics (submitted)

Publications not related to this work:

L. Alaerts, C.E.A. Kirschhock, M. Maes, M.A. van der Veen, V. Finsy, A. Depla, J.A. Martens, G.V. Baron, P.A. Jacobs, J.F.M. Denayer, D.E. De Vos
Selective Adsorption and Separation of Xylene Isomers and Ethylbenzene with the Microporous Vanadium(IV) Terephthalate MIL-47
Angewandte Chemie (International ed.) **2007**, *46*(23), 4293-4297

L. Alaerts, M. Maes, M.A. van der Veen, P.A. Jacobs, D.E. De Vos

Metal-organic frameworks as high-potential adsorbents for liquid-phase separations of olefins, alkylnaphthalenes and dichlorobenzenes.

Physical Chemistry Chemical Physics **2009**, *11*(16), 2903-2911